WL-TR-94-2054

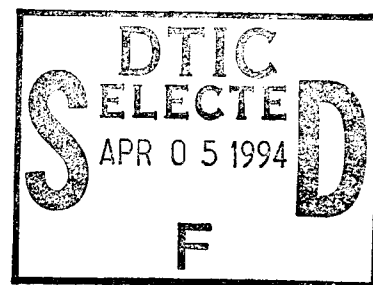# FEASIBILITY STUDY OF USING NEUTRON DIAGNOSTICS FOR TURBINE ENGINE STRUCTURAL MEASUREMENTS

PREPARED BY: D. LEGGETT

PRATT & WHITNEY CANADA INC.
1000 MARIE VICTORIN
LONQUEUIL QUEBEC J4G 1A1

FEBRUARY 1994

FINAL REPORT FOR 09/01/88 - 02/01/94

DTIC
ELECTED
SELECTED
APR 0 5 1994
F

19950403 166

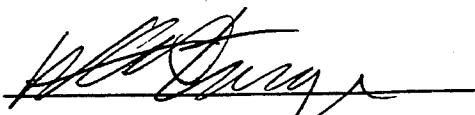## NOTICE

When Government drawings, specifications, or other data are used for any purpose other than in connection with a definitely Government-related procurement, the United States Government incurs no responsibility or any obligation whatsoever. The fact that the government may have formulated or in any way supplied the said drawings, specifications, or other data, is not to be regarded by implication, or otherwise in any manner construed, as licensing the holder, or any other person or corporation; or as conveying any rights or permission to manufacture, use, or sell any patented invention that may in any way be related thereto.

This report is releasable to the National Technical Information Service (NTIS). At NTIS, it will be available to the general public, including foreign nations.
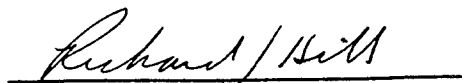
This technical report has been reviewed and is approved for publication.

WILLIAM A. STANGE
PROJECT ENGINEER
COMPONENTS BRANCH
TURBINE ENGINE DIVISION
AERO PROPULSION & POWER DIRECTORATE

THEODORE G. FECKE
CHIEF, COMPONENTS BRANCH
TURBINE ENGINE DIVISION
AERO PROPULSION & POWER DIRECTORATE

RICHARD J. HILL
CHIEF OF TECHNOLOGY
TURBINE ENGINE DIVISION
AERO PROPULSION & POWER DIRECTORATE

If your address has changed, if you wish to be removed from our mailing list, or if the addressee is no longer employed by your organization please notify WL/POTC , WPAFB, OH 45433-7251 to help us maintain a current mailing list.

Copies of this report should not be returned unless return is required by security considerations, contractual obligations, or notice on a specific document.

REPORT DOCUMENTATION PAGE

Form Approved
OMB No. 0704-0188

1. AGENCY USE ONLY *(Leave blank)*	2. REPORT DATE FEB 1994	3. REPORT TYPE AND DATES COVERED FINAL 09/01/88--02/01/94

4. TITLE AND SUBTITLE FEASIBILITY STUDY OF USING NEUTRON DIAGNOSTICS FOR TURBINE ENGINE STRUCTURAL MEASUREMENTS

5. FUNDING NUMBERS
C F33615-88-C-2887
PE 61101
PR ILIR
TA P8
WU 07

6. AUTHOR(S)

DUDLEY LEGGETT (EDITOR / COMPILER)

7. PERFORMING ORGANIZATION NAME(S) AND ADDRESS(ES)
PRATT & WHITNEY CANADA INC
1000 MARIE-VICTORIN
LONGUEUIL QUEBEC J4G 1A1

8. PERFORMING ORGANIZATION REPORT NUMBER

9. SPONSORING / MONITORING AGENCY NAME(S) AND ADDRESS(ES)
AEROPROPULSION AND POWER DIRECTORATE
WRIGHT LABORATORY
AIR FORCE MATERIEL COMMAND
WRIGHT PATTERSON AFB OH 45433-7251

10. SPONSORING / MONITORING AGENCY REPORT NUMBER
WL-TR-94-2054

11. SUPPLEMENTARY NOTES

12a. DISTRIBUTION / AVAILABILITY STATEMENT

APPROVED FOR PUBLIC RELEASE; DISTRIBUTION IS UNLIMITED.

12b. DISTRIBUTION CODE

13. ABSTRACT *(Maximum 200 words)*

THE INTEGRATED INTENSITY AND THE ANGULAR POSITION OF A BRAGG DIFFRACTION PEAK ARE BOTH RELATED TO TEMPERATURE.

A MULTIPHASE TEST PROGRAM, SPECIFICALLY DESIGNED TO EXPLORE NUCLEAR METHODS, HAS DETERMINED THAT STRAINS AND TEMPERATURES IN THE STATIC AND ROTATING COMPONENTS OF A GAS TURBINE ENGINE CAN BE MEASURED NONINTRUSIVELY USING NEUTRON DIFFRACTION TECHNIQUES.

IN PARALLEL WITH THESE EFFORTS, A STUDY CONCLUDED THAT THERE ARE SEVERAL "PORTABLE" NEUTRON SOURCES THAT ARE SUITABLE FOR THE NEUTRON RADIOSCOPIC EXAMINATION OF AN OPERATING GAS TURBINE ENGINE.

14. SUBJECT TERMS

STRAIN, TEMPERATURE, MEASUREMENT, GAS TURBINE, NEUTRON DIFFRACTION

15. NUMBER OF PAGES
106

16. PRICE CODE

17. SECURITY CLASSIFICATION OF REPORT UNCLASSIFIED	18. SECURITY CLASSIFICATION OF THIS PAGE UNCLASSIFIED	19. SECURITY CLASSIFICATION OF ABSTRACT UNCLASSIFIED	20. LIMITATION OF ABSTRACT UL

NSN 7540-01-280-5500

Standard Form 298 (Rev. 2-89)
Prescribed by ANSi Std. Z39-18
298-102

TABLE OF CONTENTS

By ....
Distribution /

Availability Codes

Dist	Avail and / or Special
A-1	

1. OBJECTIVE

The goal of this program was to assess the feasibility of using neutron diffraction techniques or other nuclear methods to measure strain and temperature in an operating gas turbine engine.

2. SUMMARY

A multiphase test program, specifically designed to explore nuclear methods, has determined that strains and temperatures in the static and rotating components of a gas turbine engine can be measured non intrusively using neutron diffraction techniques.

Neutron diffraction applications, previously limited to residual stress measurement and material characterization, were expanded to determine the strain and temperature profiles in a stationary test specimen. This same technique was then repeated successfully on a rotating, heated disc of Waspaloy. Finally, the internal components of a PT6A- gas generator were mapped from the outside to show that a particular volume of interest can be located by the neutron diffraction method.

In parallel with these efforts, a study concluded that there are several "portable" neutron sources that are suitable for the neutron radioscopic examination of an operating gas turbine engine.

To summarize then, this program has successfully demonstrated that it is feasible to use neutron diagnostics to make non invasive measurements on gas turbine engines.

3. BACKGROUND

Calibration of the analytical tools used to determine gas turbine component life is extremely complex by virtue of the experimental techniques currently available. The uncertainties associated with the measurement of strain and temperature in rotating components compromise the verification of gas turbine engine structural design techniques and analytical prediction capabilities. Temperature-limited gauges, aerodynamic probes that protrude into the gas path disturbing flow and the difficulties of extracting signals from rotors, etc., are factors that inhibit today's established instrumentation methods. Future engine designs, which demand higher operating temperatures and tip speeds can only exacerbate this situation.

A non invasive measurement technique that overcomes the above limitations would allow optimum designs to be achieved earlier in the engine development cycle and more confidence to be gained in rotor integrity analyses. Neutron diffraction provides an opportunity to collect this valuable structural data non intrusively.

When an incident beam of neutrons strikes a specimen, it is diffracted at an angle that depends on the distance between the planes of atoms in the crystal lattice. This angle can be measured with a neutron spectrometer and the interplanar spacing

can then be calculated. Any differences resulting from a comparison of total lattice strain and the expected thermal expansion, can be attributed to mechanical loading. Also, once the integrated intensity of the diffraction peak has been determined, the temperature of the material can be deduced through comparison with a standard curve of intensity versus temperature since any change in integrated intensity of the diffraction peaks is related to temperature by the Debye-Waller factor. To reiterate then, neutron diffraction offers the possibility of measuring both strain and temperature in a component independently.

Neutron radioscopy can be used to monitor oil flow in an operating engine and to show the location of any ice formation. "Cold" neutrons have been used for oil imaging analyses for several years but the use of cold neutrons results in a significant increase in system cost and a significant reduction in available neutron flux from a given neutron source. Thermal neutrons, on the other hand, if suitable for imaging purposes, are somewhat cheaper to produce and could be output from a "portable" source.

4.0   RESULTS AND DISCUSSION

Detailed descriptions of the study, test arrangements and discussions of the test data and subsequent analyses, can be found in Appendices A-D. The following sub-sections represent synopses of that information.

4.1   Application Study (Appendix A)

Theoretical calculations, supported by experimental evidence, indicate that 'thermal' neutrons can be used for neutron radiography. A neutron radiograph has shown that a 0.125 mm layer of paraffin (similar attenuation properties as oil) is visible behind 20 mm of Inconel, a nickel-based alloy.

The study of neutron sources also concluded that four suitable accelerators can meet the requirements of "portability".

4.2   Static Calibration (Appendix B)

Two neutron diffraction methods were developed to determine temperature within stationary components non intrusively. The integrated intensity of a diffraction line depends on temperature through the Debye-Waller factor and the angular position of the line, in the absence of applied load, depends on temperature through the thermal expansion coefficient. Temperature of a Waspaloy specimen was thus determined by accurate measurement of the intensity relative to a reference temperature and the interplanar spacing. It was also shown to be practical to measure the strain response to an applied load at elevated temperatures.

The temperatures of the Waspaloy and Ti alloy test pieces were determined by measurement of thermal strain with precision of $\pm 4^0$K and $\pm 5^0$K respectively; these determinations correlated with thermocouple measurements within 5^0K up to 800^0K

2

and 600^0K respectively. Additionally, the intensity measurements indicated that temperatures could be measured independent of load with a precision of 10^0K.

4.3 Dynamic Calibration (Appendix C)

Measurements made on a Waspaloy disc, similar in dimension to an actual turbine disc, spinning at 3000 rpm and heated electrically, confirmed the feasibility of using the neutron diffraction methods developed in the Static Calibration phase for non-invasive measurement of temperature in a dynamic system. Precision corresponding to temperature uncertainties of less than 10^0K can be achieved from measurements of diffraction peak position and intensity.

4.4 Engine Test (Appendix D)

As a precursor to running a gas turbine in the reactor hall, a PT6A- gas generator with an electrically-driven compressor turbine rotor was mounted on the spectrometer. Room temperature diffraction measurements explored beam path limitations and allowed the successful non-intrusive 'mapping' of the internal components in the region of the turbine disc and blades.

5.0 RECOMMENDATIONS

5.1 "Portable" Neutron Sources

The study indicated that several accelerators are capable of generating sufficient neutron flux for thermal neutron radiography. The next logical step in the development is a conceptual design study to address such issues as imaging and target technology, shielding and power requirements and system capital and operating costs.

5.2 Engine Operational Test

The results of Tasks 4.2 through 4.4 have indeed shown that it is feasible to make non-intrusive strain and temperature surveys of the stationary and rotating components of a gas turbine installed adjacent to a reactor using neutron diffraction techniques. However, before the engine operational test can become a reality, certain safety criteria must be satisfied.

(i)   In the unlikely event that any radiation is leaked from the reactor during an incident, the ambient pressure in the reactor hall is always kept below atmospheric, to ensure that this leak is contained within the building. The engine, therefore, must be installed in its own chamber with the intake air ducted into the chamber from the outside of the building; similarly, all exhaust gases must be ducted back outside.

(ii)   The spectrometer, on which the engine is mounted close to the reactor, is accessible to AECL Research personnel. The chamber must have an adequate containment capability (in the unlikely event of an uncontained disc failure) and

3

sufficient noise attenuation to reduce the ambient noise in the vicinity of the spectrometer to an acceptable level. The temperature of the exhaust duct at ground level will be minimized by injecting water (or liquid nitrogen) into a modified turbine support case.

The following paragraphs describe some operating practices and a means of validating the neutron diffraction-derived data.

(iii)   It is planned to run the engine at a constant Measured Gas Temperature (MGT) and both the turbomachinery and installation will be sufficiently instrumented to maintain a safe operation. From the data collected during task 4.4, it was shown to be possible to position the "sampling volume" anywhere on the center line of the disc and traverse radially outwards through the blades and shroud. The depth of scanning is limited only by a maximum material thickness in the beam path of 19mm. The disc can also be traversed axially in the region of the blade roots.

(iv)   Since this statistical method requires sufficient time (as long as 2 hours in some cases) to give adequate resolution of the Bragg peaks, the measured strains and temperatures will be circumferentially-averaged values. Selected stationary components will be sufficiently instrumented to allow comparison between conventional and nuclear techniques.

6.0   ACKNOWLEDGEMENTS

APPENDIX A

NRAY - 7   NEUTRON SOURCES FOR NEUTRON RADIOSCOPY

NEUTRON SOURCES FOR NEUTRON RADIOSCOPY

G.M. MacGillivray, R.S. Davis[1], B.G. Chidley[2], G.E. McMichael[2] and M.A. Lone[3]

---

[1]Reactor Physics Branch
[2]Accelerator Physics Branch
[3]Neutron and Solid State Physics Branch

ABSTRACT

This report examines the requirements at the Arnold Engineering Development Center for a neutron source suitable for the neutron radioscopic examination of operating jet engines under simulated operating conditions in engine test cells. Theoretical calculations, supported by experimental evidence, lead to the conclusion that four accelerators are capable of meeting the requirements, with two of these being cyclotrons and two being radio-frequency quadruple accelerators. The latter are the favored option because of the greater efficiency of neutron thermalization and because of the reduced shielding requirements.

Fuel Materials Branch
Chalk River Laboratories
Chalk River, Ontario, Canada K0J 1J0

1.0   SCOPE

This report examines the availability of neutron sources for the neutron radiographic inspection of operating jet engines at the Arnold Engineering Development Center (AEDC). This study does not consider neutron sources based upon nuclear reactors (excessive licensing delays and costs) or isotopic sources such as californium (available neutron yield too low). Furthermore, subcritical masses of fissile material are not considered, since the safety and licensing difficulties for such a device are similar to those for a nuclear reactor. Only accelerator-based systems are considered.

The calculations that were performed were of a scoping nature and were intended only to provide an indication of the feasibility of the project. Therefore, code calculations are accurate only to a factor of 2. Greater accuracy cannot be obtained at this time because of a lack of specific data related to the exact operational setup and because of the limited funds for the scoping calculations.

Shielding has been considered only in a relative fashion, wherein the shielding requirements for various neutron sources are described in comparison to one another. No attempt has been made to carefully estimate the types and quantities of shielding materials required. Sufficient information is presented to allow some judgment as to the comparative costs of shielding different facilities.

Largely as a result of the above, it was not possible to accurately state the dimensions or mass of any given system. Rather, the systems are ranked as small to large.

2.0   NEUTRON BEAM REQUIREMENTS

To specify the requirements of the neutron beam, it is necessary to consider three separate criteria: the intensity of the beam, the energy of the neutrons, and the purity of the beam. More importantly, it is necessary to understand the nature of the specific application.

2.1   Application

AEDC is interested in neutron radioscopy for the examination of operating gas turbine engines under representative conditions of temperature, pressure and airflow. Ideally, such a system would show the location(s) of lubricant within the engine and the location of any ice formation. Lacking other information, layers of ice or water are assumed to be of interest only if the thickness of the layer exceeds 0.1 mm. Examination of a Pratt and Whitney Canada PT6 engine and observations from a USAF F-100 engine drawing, suggest that about 20 mm of Inconel must be penetrated to see the areas of interest. Spatial resolution is more difficult to establish a specification for, but it is important to do so because a specification for the collimation ratio of the neutron beam collimating system is derived from it--a ratio that impacts enormously upon the final intensity of the neutron beam. If it is

assumed that the maximum allowable geometric unsharpness is 1.5 mm, and that the total beam path through the area of interest does not exceed 75 mm (from the object of interest to the image plane), then a collimation ratio of 50 can be established (75/1.5). The fundamental system requirements, then, are that layers of water or oil 0.1 mm thick be imaged through 20 mm of Inconel with a maximum geometric unsharpness of 1.5 mm.

2.2 Neutron Flux

The requirement that the imaging be done in real-time places a constraint upon the allowable neutron flux. Given the available imaging technologies (from either Precise Optics or LTV Defense and Aerospace), a neutron flux at the image plane of 1.0×10^6 n/cm^2.s is required in order to ensure that sufficient signal strength is obtained to generate 30 frames of video data per second.

2.3 Neutron Energy

Widely published work[1] has shown that cold neutrons can be used to perform an examination similar to the one described here. However, the use of cold neutrons results in a significant increase in system cost and in a significant reduction in available neutron flux from a given neutron source. Neutron cross-section data were examined in an attempt to estimate the likelihood that thermal neutrons would be able to penetrate the Inconel and image the layer of water or oil.

Figure 1 shows the transmission of neutrons through Inconel and through oil as a function of neutron energy. In Figure 1, transmission of neutrons through Inconel is shown as the thickness of Inconel that will allow transmission of 1% of the beam (allowing sufficient intensity in the transmitted beam for imaging), and the transmission of neutrons through oil is shown as the thickness of oil that will allow the transmission of 5% of the beam. Here, it is desirable to penetrate the greatest thickness of Inconel and to penetrate the least thickness of oil. From this it is evident that cold neutrons (0.004 eV) will provide better contrast between oil and Inconel than will thermal neutrons (0.023 eV). However, thermal neutrons will provide sufficient contrast to be visible and are capable of penetrating the necessary thickness of Inconel. Thus, while cold neutrons would be superior for the examination in question, thermal neutrons are adequate.

To verify that thermal neutrons could image oil behind Inconel, a test piece was prepared (see Figure 2). This test piece comprises an Inconel step wedge with an aluminum tray. The aluminum is grooved perpendicular to the length of the Inconel steps and the grooves are filled with paraffin, which attenuates neutrons approximately the same as does oil. A neutron radiograph (Figure 3) of the test piece shows that the thinnest layer of paraffin (0.125 mm) is visible behind the thickest Inconel step (20 mm), confirming the analytical results of Figure 1. The test piece was sent to JRC Petten in the Netherlands for cold-neutron radiography. A print of the cold-neutron radiograph obtained is presented as Figure 4. As expected, only slightly more contrast is available with the cold neutrons than with the thermal neutrons.

Therefore, it is not necessary to use cold neutrons in order to perform these examinations; thermal neutrons are adequate.

2.4 Beam Purity

All neutron beams are contaminated with gamma rays and with neutrons of other than optimal energy. Also, neutrons scattered within the facility can degrade the quality of the generated images. The effect of scattered neutrons can be minimized through careful design of the beam collimation system, and particularly through the choice of materials for the walls of the collimator. Neutrons at energies other than that required will degrade the image only if the imaging system is sensitive to them and only if they are abundant. Generally, it is possible to minimize the effects of undesired neutrons by carefully designing the moderator and the aperture assemblies, thereby removing such neutrons from the beam. The question of gamma-ray contamination is somewhat more complex.

For neutron radiography using gadolinium conversion foils and film, it is generally accepted that the best results are obtained when the neutron to gamma ratio is greater than 10^6 n/cm^2.mR. This is a difficult condition to meet, particularly for small, low-intensity neutron sources. However, the gadolinium oxysulphide or ^{6}Li-ZnS scintillator screens used for neutron radioscopy are generally less sensitive to gamma rays than the X-ray film used in radiography. Moreover, it is usual practice in the design of a neutron radioscopy system to place a mirror and a right angle between the scintillator and the imaging system proper. This practice ensures that neither neutrons nor gamma rays from the direct beam are able to impinge directly upon the television camera or diode array. Normally, the neutron to gamma ratio is not a problem for a neutron radioscopy system. If a specification is required, any ratio greater than 10^3 n/cm^2.mR is sufficient.

3.0 NEUTRON SOURCE REQUIREMENTS

From the available data on the production of neutrons from charged particle accelerators and from the known behavior of neutrons during moderation, it is possible to estimate the neutron flux that will result from a particular beam (particle, energy and current) striking a particular target. The systems of interest involve beams of protons or deuterons striking targets of tritium, lithium or beryllium.

3.1 Target

The target that is struck by the charged-particle beam is a critical system component and must be fabricated of either beryllium or lithium in order to generate the required neutron yields. The energy deposition in the target (and the requirement to remove that energy) introduces a substantial complication in the design of the system. Typical systems would require the removal of about 10 kW from a target area that is likely about 50-100 cm^2 in area and on the order of 1 mm thick. The most promising candidate for such a target is a falling curtain of liquid lithium, although a spinning disk of beryllium is also a reasonable approach. Both target concepts would require some development work.

3.2   Neutron Production

Here, we seek the number and energy distribution of neutrons produced by a particular particle of given energy striking a particular target. Unfortunately, data here are limited. While the emission of neutrons in the forward direction is well understood, the emission over 4π is poorly understood. We assume that half of the generated neutrons are emitted in the forward direction, and that the energy distribution is identical in all directions. Thus, we prepared a series of graphs showing neutron yield as a function of energy for a given beam/target interaction, with a different curve for each energy of the incident charged particle.

3.3   Neutron Moderation

The moderation of neutrons is not a trivial subject, but simplifications can be made that allow for reasonable estimations of the thermal neutron flux that will result from the moderation of neutrons of a given energy. From the earlier calculations, we have data relating neutron yield to neutron energy for each beam/energy/target combination. For each case then, the final neutron flux (per incident charged particle) is simply the sum of the contributions made by neutrons at each different energy level. We can now convert the earlier data into a curve for each target-beam system that shows specific neutron flux (neutron flux per incident charged particle) as a function of beam energy.

Since the detailed design of both the moderator and the aperture assembly will affect the obtained neutron flux, and since the precise energy spectrum from a given neutron source cannot be calculated exactly without experimental verification of the neutron yields over 4π, the moderator effectiveness calculations are accurate only to within a factor of two.

3.4   Source Strength

As shown in section 2.2, the flux at the sample plane must be 10^6 n/cm^2.s in order to perform real-time neutron radioscopy. Furthermore, the flux at the image plane is known to be well-approximated as one-sixteenth of the flux at the aperture divided by the square of the collimation ratio. Since the collimation ratio here should be at least 50, it follows that the neutron flux at the aperture must be at least 4×10^{10} n/cm^2.s.

Since we now know the neutron flux requirements, and the specific neutron flux for each beam/energy/target case, we can calculate the beam current as a function of beam energy. These data are presented as Figure 5. Note that only small differences are evident between systems using lithium targets and those using beryllium targets. A general conclusion from Figure 5 is that the beam current requirement becomes lower as the beam energy increases.

4.0   POTENTIAL NEUTRON SOURCES

Particle accelerators are generally optimized for the production of particles of a specific energy. Each different type of accelerator has a niche of energy that it is

best able to produce. The two accelerator types that seem to best fit the requirements of AEDC are radio-frequency-quadruple (RFQ) linear accelerators (Linacs) and cyclotrons. The cyclotrons generally produce higher energy and lower current than do the RFQ-Linacs.

Figure 5 contains an overlay showing the capabilities of several specific accelerator concepts. Of these, four specific accelerators appear to meet the stated technical requirements, two being RFQ-Linacs (PL-11 and CANUTRON) and two being cyclotrons (Oxford and a TR-30 such as the one at TRIUMF)

4.1   RFQ Linacs

4.1.1 CANUTRON

CANUTRON is a conceptual design for an RFQ-Linac developed at AECL Research that uses a high-current, low-energy beam of protons striking a lithium target to generate neutrons. This results in a relatively low energy in the generated neutrons, which can therefore be moderated quite efficiently. The low energy of the primary beam limits the amount of primary shielding required. This accelerator operates at a 100% duty factor; it is not a pulsed accelerator.

4.1.2 PL-11

The PL-11 is a conceptual design comprising an RFQ and a Drift-Tube Linac developed by AccSys Technologies that uses a moderate-current, moderate-energy beam of protons striking a lithium target to generate neutrons. This system would require somewhat more shielding on the accelerator proper than would CANUTRON, because of the higher energy of the beam. This is a pulsed accelerator.

4.2   Cyclotrons

4.2.1 TR-30

A TR-30 cyclotron, manufactured by EBCO, is being operated by the group at TRIUMF for the production of radioisotopes. This accelerator could be readily adapted to the use at hand. It is a high-energy, low-current accelerator.

4.2.2 Oxford

Oxford Instruments design and market a small super-conducting cyclotron that is easily capable of meeting the stated requirements of this program. Shielding requirements for the primary beam will be intermediate between those of the TR-30 accelerator and those of the PL-11.

5.0   SIZE AND MASS

The requirements of each of the four accelerator-based systems referred to above in terms of floor area and load capacity differ in detail only. All require large power supplies, and all require significant amounts of shielding. In all cases, for given neutron flux at the image plane, equivalent amounts of shielding will be required at the sample end of the system, but the amount of shielding required at the target/moderator assembly differs significantly.

5.1   Shielding

5.1.1   Target/Moderator Area

Most of the shielding required in the whole assembly will be in the target/moderator area. In the vicinity of the target assembly and the moderator surrounding it, the incident beam of charged particles is converted into neutrons that are subsequently moderated to thermal energies. The radiation that require shielding here are gamma rays, produced during the formation and moderation of the neutrons and by the interaction of neutrons and other materials, and fast neutrons. The fast neutrons are simply those that have not been slowed to thermal energies upon reaching the outer wall of the moderator vessel. The solution here is to increase the size of the moderator, to perhaps 1.5 m diameter. The outer wall of the moderator assembly would require a thin layer of neutron-absorbing material (boron for example) and lead shielding to stop gamma rays. The lead shielding would likely have to be at least 15 cm thick. The amount of shielding depends very strongly upon the energy of the generated neutrons and therefore upon the energy of the particle beam. Therefore, CANUTRON would require the least shielding in this area, followed by the PL-11, the Oxford cyclotron and the TR-30.

5.1.2   Sample Area

The second most significant amount of shielding will be required in the sample area, principally behind the image plane. In the sample area the entire neutron beam must be absorbed. Most of the neutrons will ultimately yield gamma rays at some energy. A neutron-absorbing beam material that yields few gamma rays (e.g., boron or lithium) should be placed behind the sample and image-capture system. A beam-stop behind the sample and covering an area slightly larger than the beam area must be provided, that reduces neutron and gamma dose rates to acceptable levels. The radiation sources include both the primary beam and secondary radiation from the sample and imaging systems. The beam-stop proper will require about 15 cm of polyethylene, about 5 cm of borated polyethylene and about 15 cm of lead in order to reduce the dose rate on contact behind the beam stop to 2.5 mR/h. The amount of shielding required will be substantially reduced if personnel access is restricted. Areas outside the direct beam path will require substantially less shielding (a factor of 2 to 5 less than required in the beam stop is likely), but the details are contingent upon the permitted contact radiation field.

5.1.3 Accelerator

The component of the system requiring the least shielding is the accelerator itself. The primary source of radiation in the accelerator is from X-rays produced from stray electrons accelerated in the RF fields. A secondary source of radiation is from neutrons produced when part of the charged-particle beam spills onto adjacent materials. The principal radiation here is X-rays (or gamma rays), and suitable personnel shielding would have to be provided. Thus, the shielding on the beam path would be lowest for CANUTRON and highest for TRIUMF, with PL-11 and Oxford intermediate between these extremes. Only 5-10 mm of lead is required for any of the accelerators.

5.2   Power Supply

In all cases, the accelerator will require a large power supply, typically occupying 5-6 m^2. This can be separated to some extent from the accelerator proper. There will be some variation in the type and size of the power supply.

5.3   Exclusion Zone

For those areas that cannot be adequately shielded for some reason, it will be necessary to bar the access of personnel. Generally, this is not a differentiating characteristic, but one that is common to all of the accelerators. The dimensions of the exclusion zone cannot be calculated without a more exact shielding design, but exclusion zones of 1-5 m in various directions would substantially reduce the shielding requirements.

5.4   Accelerator Proper

The cyclotrons require about the same amount of floor space as does CANUTRON, at about 3 m^2, while the PL-11 requires about 10 m^2.

6.0   CONCLUSIONS

1)   Thermal neutrons can be used.
2)   The collimation ratio must be at least 50.
3)   The neutron flux at the sample must be at least 10^6 n/cm^2.s.
4)   The neutron flux at the aperture must $> 4 \times 10^{10}$ n/cm^2.s.
5)   Several accelerator designs exist that can be used.
6)   RFQ-Linacs and cyclotrons are possibilities.

The RFQ-Linac, with or without a drift-tube Linac, and with a solid beryllium target, is the most promising candidate technology, principally because of the lower beam energy, which yields a lower requirement for shielding the charged-particle path, and because of the reduced energy of the neutrons produced, which increases the thermalization efficiency, thereby reducing the requirement for shielding in the target area. Pulsed systems such as those produced by Accsys Technology Inc., or

100% duty factor systems such as the CANUTRON, can be used, where the choice will be influenced somewhat by the details of the imaging system selected. The lower energy of the CANUTRON concept is a definite advantage in reducing the shielding requirements in the target/moderator area.

7.0   RECOMMENDATIONS

This study has shown that a variety of accelerators are capable of generating the required neutron flux. A more careful study of specific siting requirements and constraints would be required before a particular accelerator design could be chosen.

A conceptual design study would address the following questions:

1) Choice of imaging system,
2) Shielding requirements for in-cell components,
3) Power requirements,
4) Choice of accelerator,
5) Choice of target technology,
6) Installation costs, and
7) System capital and operating costs.

The conceptual design study would also have to extend the work of this study where such extension was necessary to better specify the necessary system components. For example, a mock-up comprising the materials found in a cross-section of a typical engine, and containing areas with water, ice or oil of suitable thickness, should be manufactured and tested to ensure that sufficient contrast is available. Once the system geometry is specified, then detailed calculations can be conducted to allow substantially more accurate determinations of beam energy and current requirements. This work should be augmented by improved nuclear data regarding the neutron yields over 4π of the most promising nuclear reactions (i.e., Li(p,n), Be (p,n), Li(d,n) and Be(d,n)). Improved accuracy in the calculations will reduce the need to over-design the system, and will ultimately reduce the capital cost of the facility.

8.0   REFERENCES

1.   P.A.E. Stewart, "Aero Engine Applications of Cold Neutron Fluoroscopy at Rolls-Royce Limited", Proceedings of the First World Conference on Neutron Radiography, San Diego, California, 1981, D. Reidel Publishing Company, Holland.

Neutron Transmission Distances
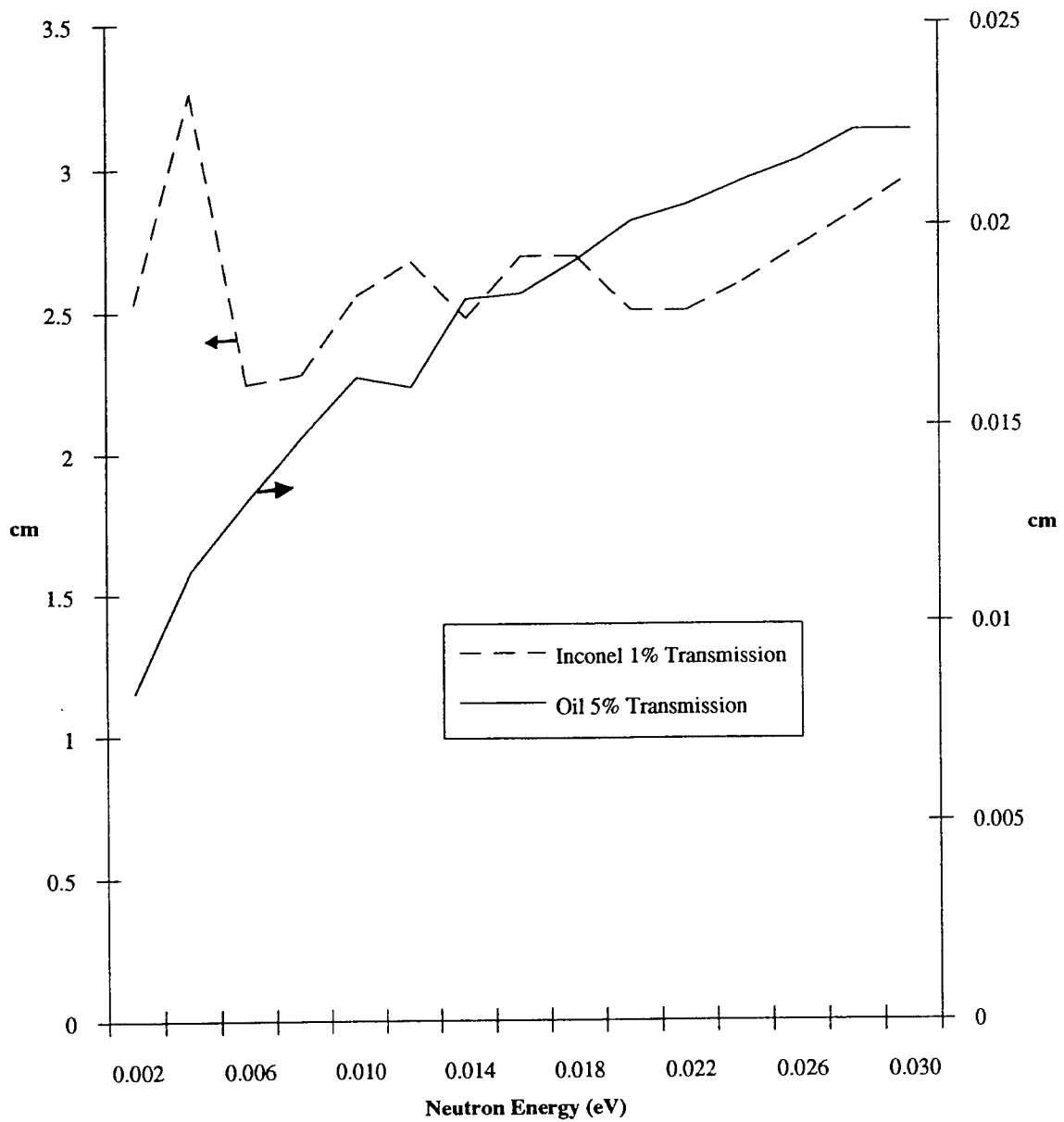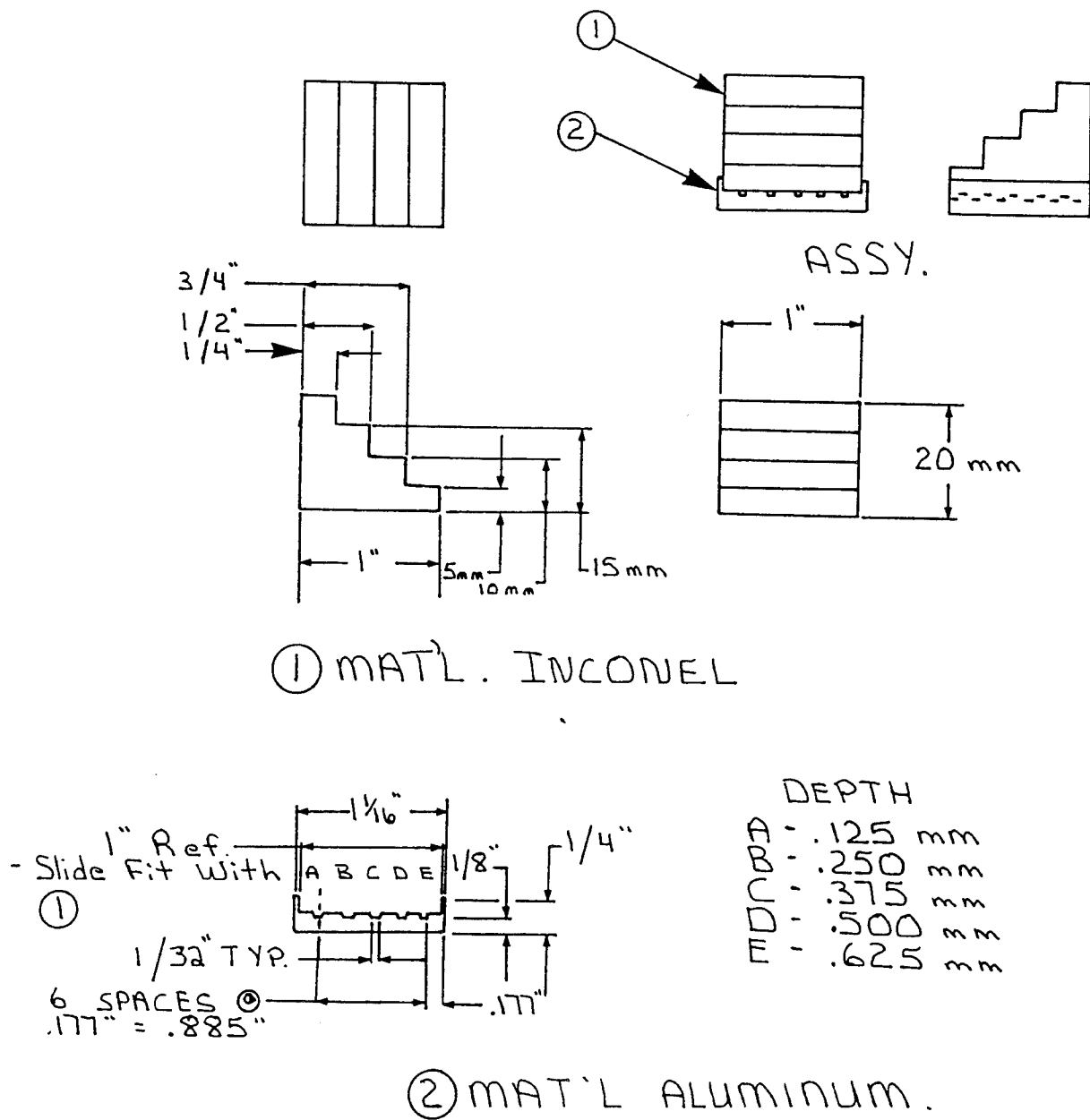## versus Neutron Energy

Figure 1   Available Contrast

ASSY.

① MAT'L . INCONEL

- Slide Fit With ①

1" Ref

DEPTH
A - .125 mm
B - .250 mm
C - .375 mm
D - .500 mm
E - .625 mm

1/32" TYP.

6 SPACES @ .177" = .885"

② MAT'L ALUMINUM.

Figure 2   Contrast Test Object
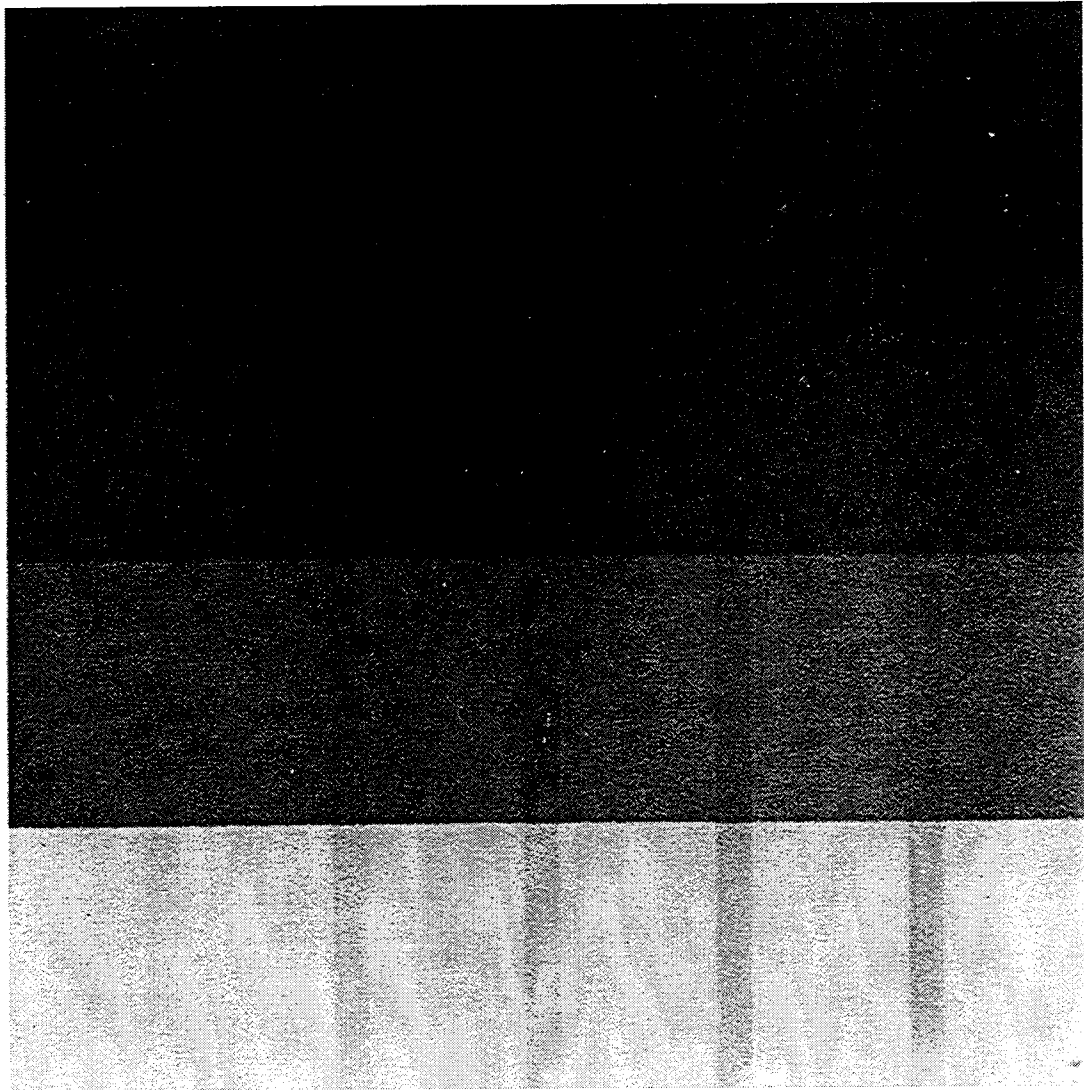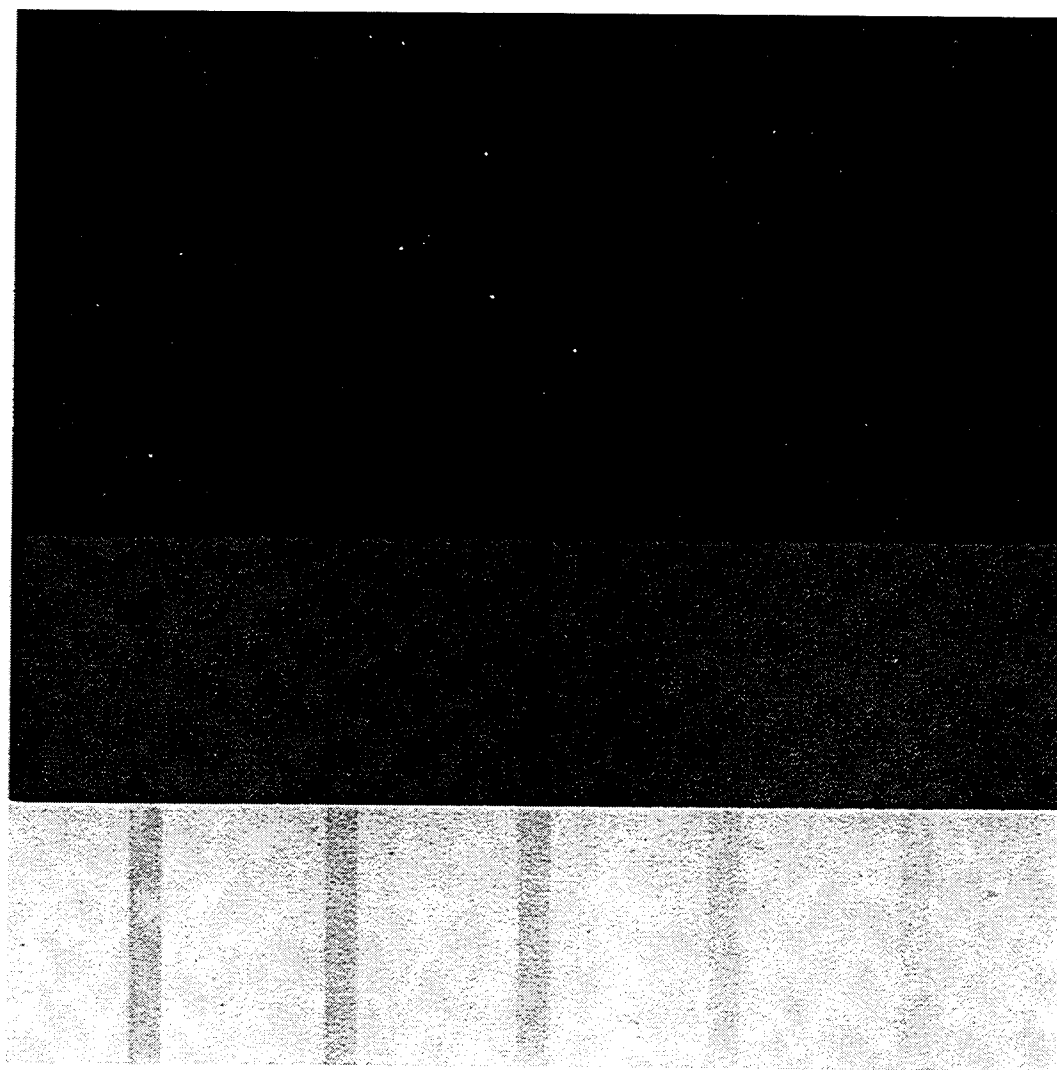
Figure 3 Thermal Neutron Radiograph

Figure 4   Cold Neutron Radiography

**Accelerator Beam Current
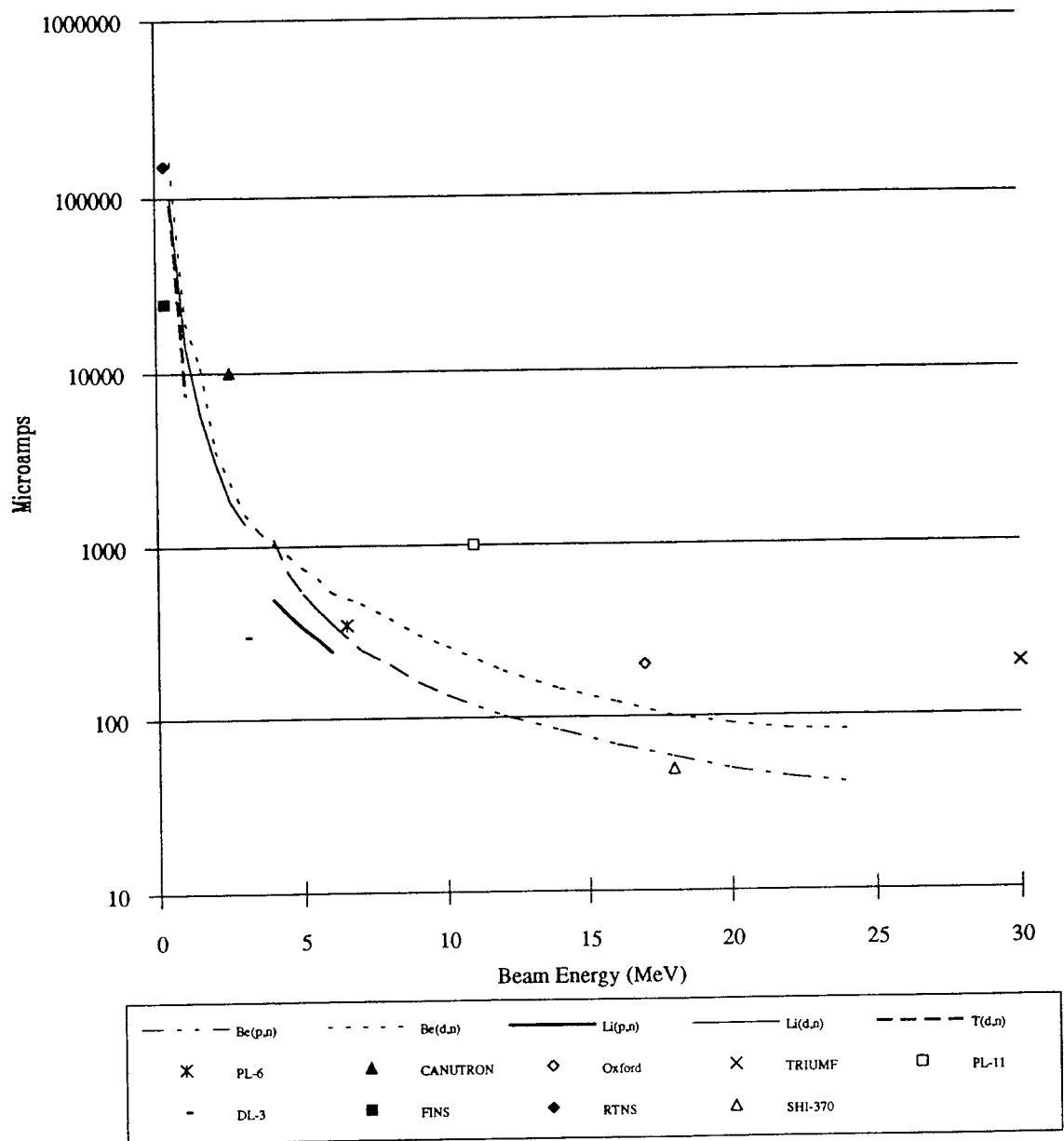versus Beam Energy**

Figure 5 Current Required versus Beam Energy

19

APPENDIX B

ANDI - 38 MEASUREMENT OF STRAIN AND TEMPERATURE FOR WASPALOY AND THE TITANIUM ALLOY AMS 4928 UNDER CONDITIONS OF STATIC LOADING

Atomic Energy Of Canada Limited

MEASUREMENT OF STRAIN AND TEMPERATURE
FOR WASPALOY AND THE TITANIUM ALLOY AMS 4928
UNDER CONDITIONS OF STATIC LOADING

T.M. Holden, J.H. Root, D.C. Tennant and D. Kroeze

ABSTRACT

Two methods have been developed to determine temperature non-invasively within engineering components by neutron diffraction. The integrated intensity of a diffraction line depends on temperature through the Debye-Waller factor. The angular position of the line, in the absence of an applied load, depends on temperature through the thermal expansion coefficient. Temperature may thus be determined by accurate relative intensity measurements with respect to a reference temperature and, alternatively, by accurate measurements of interplanar spacing. It was also shown to be practical to measure the strain response to an applied load at elevated temperatures.

Neutron and Solid State Physics Branch
AECL Research,
Chalk River,
Ontario, Canada
K0J 1J0

I.   INTRODUCTION

The measurement of the temperature of aero-engine components is an important task of engine diagnostics. Present methods involve the use of slip rings to bring thermocouple leads out of the engine or remote telemetry methods, both of which require modifications to the engine under test. Methods which hold the promise of being able to measure temperatures non-invasively without special modification are therefore of great interest. Four methods have recently been proposed, epithermal neutron resonance thermometry[1,2,3], γ-ray[4] resonance thermometry, Mossbauer spectroscopy and thermal neutron diffraction. Prototype experiments[1-3] have already been carried out to measure temperatures by epithermal neutron resonance thermometry and impressive accuracy, $\pm 5^{0}K$, has been achieved for the limited isotopic species for which the method can be expected to work. Neutron diffraction can be applied to any engineering material and gives comparable accuracy. The only materials to which it may not be applied are highly absorbing isotopic species much as Gd, Cd or B. There are two ways neutron diffraction may be used to measure temperature. By measuring the change in lattice spacing, the temperature may be found by comparison with macroscopic measurements of thermal expansion.   Alternatively, the decrease of integrated intensity of the diffraction peaks is directly related to temperature via the Debye-Waller factor. With accurate intensity measurements and comparison with a standard curve of relative intensity versus temperature, the temperature can be deduced. Lattice spacing are also influenced by the stress state of a component. By combining measurements of the diffraction peak position and its intensity, neutron diffraction offers the possibility of measuring both the temperature and stress state of the part under study.

The present report describes the results of experiments designed to check the practicality of the measurements and to discover the difficulties in the path of realizing the potential of the method. Calibration constants for Waspaloy were determined to link the temperature of the material to measurable parameters of diffraction peaks, the peak position and integrated intensity. The experiments were also designed to measure the strain response to a known static stress at an elevated temperature. Further phases of the experiment will address the measurement of a thermal gradient in a rotating disc.

The balance of the paper is organized as follows:

The second section gives the basic formulae for neutron diffraction and definitions of the measured strains. The third section provides a description of the experimental equipment used for the measurements and the details of the neutron scattering method. The results of the experiments on Waspaloy and titanium alloys are described on the fourth section. Problem areas are identified in the fifth section.

2. BASIC THEORY OF THE METHOD

2.1 Neutron Diffraction

The number of neutrons diffracted per second into the counter, I, for the (hkl) diffraction peak in terms of the number of neutrons per unit area, I_0, striking a cylindrical sample completely bathed in the neutron beam is

$$\frac{I}{I_0} = \frac{\lambda^3 l_s}{8\pi r} \; V \; N_c^2 \, j \; \frac{1}{\sin\theta \, \sin 2\theta} \; T_{hkl} \; F_{hkl}^2 \; A_{hkl} \; \varepsilon^{-2w} \tag{1}$$

In Eq. (1) V is the volume of sample in the beam, A_{hkl} is the known absorption factor which is temperature independent, l_s is the height of the counter at a distance r from the sample, j is the multiplicity of the reflection, N_c is the number of unit cells per cm^3, F_{hkl} is the known structure amplitude of the reflection, and ε^{-2w} is the Debye-Waller factor. The scattering angle, 2θ, is the angle between the incident and outgoing beam and T_{hkl} is the texture of the hkl reflection for the sample orientation. For a completely random grain orientation $T_{hkl} = 1$. In general processing, metal samples orients the grains so that $T_{hkl} \neq 1$. However, it is expected to be a constant independent of the temperature for a given orientation. The wavelength of the neutron beam is denoted by λ. Equation (1) holds for the cylindrical sample geometry used in the experiments.

The relationship between the angle of diffraction and the interplanar spacing, d_{hkl} of the (hkl) plane is given by:

$$\lambda = 2d_{hkl} \; \sin\theta_{hkl} \tag{2}$$

In order to establish the feasibility of measuring mechanical strains at high temperatures, known stresses were applied to the sample, and the change in the d-spacing measured for each of several reflections. The mechanical strain response to the applied stress is

$$\varepsilon_{hkl} = [d_{hkl}^{\sigma} (T) - d_{hkl}^{0} (T)] / d_{hkl}^{0} (T) \tag{3}$$

where d_{hkl} is the d-spacing at applied stress σ and d^0 is the d-spacing for an unstressed sample. Likewise the thermal strain in the lattice is given by

$$\varepsilon_{hkl}^{th} = \frac{d_{hkl}^{\sigma}(T) - d_{hkl}^{0}(T_{REF})}{d_{hkl}^{0}(T_{REF})} \qquad (4)$$

where the reference temperature, T_{REF}, was chosen to be just above room temperature to make temperature control easier. The thermal strain is related to the macroscopic coefficient of linear expansion, $\bar{\alpha}$, where the bar signifies an average between the reference temperature and some required temperature, T, by

$$\varepsilon_{macro}^{th} = \bar{\alpha}(T)\ (T - T_{REF}) \qquad (5)$$

If ε_{hkl}^{th} is independent of hkl, and we assume $\varepsilon_{hkl}^{th} = \varepsilon_{macro}^{th}$, then we may use data compilations of e_{macro} as a calibration curve to derive the temperature from ε_{hkl}^{th}.

In the present experiments the stress was applied vertically and the strain response was measured in the horizontal plane, so that in terms of the applied stress, σ, the bulk strain is:

$$\varepsilon_{bulk} = -\frac{\sigma}{E} \cdot \upsilon \qquad (6)$$

where E is the polycrystalline bulk modulus and υ is Poisson's ratio. In a diffraction experiment we measure not ε_{bulk}, but the response in a particular direction of the set of correctly oriented grains as constrained by their neighbouring grains. The "diffraction elastic constants" vary with the choice of diffraction line as characterized by the Miller indices (hkl) in a manner described by Noyan[7] and Cohen and Dolle[8] for the three constitutive models of polycrystalline materials, the Voigt, Reuss and Kröner models. The Kröner elastic constant is[8] S_1 (hkl), corresponding to υ/E,

$$S_1\ (hkl) = S_{3311} + t_{3311} + t_o\Gamma_{hkl} \qquad (7)$$

where S_{3311} and t_{3311} and t_o are functions of the single crystal elastic constants and Γ_{hkl} is given by:

$$\Gamma_{hkl} = \frac{h^2k^2 + k^2l^2 + l^2h^2}{(h^2 + k^2 + l^2)^2} \tag{8}$$

Equations (7) and (8) predict the right sense of the anisotropy for the different reflections. The calculated Kröner elastic constants S_1 (hkl) are 1.68, 1.26, 1.01 and 0.78 x 10^{-3} $(GPa)^{-1}$ for the (002), (113), (220) and (111) reflections. These values were determined from the single crystal elastic constants of $Ni_{80.4} Cr_{19.6}$ as the nearest concentration to Waspaloy to be found in the literature.

The Debye-Waller exponent is conventionally written[9] as:

$$W = \frac{B\sin^2\theta}{\lambda^2} \tag{9}$$

where B, a characteristic property of the material, is related to the mean square amplitude of vibration of an atom on its site, $<u^2>$, by:

$$B = 8\pi^2 <u^2> \tag{10}$$

Over a wide temperature range, the mean square amplitude of vibration of an atom increases with temperature in a nearly linear fashion and therefore the intensity of a given peak decreases with temperature. The Debye-Waller exponent in (9) also increases with $\sin^2\theta/\lambda^2$ so that the effects are more marked for high angle reflections than for low angle peaks. A cubic material, with one atom per unit cell, is characterized by a single B-value whereas for hexagonal close-packed materials such as Ti, where there are two atoms per unit cell, two such factors are, strictly speaking, needed.

The expression for the amplitude of vibration of an atom at temperature T in terms of the normal modes of vibration, w, of the material is:

$$<u^2> = \frac{h}{2\pi M} \int d\omega \frac{Z(\omega)}{\omega} \left(\frac{1}{2} + \frac{1}{\varepsilon^{hw/kt} - 1} \right) \tag{11}$$

where $Z(\omega)$ is the number of normal modes with frequency between ω and $\omega + d\omega$, and the term in curly brackets is the mode population factor. $Z(\omega)$ is known for most elements, including Ni, from single crystal inelastic neutron scattering measurements although not for Waspaloy (a complete tabulation of $Z(\omega)$ for the

elements is given in reference 10).

When $Z(\omega)$ is unknown, it is often written in the Debye approximation with

$$Z(\omega) = \frac{3\omega^2}{\omega_D^3} \quad \text{for} \quad \omega < \omega D$$

$$= 0 \qquad \omega > \omega D \tag{12}$$

The Debye cut-off frequency, ω_D, is related to the Debye temperature, θ_D, by $\frac{h\omega}{2\pi} = k\theta_D$ where h is Planck's constant and k is Boltzmann's constant. The integral of Equation 11 may be carried out with the approximations of Equation 12 and yields:

$$<u^2> = \frac{3h^2}{4\pi^2 M} \frac{1}{K\theta_D} \left(\frac{1}{4} + \frac{T}{\theta_D} f \left(\frac{\theta_D}{T} \right) \right) \tag{13}$$

where M is the atomic mass and $f\left(\frac{\theta_D}{T}\right)$ is the well-known Debye integral:

$$f\left(\frac{\theta_D}{T}\right) = \frac{T}{\theta_D} \int_0^{\theta_D/T} \frac{\chi \, d\chi}{e^\chi - 1} \tag{14}$$

If we make a high temperature expansion for $\frac{T}{\theta_D}$ we obtain for the temperature dependence of B the following expression.

$$B = \frac{6h^2}{M} \frac{1}{K\theta_D} \frac{T}{\theta_D} \left(1 + \frac{\theta_D^2}{36T^2} - \frac{\theta_D^4}{3600T^2} + \cdots \right) \tag{15}$$

where the second term makes a 6% correction and the third term a 0.1% correction

at room temperature for nickel.

Values of B for Ni have been obtained by neutron diffraction[11] and x-ray diffraction[12], 0.426 ± 0.009 and 0.37 ± 0.02 $\mathring{A}^2$ respectively. These do not agree well. From Equation (15) we find that the value of θ_D corresponding to the value $0.426\mathring{A}^2$ is $\theta_D = 374 \pm 4^0K$.

The parameterization of the problem in terms of a Debye temperature gives a qualitative guide to the temperature dependence although it is not accurate. This is partly because it ignores the real structure in $Z(\omega)$ which is particularly relevant to hexagonal-close-packed metals like titanium where there are two atoms per unit cell. The calculations of Sears and Shelley[10] partly address this point because they have used the experimental measured density of vibrational states, as determined by inelastic neutron scattering to calculate the Debye-Waller factor as a function of temperature for most elements, including nickel and titanium. For Ni there is a discrepancy among the various experimental measures of B as noted above and the calculation $(0.34 \pm 0.01$ $\mathring{A}^2)$.

The discussion up to this point has used a harmonic model of the lattice in which the atoms are assumed to move in a quadratic potential. Additional anharmonic terms become important at high temperatures and deviations occur from the harmonic model. The influence of anharmonic terms has been extensively discussed by Willis and Pryor[13]. They write (Equation 5.386)

$$B = B_{harmonic} \left(1 + T \left(2 \chi \gamma_G - 20 \frac{k\gamma}{\alpha^2} \right) \right) \tag{16}$$

where γ_G is the Gruneisen parameter, χ is the coefficient of volume expansion and α and γ are the related to the magnitudes of harmonic and anharmonic terms in the potential.

Finally, the measurements which we have made did not employ energy analysis to remove the contribution under the diffraction peak from inelastic "thermal diffuse scattering". Strictly speaking the integrated intensity attributed to elastic diffraction, and hence the Debye-Weller factor, is overestimated in measurements with no analyzer. With all these considerations the best procedure is to derive a curve of intensity versus temperature for an instrumented polycrystalline standard sample and to use this calibration curve to derive the temperature from measured intensities in the same way as the macroscopic thermal strain curve is used in the computation of temperatures from measured thermal strains.

We consider now a simple method of presenting the experimental data so as to facilitate setting up a calibration curve. In order to take out the effects of the

constants in Equation 1 the ratio of the intensity at temperature T to that at the reference temperature is constructed

$$\frac{I'_T}{I'_{REF}} = e^{-\frac{2}{\lambda^2}(B_T \sin^2\theta_T - B_{REF}\sin^2\theta_{REF})} \tag{17}$$

where the primed quantities refer to the intensity corrected for the small angular shifts in the $\sin\theta\sin2\theta$ term in the denominator of Equation 1. This may be rewritten as:

$$\ln\left(\frac{I'_T}{I'_{REF}}\right) = -\frac{2 B_{REF} \sin^2\theta_{REF}}{\lambda^2}\left(\frac{B_T \sin^2\theta_T}{B_{REF} \sin^2\theta_{REF}} - 1\right) \tag{18}$$

The correction term $\sin^2\theta_T/\sin^2\theta_{REF}$ is less than 1% over the whole range of temperature and

$$\frac{B_T}{B_{REF}} = \frac{T}{T_{REF}} \tag{19}$$

to within 3% over the whole range of temperature. Then we have

$$\ln\left(\frac{I'_T}{I'_{REF}}\right) = -\frac{2 B_{REF} \sin^2\theta_{REF}}{\lambda^2} \cdot \frac{T-T_{REF}}{T_{REF}} \tag{20}$$

This suggests that the natural logarithm of the intensity ratio of a given peak is approximately proportional to the temperature increment above the reference temperature. We will therefore use the experimental data to test this form, and to determine the value of B_{REF} for Waspaloy. The slope depends on the factor $2\sin^2\theta_{REF}/\lambda^2$, which from Bragg's Law is $(h^2 + k^2 + l^2)/a^2$ for cubic crystallographic symmetry. It is thus possible to derive a universal curve for all the diffraction lines by dividing the reduced intensity by the appropriate value of $\frac{2\sin^2\theta_{REF}}{\lambda^2}$.

A further level of approximation may also be adequate to describe the temperature dependence of the diffraction peak intensity. In Eq. 17 we may immediately linearize the experimental function, and collect constant factors into a single, material-dependent constant, C, to obtain

$$\left(1 - \frac{I'_T}{I'_{REF}} \right) / (h^2 + k^2 + l^2) = C\,(T - T_{REF}) \tag{21}$$

The experimental data will also provide a test of this calibration method, and determine the value of C for Waspaloy.

3.0 EXPERIMENTS

3.1 Loading Equipment

The load was applied to the sample with an adapted "Creep Rupture Machine" mounted on the L3 spectrometer at the NRU reactor, Chalk River. A schematic diagram of this equipment is shown in Fig. 1. A photograph of the apparatus is shown in Fig. 2. The major adaptation was the replacement of dead-weights by a computer-controlled cantilever arrangement on the "long" arm of the machine. Three 5-lb loading discs were mounted on the platform of a linear translator which is driven back and forth by means of a stepping motor under spectrometer control. The precise load applied on the long arm was measured with a load cell.

Two load cells were calibrated by measuring the response to known added weights. The mechanical advantage of the creep rupture equipment, nominally 10, was measured by adding known weights on the long arm and measuring the load on the short arm with the calibrated load cells. In this way the mechanical advantage of the equipment was found to be 9.95 ± 0.04 and this factor was used to calculate the stress on the sample.

The use of the modified creep rupture equipment had an important bearing on the design of the experiment. In order to obtain stresses as high as 150 MPa (21 ksi) with the maximum load that could be applied to the loading rig, the diameter of the samples had to be 4.8 mm. With lower stresses the strain response would have been too small to measure accurately. The diameter of the sample was then however, about a factor of two less and the volume a factor of four less than desirable from the viewpoint of optimizing the intensity of the neutron diffraction.

3.2 The Furnace

The load was transmitted to the samples through stainless steel pull-rods threaded to vanadium rods near the furnace. The arrangement of the pull-rods, the heaters, the sample and the surrounding furnace is shown in Fig. 3. The pull-rods were

12.7 mm diameter stainless steel, threaded to 12.7 mm diameter vanadium in the furnace. Each vanadium piece had a 1/32" female thread into which the threaded samples were screwed. Vanadium was chosen because it gives incoherent scattering only, with no diffraction peaks and only adds to the background. Two heater assemblies were bolted to the vanadium rods above and below the sample, each with four cartridge heaters. In the first experiment on Waspaloy the chromel-alumel control thermocouples were inserted in the heater blocks. In the second experiment on Ti alloy the heater control thermocouples were mounted in the vanadium. The furnace walls were made of the insulating mineral Cristobalite. A 5 cm thick sample of low density Cristobalite attenuates the neutron beam by only 23% and thus is a very suitable material for construction of an air furnace. The Cristobalite was machined into 10 half-ring-shaped pieces which were held together by two Al rods running through the rings and secured to Al plates at the top and bottom of the furnace. The furnace was constructed in two halves to facilitate specimen changes.

The power requirements for the furnace were low, and varied from 9 W at 500^0K to 129 W at 873^0K.

3.3   Temperature Control

The temperature control system made use of an IBM PC-XT interfaced to an HP3478A digital multimeter and an analog output board which provides a zero to ten volt control signal to a phase angle silicon control rectifier power module. The power from the module was proportioned to the two heater blocks by adjusting two variacs to equalize the temperature with a stability of about $\pm$ 0.1^{0}K. A third thermocouple was mounted on the sample and read by a minicomputer (supplied by Pratt & Whitney) every time the spectrometer finished a neutron count.

In the experiments, a thermal gradient did exist along the sample and in general the third thermocouple always read lower than the control thermocouples. The origin of the effect was the convection current set up through the access holes for the pull-rods in the top and bottom of the furnace. The possibility therefore exists that the bulk temperature may be higher than the surface temperature since the heat loss is at the surface. After the first experiments were analyzed it was decided to repeat the measurements on Waspaloy in a neutron-diffraction vacuum furnace to avoid thermal gradients. This second series of measurements was needed to achieve higher statistical accuracy on the material calibration constants by measuring the strain and temperature at more temperatures.

3.4   Neutron Scattering Measurements

The experiments were carried out on the L3 spectrometer at Chalk River in a medium resolution configuration with the (331) planes of a silicon monochromator providing neutrons of wavelength 1.480 Å. The relatively short wavelength of the neutron beam permitted access to the high index planes whose intensities are most sensitive to temperature. The collimation in both the incident and scattered beams

provided by collimator blades was 0.43^0 for the experiment on Waspaloy. The diffraction peaks were obtained by moving the single counter in 0.1^0 steps over the required angular range. The full width at half maximum of the diffraction peaks was lowest for the (220) and (113) peaks and rises for the lowest index peaks and for the highest index peaks with this arrangement.

The sample was positioned at the center of the spectrometer to within ± 0.5 mm with the aid of a laser beam aligned with the incident and scattered beams. Neutron absorbing masks were placed in the incident and scattered beams so that the illuminated height of the sample was 2.5 cm.

With this set-up the height of the sample in the beam stays constant as a function of temperature and the area increases slightly due to the coefficient of thermal expansion. The peak intensity data were corrected for these small geometric effects.

The time taken to acquire the data for each diffraction peak in Waspaloy varied from 1 hour for the (111) and (002) to 3 hours for the (220), (113) and (222) peaks.

The structure factor for the Titanium alloy is reduced by more than a factor of ten below Waspaloy because of the relative values of the nuclear scattering cross sections. The experiment would have therefore taken more than ten times longer with the set-up used for Waspaloy. A multidetector counter set-up was therefore used to improve the data acquisition rate. For this experiment, the incident beam collimation was defined as usual by the sample and the width of the beam close to the monochromator, while the scattered beam collimation was defined by the sample and the width of each 6 mm counter in the multidetector. The collimations were respectively 0.30 and 0.36^0. The time taken to acquire the diffraction peaks was of order 2 1/2 hours again, thus compensating for the low nuclear scattering properties of Ti. It follows that the use of a multidetector would have reduced the data acquisition times for Waspaloy by a factor of about ten. For the experiment on the Titanium alloy the wavelength of the neutron beam was 1.485Å.

Repeated measurements on Waspaloy were made with the E3 spectrometer at Chalk River with the (331) planes of a silicon monochromator to provide neutrons of wavelength 1.4692Å. The collimations before and after the sample were 0.28 and 0.30^0.

3.5   Samples

The materials studied, Waspaloy (AISI 685) with composition $Ni_{58.0} Cr_{19.5} Co_{13.5} Mo_{4.3} Al_{1.3}$ and the Titanium alloy AMS 4928 were provided by Pratt & Whitney Canada. Waspaloy is basically a face-centered cubic matrix with a simple cubic strengthening phase of the type $Ni_3 Al$. The diffraction lines studied here were from the matrix, but one of the lines of the strengthening phase was also followed in the second set of measurements. Waspaloy is a material commonly used for high temperature turbine blade and turbine disc applications. The titanium

alloy is an ($\alpha + \beta$) two-phase alloy of hexagonal close packed α-Ti, with cubic β-Ti Al used for relatively low temperature application since it ages and decomposes at high temperatures.

4.0   RESULTS

1.   Waspaloy

Measurements of the (111), (002), (220), (113) and (222) diffraction peaks were made at applied stresses near 20, 80 and 150 MPa and temperatures of 309, 392, 506, 607, 714 and 822^0K. The temperatures are the averages of the control temperature and the temperature on a thermocouple attached to the center of the sample. Typical raw data of counts versus angle at temperatures of 309, 607 and 822^0K are shown in Figure 4. The shift to a smaller diffraction angle, corresponding to a lattice expansion, and the intensity loss are evident.

The maximum count in this experiment was 11,000 counts on a background of 2500 in 2 1/2 hours. The lattice spacing as a function of stress and temperature for the (113) reflection is shown in Figure 5 and this gives an overview of the behavior of the material. The straight lines through the points, are least squares fitted to a linear stress versus strain law and the errors are the size of the points. Taking as reference points the spacing at 309^0K, the thermal strain is tabulated in Table 1 and the average strain is plotted in Figure 6. The error of the average is the standard error from the five measurements. The typical make-up of the average is shown in the inset for 506^0K; the most precise results come from the (200), (220) and (113) reflections which have the smallest line width. The solid curve is the macroscopic curve of thermal strain versus temperature for Waspaloy[14]. By comparing the neutron strain measurements with the macroscopic strain the effective temperature can be deduced and this is shown as T_{eff} in Table 2. A thermal gradient existed on the sample since there was a difference between the control thermocouples and the central thermocouple. The upper and lower limits on the temperature are given by these thermocouples and the values of T_{eff} fall between these limits and are quite closely equal to the average of the limits. The data from the second experiment are well represented by a second order polynomial in T:

$$\varepsilon_{th} = -(28.7 \pm 0.1) + (0.0834 \pm 0.0006)T - (5.04 \pm 0.03) \times 10^{-5}\, T^2.$$

The strain response to the applied stress is shown in Figure 7 and tabulated in Table 3 where the reference lattice spacing for calculating strain was the value obtained by extrapolating to zero stress. The solid curves in Figure 7 represent the bulk strain perpendicular to the direction of the applied stress calculated with polycrystalline Young's modulus[15] 213 GPa and Poisson's ratio $\gamma = 0.3$ (taking the value for Inconel) at 309^0K, and 180 GPa and 0.3 at 850^0K. The filled circles and squares represent the strain gage response to the applied stress. The strain gages became detached from the sample surface above 392^0K. The open symbols

represent the strain measured with the designated diffraction lines with errors derived from the uncertainty in the appropriate lattice spacing. Because of the variation of instrumental line shape with angle, the most precise measurements of strain were made with the (002), (220), (113) and (222) lines. In general, the "crystal" strains were larger than the calculated strains, which were in turn larger than the strain-gage values. However, to within the experimental errors, the "crystal" strains agreed with the calculation. The strain response was less for the (222) than for the (002) reflection as predicted by Equation 8 and the (113) and (220) reflections come between these limits. The bulk elastic constant calculated with the Kröner model, and the same single crystal elastic constants[16] as for calculating the diffraction elastic constants with Equation 8, is $\gamma/E = 1.33 \times 10^{-3}$ $(GPa)^{-1}$ compared with the bulk value of $\gamma/E = 1.40 \times 10^{-3}$ $(GPa)^{-1}$.

The intensity of each diffraction line and the relative intensity I'_T/I'_{REF} Equation 17, which takes out texture effects and corrects for slight position shifts of the diffraction line are recorded in Tables 4 and 5 for the two experiments on Waspaloy. The results are plotted versus reduced temperature $(T-T_{REF})/T_{REF}$ in Figure 8a with the quantity $2\sin^2\theta_{REF}/\lambda^2$ divided into the reduced intensity for each reflection, following Equation 20, to bring all the results onto a single master curve. There is good agreement among the different reflections to within the experimental errors which are shown in Figure 8a. The data for all (hkl) may be fit by a straight line over the entire temperature range. Constraining the intercept to be zero we obtain a slope of -0.4894 ± 0.0053. A constant that characterizes the temperature dependence of the peak intensity for Waspaloy must have a relatively low uncertainty as found for the slope of the line. However, it is obvious that the data exhibit some curvature, over the temperature range of interest.

Fitting with a second order polynomial, we obtain the relation

$$R' = 0.435(30)t - 0.036(12)\, t^2$$

where R' is $\ln (I'_T/I'_{REF})/(2\sin^2\theta_{REF}/\lambda^2)$ and t is $(T-T_{REF})/T_{REF}$. The agreement of this function with the data is better and the linear coefficient agrees with the Debye-Waller factor of Ni near room temperature as measured by neutron scattering.[11] However, the uncertainties on the coefficients are too large for the polynomial to serve as a precise calibration curve for Waspaloy.

The data may also be presented as a plot of $(1 - I'_T/I'_{REF})/(h^2 + k^2 + l^2)$ vs. $(T - T_{REF})$ as suggested by Eq. 21 and shown in Fig. 8b. Over the entire temperature range the data are well represented by a straight line of slope $0.0537(7) \times 10^{-3}$. This slope has a sufficiently low uncertainty that it serves as a reasonable characterization constant for Waspaloy. Intensity data plotted in this way cannot readily be linked to a Debye-Waller factor, but this approach is best as a simple way to correlate peak intensity to temperature.

To determine a Debye-Waller factor from our measurements we note that in Equation 1 and 9 since the structure factor, multiplicity and the texture are identical for the (111) and (222) reflections we have

$$\ln I'_{111} - \ln I'_{222} = -\frac{2B}{\lambda^2} \left(\sin^2\theta_{111} - \sin^2\theta_{222} \right) \qquad (22)$$

Thus at each temperature knowing the intensities and angular positions of the two reflections we may derive the value of B. The value obtained is 0.42 ± 0.06 Å^2 for 309^0K in agreement with the values for Ni and the value obtained from the slope of the reduced intensity curve discussed in the previous paragraphs. This also provides a good test of the accuracy of the neutron diffraction spectrum obtained over a wide angular range. The variation of B as a function of temperature derived from the (111) and (222) reflection are plotted in Figure 9 and is seen to be linear in form as approximated in Equation 19.

As a general remark, the variation of intensity with temperature is seen to be more susceptible to statistical noise than was observed in the thermal strain figure. Thus an individual measurement of intensity is less likely to give an accurate measure of temperature than a single strain measurement.

4.2   Titanium AMS 4928

Measurements of the (0002), (1011), (1120) and (1013) peaks of the hexagonal a-phase of the alloy were made at applied stresses of 25, 65 and 115 MPa and temperatures of 310, 394, 488, 584, 678, 725 and 441^0K. The temperatures are the averages of the temperature-control thermocouple, mounted on the vanadium pull-rod below the heater, and a thermocouple attached to the center of the sample. Figure 10 shows data for the (1011) reflection at 310^0K in the as- received condition and after the temperature measurements were completed.   In the as-received condition a secondary peak, the (110) peak of the cubic β-Ti Al[17] strengthening phase appears at $2\theta = 37.6^0$.   After raising the temperature to 725^0K this cubic phase peak has disappeared, signifying that a micro structural change has occurred with a transformation from the β-phase to the hexagonal α-phase. Figure 11 shows the data for the (0002) peak and the b-Ti Al (110) peak at 488, 584, 678 and 725^0K and indicates immediately that the change in micro structure has begun at 678 and is complete at 725^0K. Since there has been a change in the volume fraction of a-phase it is clear that the intensity will not give a reliable measure of temperature at 678^0K and above. To the extent that the minor atomic constituents are redistributed into the a-phase, the lattice spacing may change due to alloying, so that the atomic spacing may also be unreliable as a measure of temperature. Figure 11 shows a capability of the technique, not addressed in this report, of recognizing micro structural changes by diffraction in situ. The (1120) and (0002) diffraction peaks do

34

not have any side peaks associated with minority phases, whereas secondary peaks are quite close to the (1011) and (1013) peaks making the intensity measurement uncertain. In spite of these considerations all the data from the four peaks are presented in this report.

The temperature and applied stress dependence of the lattice spacing corresponding to the (1120) reflection is shown in Figure 12 which clearly shows the relative scale of thermal expansion and the strain response to the applied stress. The stress-free lattice spacing is obtained from the intercept and the elastic response from the slope of the straight line through the data.

The variation of the thermal strain for the low reflections, relative to the reference spacing at 310^0K is plotted in Figure 13. There are two coefficients of linear expansion for Ti, corresponding to expansion along the hexagonal axis and perpendicular to it, which differ by about 10%. The differences between the (0002) expansion and the (1120) expansion which we have observed are generally consistent with the differences in the macroscopic thermal expansion coefficients. There is much more spread in the values among the low reflections than for Waspaloy. This scatter may also indicate the relaxation of grain-to-grain strain as the temperature is raised as well as the intrinsic thermal expansion. (The grain-to-grain strain would be generated by the forging process in making the alloy billet from which the sample was taken). The horizontal error bars span the temperature range from the value recorded on the vanadium rod to the value recorded at the midpoint of the sample. The solid line represents the macroscopic thermal strain derived from conventional thermal expansion measurements for Ti[17]. The temperatures deduced from the spacing are given in Table 6 together with thermocouple measurements. The temperature derived from the neutron measurements has an uncertainty of $\pm 5^0$K from the spread in measured strain and is offset on average from the thermocouple temperature by $+5^0$K. It is systematically higher than the average of the two thermocouples but within the range of the two sets. With a temperature gradient, caused by convective cooling, the surface would be expected to be lower than the bulk. The major discrepancies occur at 688^0K and 725^0K, where, as we have noted earlier, micro structural changes have occurred. The variation of the load-induced strain as a function of applied stress for the low reflections is shown in Figure 14 at 310^0K and 584^0K. The lines in the figure represent the values of $-\gamma/E$ calculated from the bulk Young's modulus and Poisson's Ratio at the appropriate temperatures for Contimet AlV64[19]. The material softens elastically as the temperature is raised and this is seen in the data.

The temperature dependence of the natural logarithm of the intensity at temperature, T, relative to 310 K^0 is plotted in Figure 15 for the (0002) and (1120) peaks. The intensities were derived by two methods, either from the area under a Gaussian with variable width, intensity and position, fitted to the data or from the numerically integrated intensity in the peak above background. The methods agree to within the experimental errors. The results are given in tabular form in Table 7. The lines through the data refer to the expected variation of intensity with

35

temperature based on the value of the Debye temperature of 373^0K which corresponds (Equation 15) to a single Debye-Waller factor of 0.553 $\AA^2$. The same value of the Debye-Waller factor was derived from the parameters presented by Sears and Shelley[10]. The calculation gives a good representation of the behavior of the (1120) peak but lies below the experimental (0002) results. The experimental results may indicate that in fact different Debye-Waller factors pertain to the two directions. The data for all the reflections for Ti is plotted in Figure 16 where the effects are put on a single master curve by dividing out $2\sin^2\theta_{REF}/\lambda^2$ following Equation 20 and plotting versus the relative change in temperature. The curve is for a Debye-Waller factor of B = 0.55 $\AA^2$. The (1120) data agrees quite well with the expected variation. However, for the other reflections the agreement is quite poor, certainly not sufficiently precise to give a good estimate of temperature from the intensity.

5.0 PROBLEM AREAS

The principal problem area is the time taken to obtain the data. A time of 2.5 hours is too long to be valuable for measuring temperature excursion which may be as large as several hundred degrees in a few seconds when maximum thrust is developed. On the other hand the temperature inside the turbine disc at cruising speeds is still not known with any certainty and information in these conditions would be valuable. The use of a multidetector device would cut the time to obtain the information to about 0.5 hours: a high flux reactor running at a flux ten times greater than NRU, i.e. 3×10^5 n cm^{-2} sec^{-1}, would provide the information in about three minutes. It will be interesting to make measurements of the temperature by diffraction on a spallation source. In this case all reflections are collected in time-of-flight at a fixed counter position. The same information is obtained at different angles, although at different arrival times, and it would be possible to bin all the data and obtain high statistical accuracy in a short time. It is intended to carry out exploratory measurements at the LANSCE source at Los Alamos to test the accuracy and speed of the measurement.

6.0 CONCLUSIONS

In Waspaloy we have shown that neutron diffraction is suitable as a noninvasive probe of temperature. Reasonably precise calibration constants were obtained to relate thermal strain (as deduced from shifts in the diffraction peak position) and peak intensity to the temperature of a sample. Applied load can also be determined noninvasively at temperature. Reliable calibration constants were not obtained for the titanium alloy due to an irreversible change in the micro structure during the thermal and loading cycle. However, the trends in the data indicate that calibrations could be made for this material as well.

7.0 ACKNOWLEDGMENTS

8.0   REFERENCES

1. P.H. Fowler and A.D. Taylor, Rutherford Appleton Laboratory Report RAL-87-56, 1987.

2. P.H. Fowler in Proceedings of the ICANS-VIII Conference July 1985 Rutherford Appleton Laboratory Report RAL-85-110, 1985.

3. J. Mayers, G. Baciocco and A.C. Hannon, Nucl. Instrum. Meth. A275 453, 1989.

4. R. Moreh, Proceedings of the International Workshop on the Applications of Intense Capture Gamma Ray Sources. Grenoble, France, 1978. Nucl. Instrum. Meth. 166, 45, 1979.

5. Patent assigned to Tokyo Shibaura Electric Company.

6. G.E. Bacon, "Neutron Diffraction" (Oxford: Clarendon Press) 1962.

7. I.C. Noyan and J.B. Cohen "Residual Stress" (New York: Springer Verlag), 1987.

8. H. Dollë J., Appl. Cryst., 12, 489, 1979.

9. "International Tables for X-Ray Crystallography" (The International Union of Crystallography: The Kynoch Press), 1959, Vol. II, p. 241.

10. V.F. Sears and S.A. Shelley (in press).

11. M.J. Cooper and K. Taylor, Acta. Cryst., A25, 714, 1969.

12. O. Inkinen and P. Suortti, Ann. Acad. Scient. Fenn., A6, 147, 1964.

13. B.T.M. Willis and A.W. Pryor, "Thermal Vibrations in Crystallography" (Cambridge: The University Press), 1975.

14. D. Leggett, Private Communication, 1989.

15. D. Leggett, Private Communication, 1989; Handbook of Materials Science, Chemical Rubber Company Inc., Cleveland, Ohio, Ed. CT. Lynch Vol.. II.

16. J.T. Lenkkeri, J. Phys. F. Metal Phys. 11, 1991, 1981.

17. Data for b-TiAl.

18. D. Leggett, Private Communication, 1989; Y.S. Touloukian, R.K. Kirby, R.E. Taylor and P.D. Desai, "Thermophysical Properties of Matter", Plenum Press: New York, 1975.

19. P. Schuler, DEW Technische Berichte, 7, 5, 1967.

20. E.S. Fisher and C.J. Renken, Phys. Rev. 135 A, 482, 1964.

TABLE 1

THERMAL STRAIN AS A FUNCTION OF TEMPERATURE IN WASPALOY

T_{av} ^0K	ε_{111} (10^{-4})	ε_{002} (10^{-4})	ε_{220} (10^{-4})	ε_{113} (10^{-4})	ε_{222} (10^{-4})	$<\varepsilon>$ (10^{-4})	ε_{112} (10^{-4})
	± 1.9	± 1.2	± 0.6	± 0.6	± 1.0	0	
				Experiment No.1			
309	0	0	0	0	0	0	
392	9.7	10.0	9.3	9.4	9.3	9.4±0.4	
506	25.0	23.9	23.6	24.0	23.6	23.8±0.4	
608	40.9	40.9	40.0	39.9	40.4	40.1±0.4	
714	53.9	56.1	54.6	54.6	55.1	54.8±0.3	
822	72.9	74.7	72,5	72.9		72.9±0.4	
	±0.7	±0.4	±0.4	±0.4	±0.4		±2.0
				Experiment No.2			
310	0	0	0	0	0		
312	0.7	0.2	0	-0.3	0.6	0.2±0.4	
414	11.7	11.2	11.4	10.2	10.3	11.0±0.7	11.7
450	17.7	17.5	17.4	17.2	17.1	17.4±0.2	18.0
500	24.0	23.3	23.2	23.6	23.9	23.6±0.4	22.5
525	27.0	26.9	27.2	26.9	27.3	27.2±0.4	27.6
525	28.2	26.9					
525	27.4						
550	30.7	30.4	30.4	30.1	30.1	30.3±0.3	29.0
600	38.4	37.6	37.3	37.1	38.0	37.9±0.4	37.9
600	38.3	38.1	38.1	37.9			38.2
650	45.7	44.9	44.6	44.0	45.1	45.1±0.5	41.6
650	45.7	45.3	45.3	45.4			45.5
700		52.6	52.6	52.1	52.4	52.4±0.2	48.9
800	68.2	67.3	68.1	67.7	68.1	67.9±0.3	66.0
800	68.0	68.1					67.0
900	86.4	85.8	85.7	85.2	85.4	85.7±0.5	82.1

TABLE 2

EFFECTIVE TEMPERATURES IN WASPALOY

Nominal Temperature (^{0}K)	Temperature deduced From Strain (^{0}K)
392±6	384±4
506±14	492±5
608±22	608±4
714±26	705±5
822±28	820±5
414±5	396±4
450±5	445±4
500±5	490±4
525±5	516±4
550±5	539±4
600±5	590±4
650±5	640±5
700±5	689±5
800±5	793±5
900±5	902±5

TABLE 3

STRAIN RESPONSE TO AN APPLIED STRESS IN WASPALOY

Temperature (^{0}K)	Applied Stress (MPa)	ε_{002} (10^{-4})	ε_{220} (10^{-4})	ε_{113} (10^{-4})	ε_{222} (10^{-4})
	Uncertainty	±1.2	±0.6	±0.7	±1.0
	20.1	-0.4	-0.3	-0.3	-0.2
309	83.2	-1.8	-1.4	-1.8	-1.2
	149.8	-3.1		-2.8	-2.5
	21.4	-0.4	-0.4	-0.4	-0.2
392	84.6	-2.2	-1.8	-1.8	-1.2
	150.1	-3.6	-2.9	-2.9	-1.8
	25.0	-0.6	-0.4	-0.4	
506	88.4	-2.1	-1.6	-2.2	
	153.7	-3.6	-2.9	-3.0	
	22.8	-0.9	-0.3	-0.5	
822	88.5	-3.2	-2.0	-2.1	
	152.8	-5.8	-3.0	-3.3	

TABLE 4

TABULATION OF WASPALOY INTENSITY DATA
BRAGG PEAK INTENSITIES AND INTENSITY RATIOS FOR DIFFERENT (hkl)
AT SEVERAL TEMPERATURES - FIRST EXPERIMENT

T (°K)	$\dfrac{I-I_{REF}}{I_{REF}}$	(111) I'_T	(111) R'^a	(002) I'_T	(002) R'^a	(220) I'_T	(220) R'^a	(113) I'_T	(113) R'^a	(222) I'_T	(222) R'^a
			±0.06		±0.05		±0.04		±0.04		±0.04
309	0	1463±8	0	809±2	0	1150±2	0	1566±9	0	2232±8	0
392	0.27	1465±8	0.03	800±2	-0.13	1105±18	-0.13	1510±7	-0.08	2120±12	-0.11
506	0.64	1439±8	-0.10	779±7	-0.25	1058±3	-0.25	1433±18	-0.19	1989±12	-0.24
608	0.97	1419±8	-0.19	726±3	-0.33	1066±5	-0.40	1350±10	-0.32	1852±8	-0.38

a. R' in Table 4 stands for: $\ln\left(I'_T / I'_{REF}\right) / \dfrac{2\sin^2\theta_{REF}}{\lambda^2}$

TABLE 5

TABULATION OF WASPALOY INTENSITY DATA
BRAGG PEAK INTENSITIES AND INTENSITY RATIOS FOR DIFFERENT (hkl) AT SEVERAL TEMPERATURES- SECOND EXPERIMENT

T (°K)	$\dfrac{T-T_{REF}}{T_{REF}}$	(111) I'_T	(111) R'^{a}	(002) I'_T	(002) R'^{a}	(220) I'_T	(220) R'^{a}	(113) I'_T	(113) R'^{a}	(222) I'_T	(222) R'^{a}
		±2.0	±0.16	±1.1	±0.07	±1.2	±0.04	±1.2	±0.03	±1.1	±0.03
310	0	218.1	0	203.4	0	207.1	0	194.1	0	188.5	0
450	0.452	211.4	-0.27	195.7	-0.250	192.7	-0.234	176.9	-0.219		
500	0.613							172.1	-0.284	164.9	-0.288
525	0.693	210.5	-0.31	192.6 193.7	-0.353 -0.317	190.2	-0.276	169.2	-0.324	161.8	-0.330
600	0.935	207.2	-0.44	190.4	-0.428	182.7	-0.406	161.2	-0.438	152.4	-0.459
650	1.097	205.8	-0.50	187.1	-0.541	178.6	-0.480	153.0	-0.560	149.7	-0.498
800	1.581	198.8	-0.80	179.1	-0.824	163.1	-0.774	137.3	-0.816	130.4	-0.796
900	1.903	195.7	-0.94	176.3	-0.926	156.8	-0.902	127.8	-0.985	116.3	-1.043

a. R' in Table 5 stands for: $\ln\left(I'_T / I'_{REF}\right) / \dfrac{2\sin^2\theta_{REF}}{\lambda^2}$

TABLE 6

T_{av} ^0K	ε_{0002}	ε_{1011}	ε_{1120}	ε_{1013}	$<\varepsilon>$	T_{strain} [a,b]
	± 0.6	± 0.6	± 0.5	± 0.6		
310	0	0	0	0	0	310
394	8.3	8.4	6.6	7.8	7.8±0.8	398±9
441	9.6	14.0	9.8	12.9	11.6±2.2	440±22
488	18.2	18.9	17.1	17.4	17.9±0.8	508±7
584	26.9	27.7	28.2	29.0	27.6±1.0	610±10
678	37.9	39.7	36.8	38.6	38.3±1.2	715±10
725	41.2	42.7	41.2	43.5	42.2±1.1	754±10

a. The titanium alloy data provided by Pratt & Whitney Canada Inc. was used to calculate the temperature from the strain. We noted however, that there was a systematic difference, as much as 22^0K at 725^0K, between the data of Touloukian et al[18] and the calibration used. This would bring the strain temperature into much better agreement with the average temperature.

b. The errors in the temperature deduced from the strain were derived from the r.m.s. error in the strain measurement.

TABLE 7

TEMPERATURE DEPENDENCE OF Ti-ALLOY INTENSITY

AVERAGE TEMP. (^{0}K)	(0002) I'_T	(0002) R' [b]	$(10\bar{1}1)$ I'_T	$(10\bar{1}1)$ R' [b]	$(11\bar{2}0)$ I'_T	$(11\bar{2}0)$ R' [b]	$(10\bar{1}3)$ I'_T	$(10\bar{1}3)$ R' [b]
	±13 [a]	±0.06	±1.4	±0.13	±31	±0.07	±85	±0.13
310	2061	0	2091	0	3729	0	4506	
394	2049	-0.06	2092	0	3647	-0.10	4447	-0.05
488	2028	-0.18	2066	-0.12	3530	-0.23	4357	-0.12
584	2025	-0.19	2068	-0.11	3337	-0.48	4156	-0.28
584	1967	-0.51	2006	-0.41				
678	1963	-0.53	1986	-0.51	3226	-0.62	4015	-0.41
725	1977	-0.45			3158	-0.71	3979	-0.44

a. Errors derived from the rms deviation of intensities obtained by fitting a Gausson to the intensity distribution.

b. R' in Table 7 stands for: $\ln \left(I'_T / I'_{REF} \right) / \dfrac{2\sin^2\theta_{REF}}{\lambda^2}$
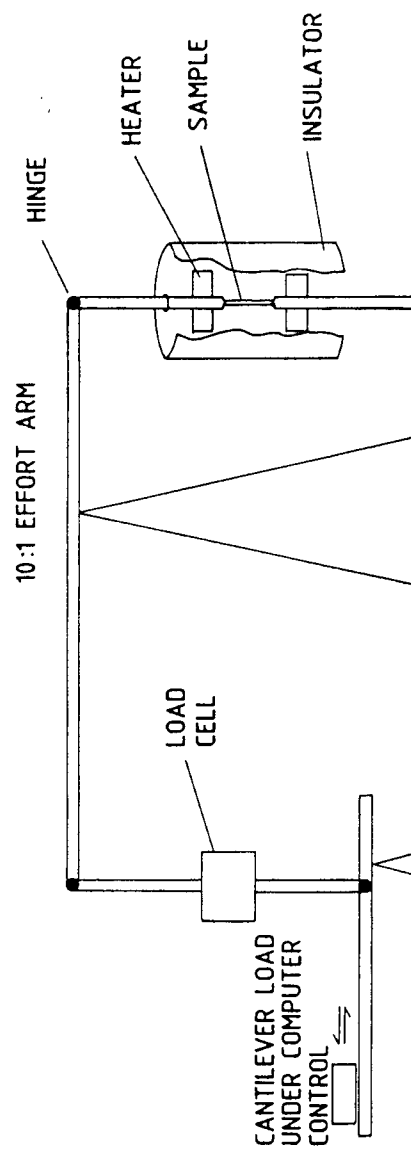
Figure 1 The arrangement of the loading rig. The sample is contained within the furnace on the short arm of the creep rupture machine and the load is applied with a computer controlled cantilever on the long arm. The load was measured with a load cell.
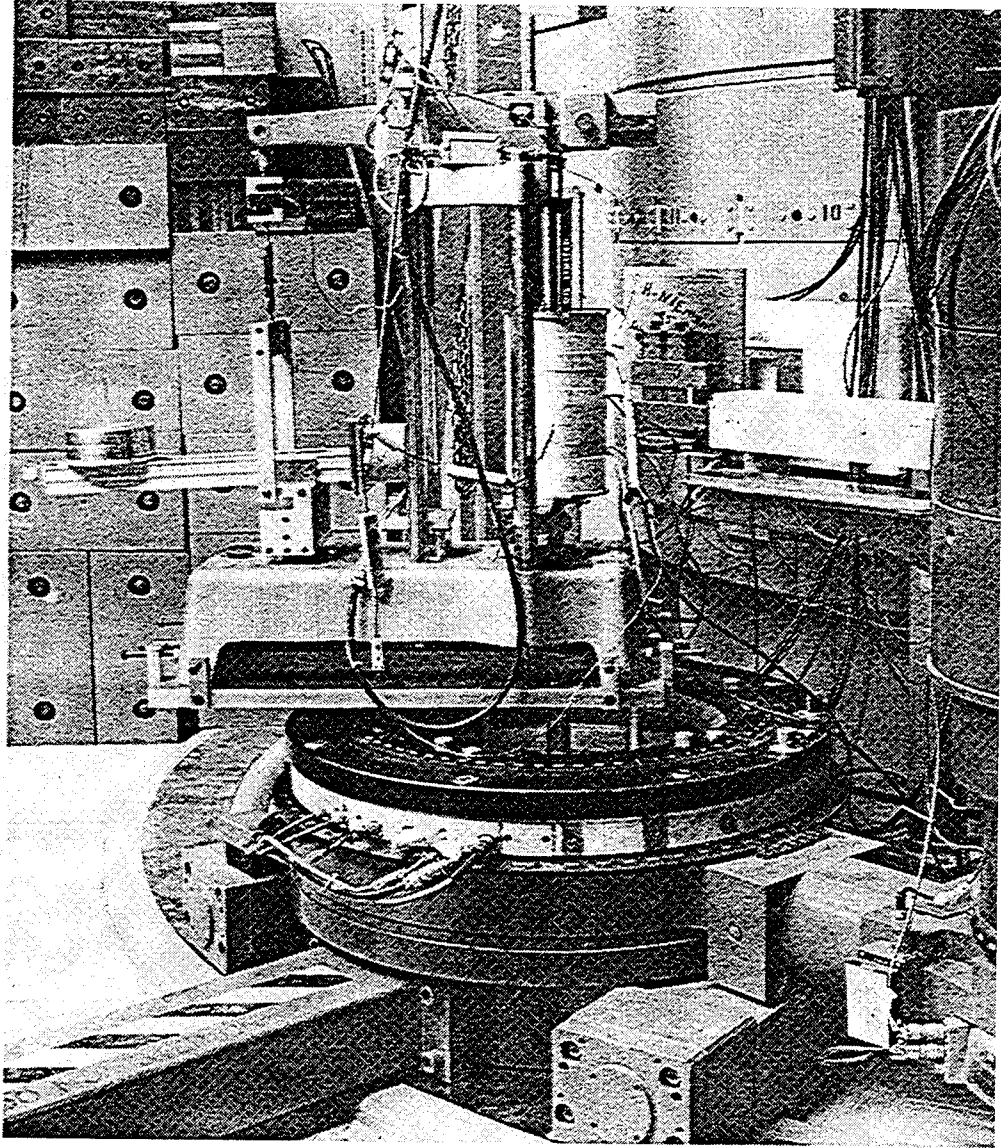
Figure 2   Photograph of the equipment installed at the L3 spectrometer at the NRU reactor, Chalk River, showing the modified creep rupture machine, and the linear drive on the cantilever.

LOAD

VANADIUM
PULL-ROD

THERMOCOUPLE NO. 1

STRAIN GAUGE

THERMOCOUPLE NO. 3

CARTRIDGE
HEATER

THERMOCOUPLE NO. 2
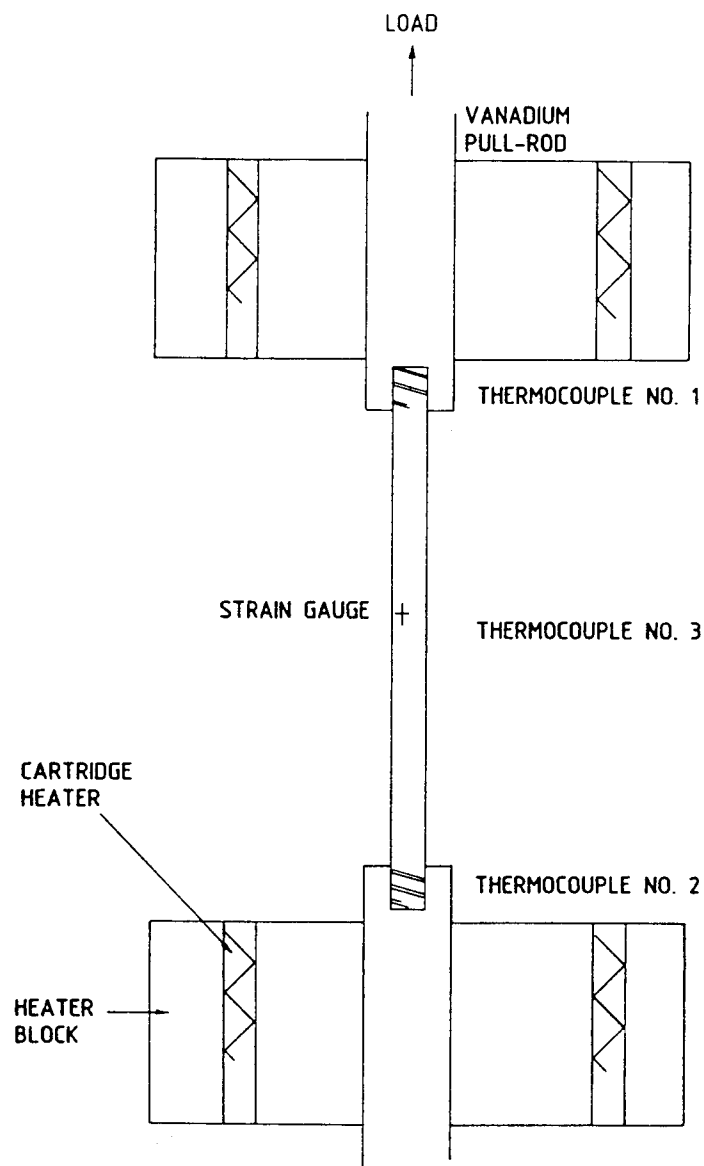
HEATER
BLOCK

Figure 3 Arrangement of the sample, vanadium pull-rods and cartridge heaters and heater block within the furnace.
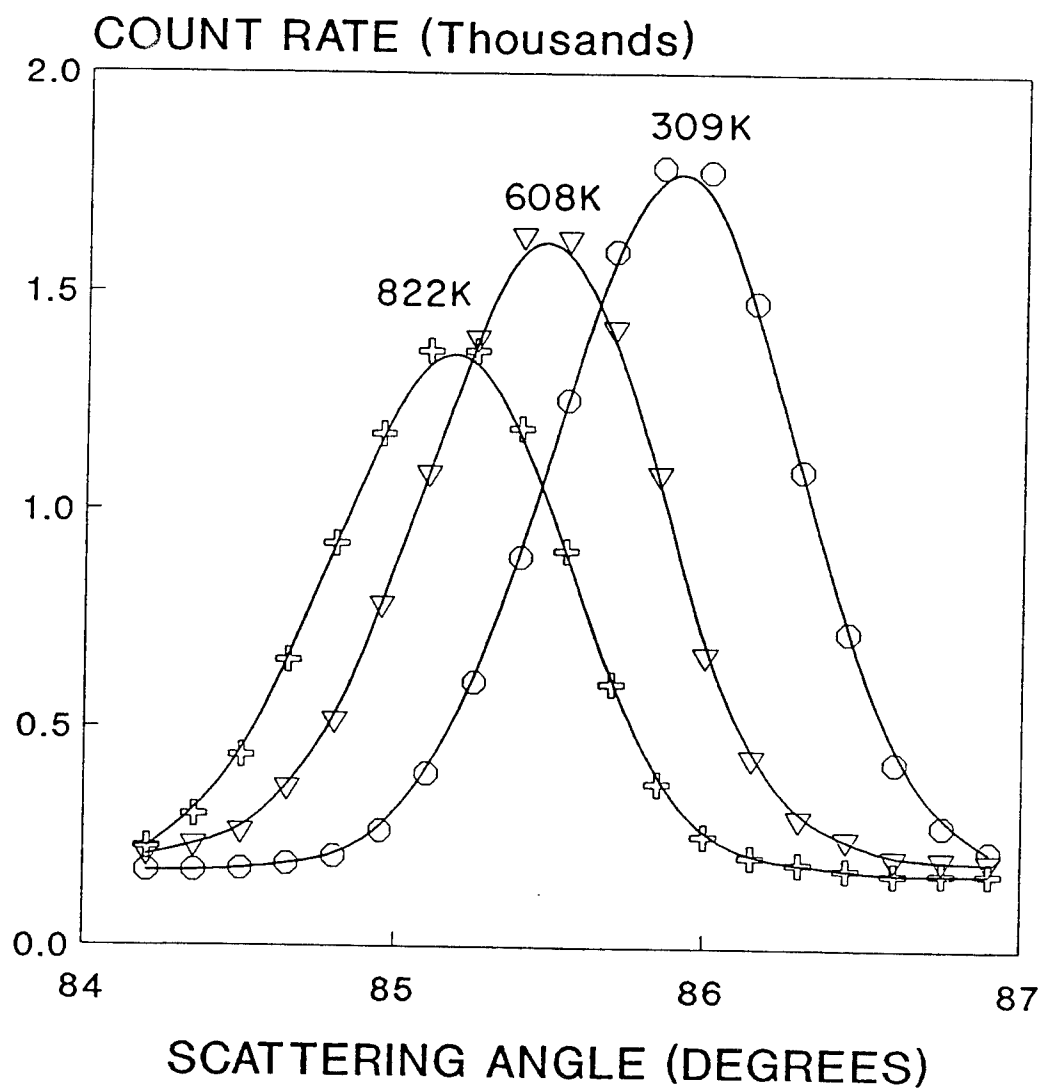
Figure 4 The temperature dependence of the (113) peak of Waspaloy showing the shift of the peak position and the diminution of the intensity.
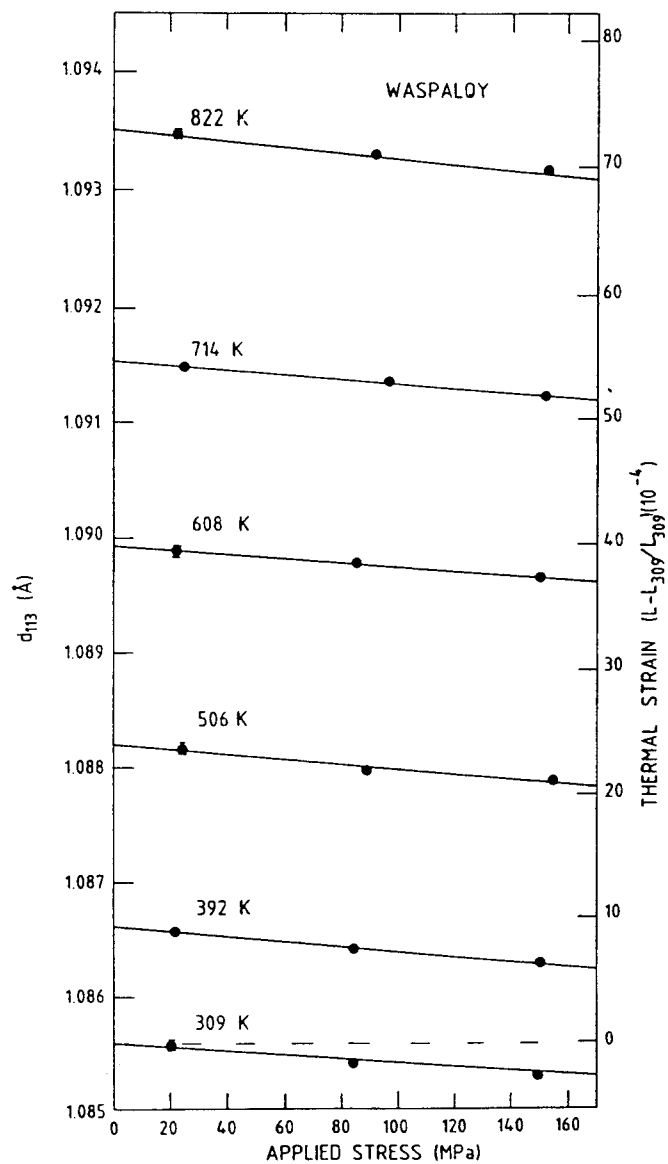
Figure 5 The lattice spacing corresponding to the (113) reflection of Waspaloy as a function of temperature and applied stress.
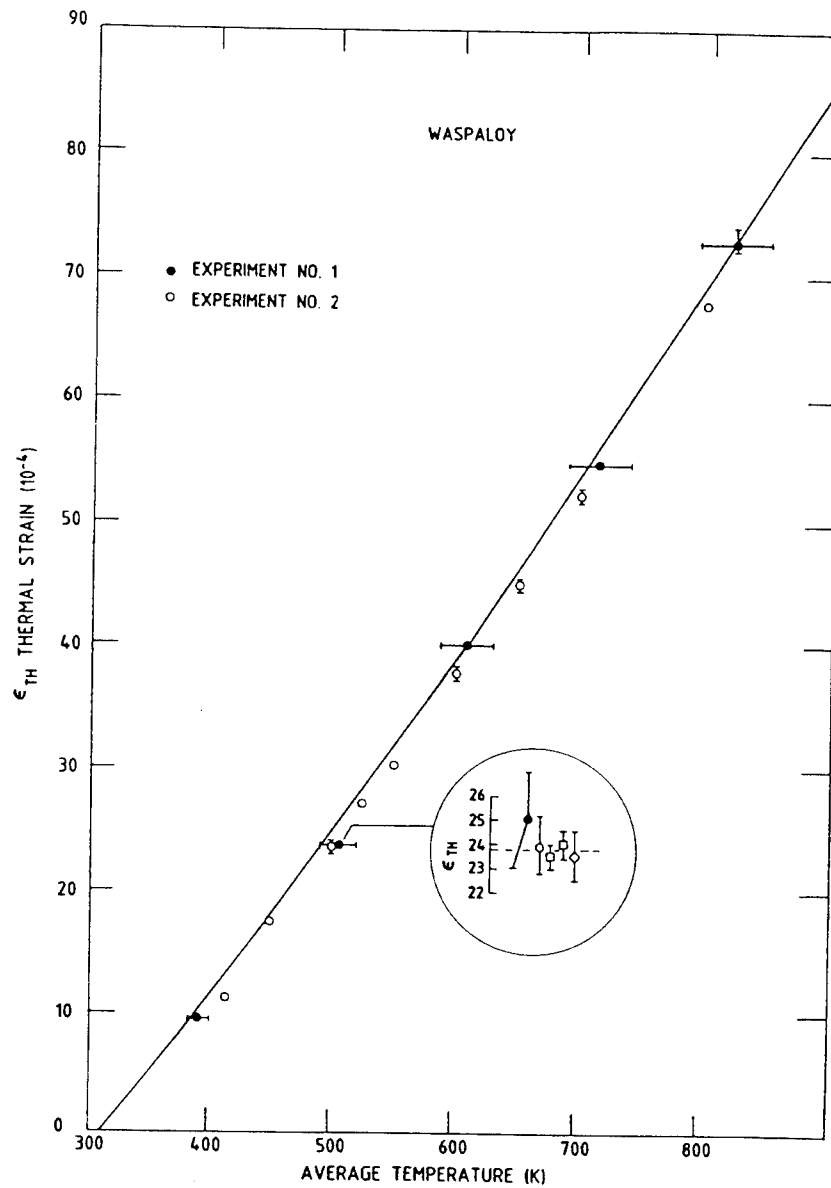
Figure 6 Thermal strain of Waspaloy with respect to a reference temperature of 309 K for the first (solid symbols) and second (open symbols) experiments. The curve is the macroscopic thermal expansion of Waspaloy. The inset shows the make-up of each measure of the thermal strain.
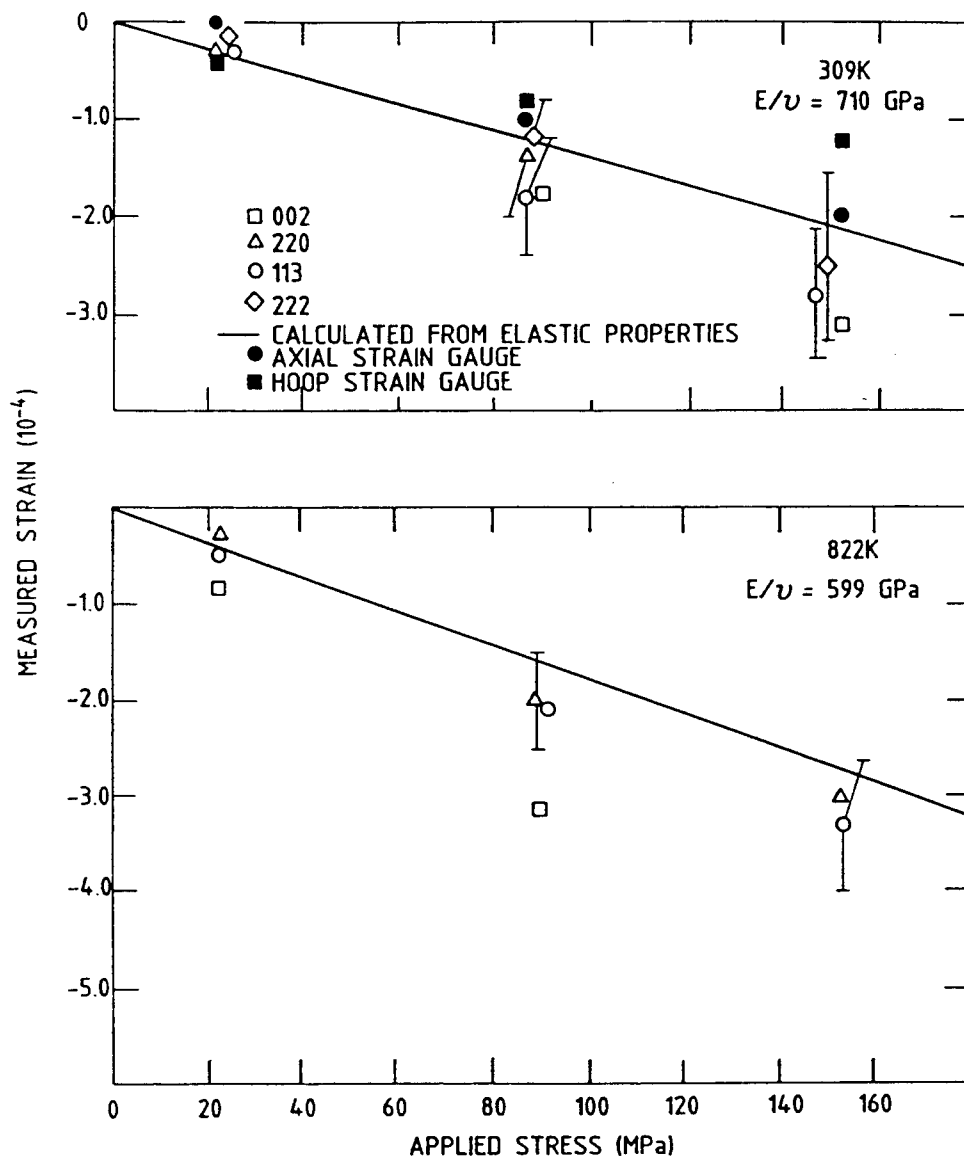
Figure 7 Strain response to applied stresses in Waspaloy at 309°K and 822°K. Open symbols represent the neutron measurements, closed symbols represent strain-gage measurements and the lines are calculated from the bulk Young's modulus and Poisson's ratio for Waspaloy at temperature.

51
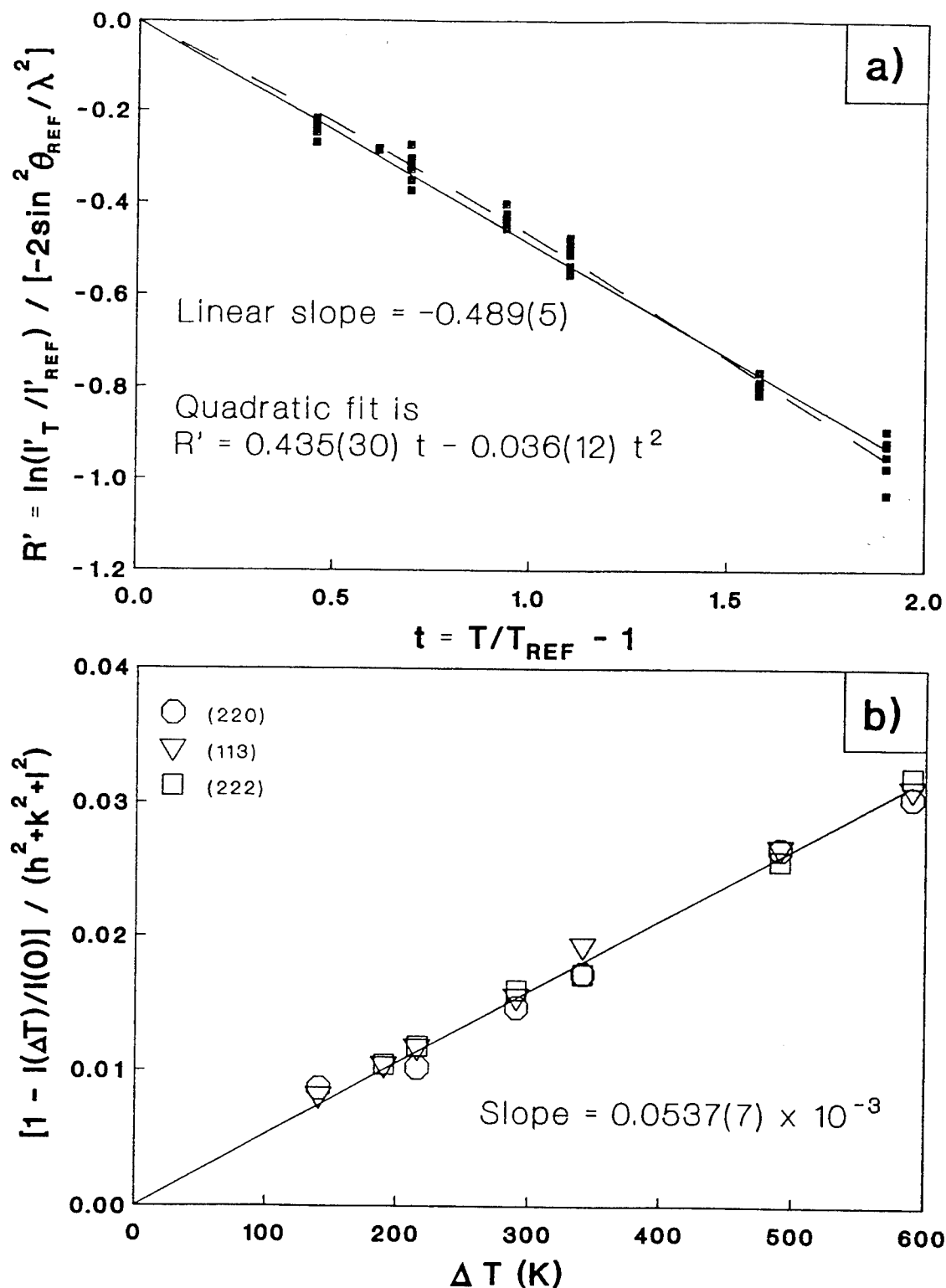
Figure 8   The temperature dependence of the ratio of intensity at temperature T to the reference temperature as a function of the temperature relative to the reference temperature for Waspaloy. (a) Data reduced via Eq. 20. The solid line is a linear fit to the data for all (hkl). The dashed line is a second order polynomial fit. (b) Data reduced via Eq. 21. The sold line is a linear fit to the data for all (hkl) shown.

$$B_{Ni} = 194.3 \frac{T}{\theta_D^2} \left\{ 1 + \frac{\theta_D^2}{36T^2} \right\}$$
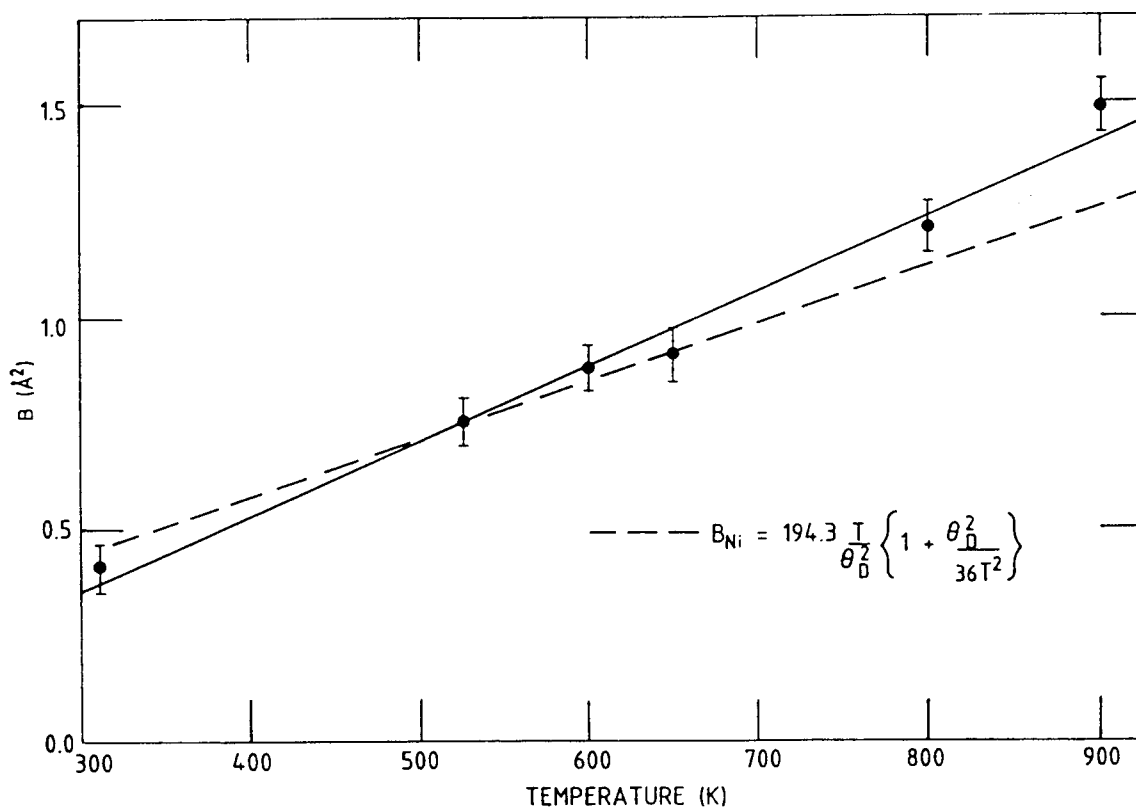
Figure 9   Variation of the Debye-Waller B, with temperature measured with the (111) and (222) reflections of Waspaloy. The solid curve through the data is the best least squares fit to a linear function. The dashed curve is the temperature dependence as given by Equation 15 with the value of B for Ni.

TITANIUM ALLOY
AGING NEAR THE (10-13) PEAK

COUNT RATE

SCATTERING ANGLE (DEGREES)

- ⊖ AS RECEIVED 310 K
- ▽ 700 K
- ⊕ RECOOLED TO 310 K
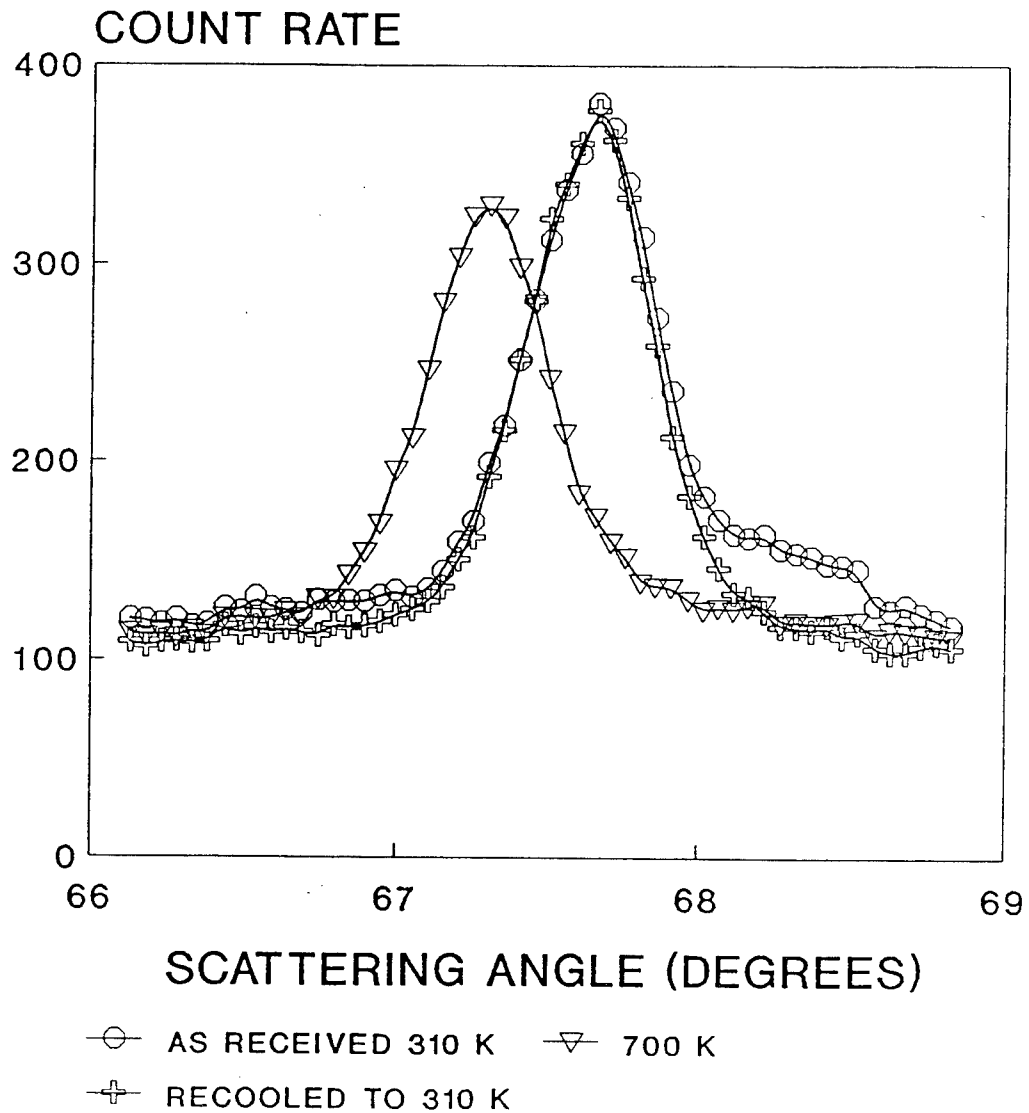
Figure 10 Profile of the (1011) reflection before and after raising the temperature to 725^0K showing the disappearance of the β-TiAl strengthening phase.

TITANIUM ALLOY
TEMPERATURE DEPENDENCE OF (0002) PEAK
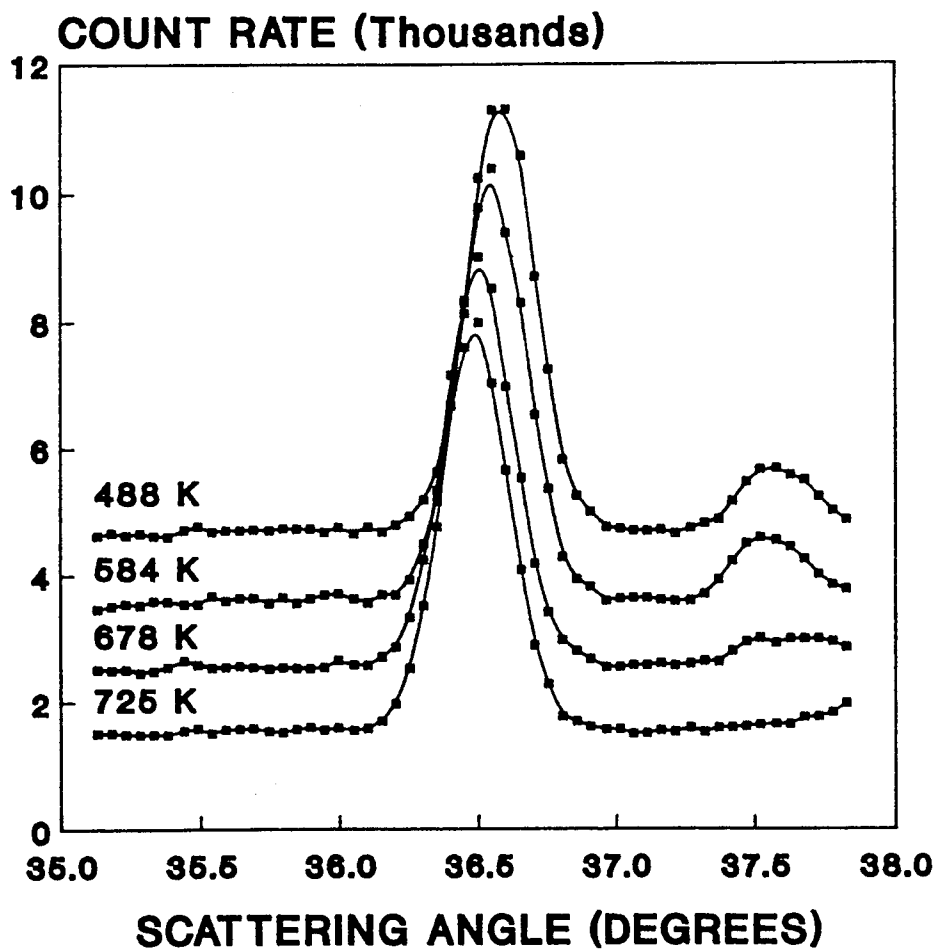
Figure 11 The temperature dependance of the (0002) peak, showing the shift and intensity fall and the abrupt disappearance of the (110) peak of the cubic phase β-TiAl at temperatures near 700^0K.
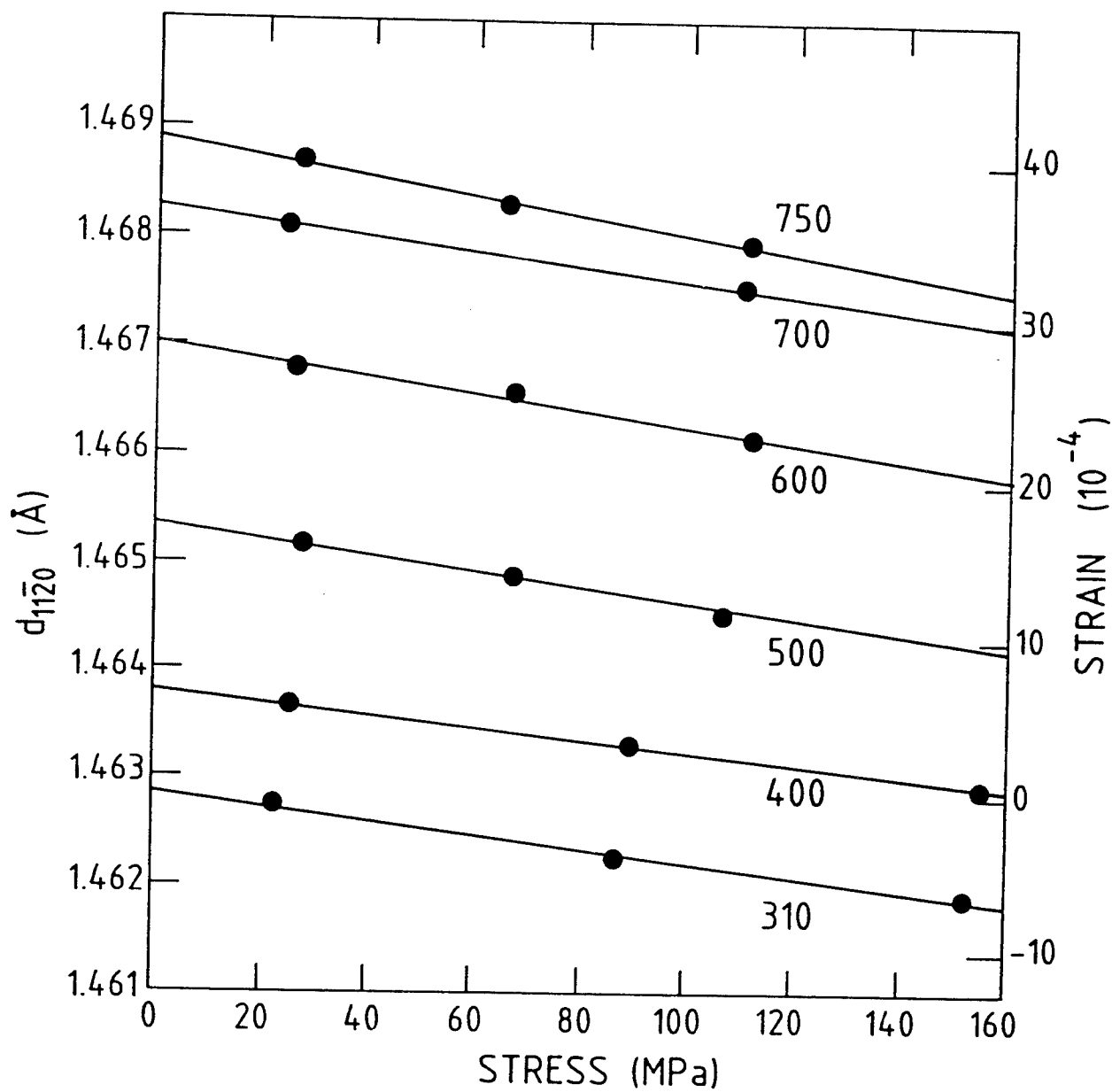
Figure 12 Variation of the lattice spacing corresponding to the (1120) reflections with temperature and applied stress.
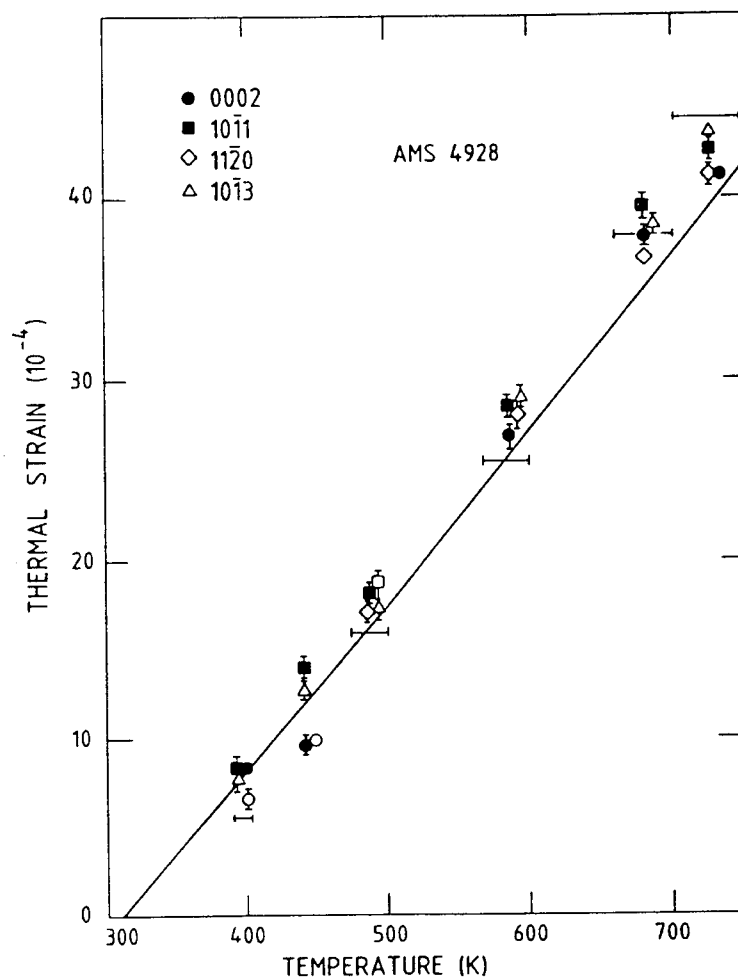
Figure 13 Thermal strains in the Ti alloy AMS 4928 with respect to a reference temperature of 310^0K for the four reflections studied. The curve is the macroscopic thermal expansion of Ti.
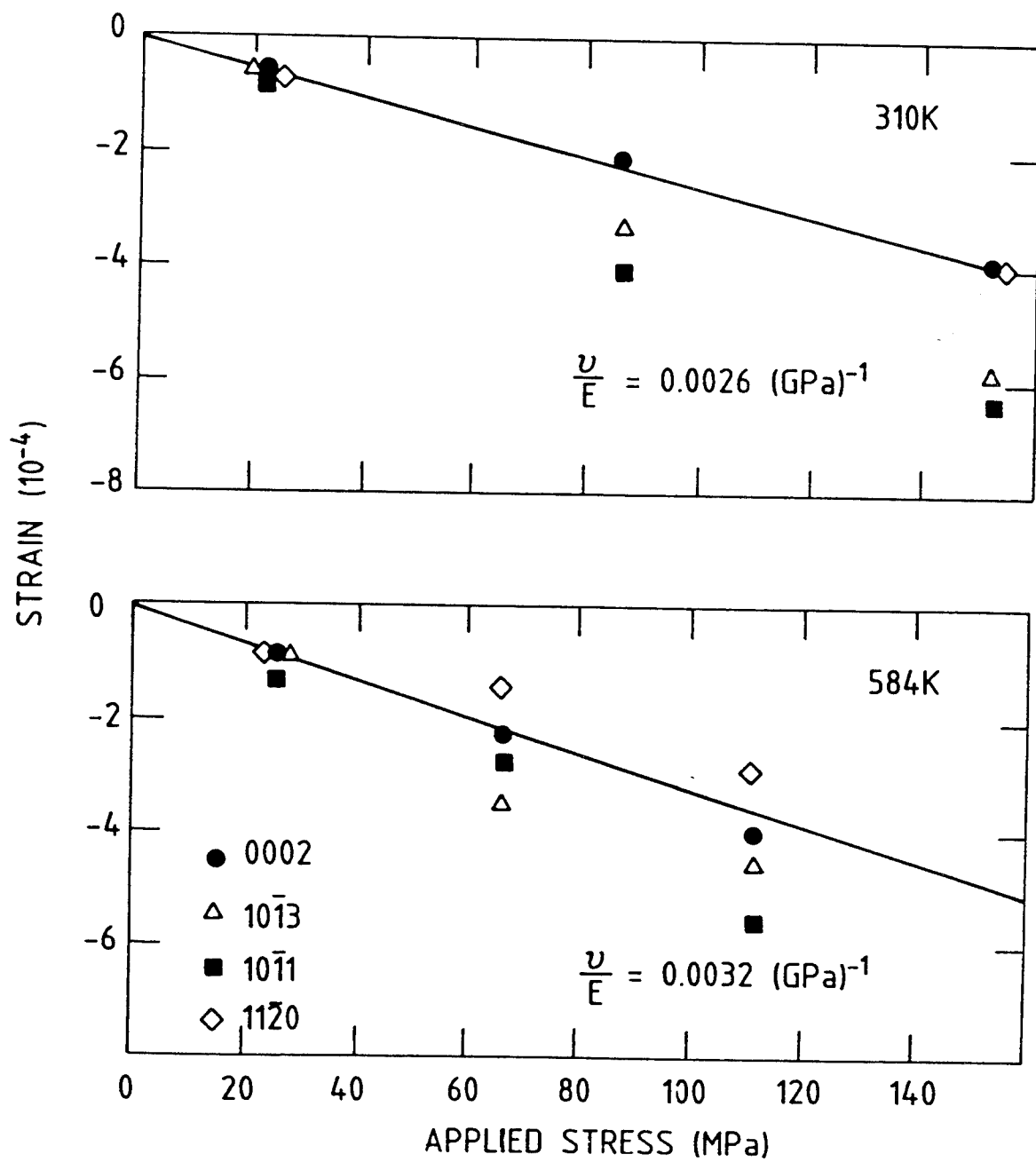
Figure 14 Strain response to applied stress in Ti-alloy AMS 4928.
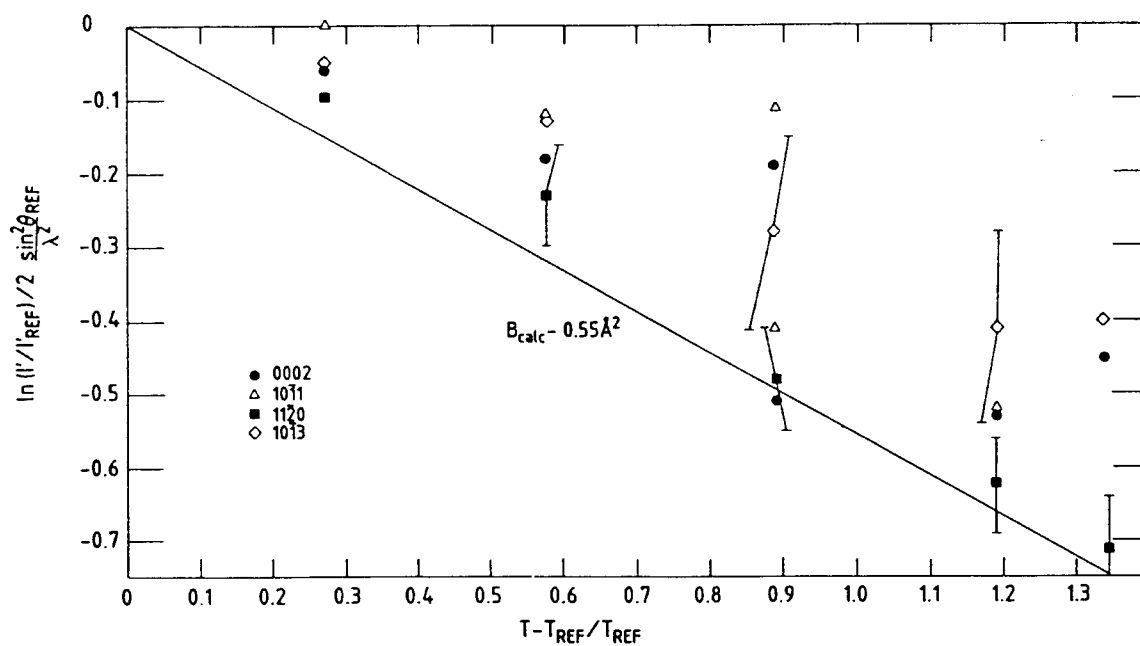
Figure 15 Temperature variation of the natural logarithm of the ratio of the intensity at temperature T to the reference temperature. The results for the four reflections were brought onto a common curve by dividing each by $2\sin^2\theta_{REF} / \lambda^2$. The curve is calculated from the value of B for Ti.

59

APPENDIX C

ANDI - 49 NEUTRON DIFFRACTION MEASUREMENT OF TEMPERATURE IN A ROTATING DISC OF WASPALOY

Atomic Energy Of Canada Limited

NEUTRON DIFFRACTION MEASUREMENT OF TEMPERATURE IN A ROTATING DISC OF WASPALOY

J.H. Root, T.M. Holden and D.C. Tennant

ABSTRACT

Measurements made on a disc of Waspaloy, spinning at 3000 rpm and heated electrically, verify the feasibility of neutron diffraction methods for the non-invasive measurement of temperature in a dynamic system.

Neutron and Solid State Physics Branch
AECL Research,
Chalk River,
Ontario, Canada
K0J 1J0

1.0   INTRODUCTION

Since neutrons penetrate through most engineering materials, neutron diffraction may serve as a non-invasive probe of the temperature at locations inside a running gas turbine engine, either through the observable changes in scattering angle or intensity of the diffraction peaks. High temperature components in gas turbine engines are often made of Waspaloy* which is a nickel-based alloy of nominal composition, by weight percent, $Ni_{0.58}Cr_{0.20}Ti_{0.03}Al_{0.01}Mo_{0.04}Co_{0.14}$. It has high tensile strength, ductility, resistance to crack propagation and low-cycle fatigue strength, even at high temperatures, and so is suitable for fabrication of gas turbine discs, integral disc/shaft units and discs with integral blades. The temperature dependencies of the mean scattering angles and integrated intensities of neutron diffraction peaks in a static specimen of Waspaloy have been characterized by calibration functions specific to this material.

Prior to attempting measurements within an actual engine, a number of preliminary tests have been completed on a rotating disc made of Waspaloy, and the results are presented in this report. These tests establish the accuracy of the two diffraction-based thermometry methods and the effect of the micro structure of the material on the precision of deduced temperatures. The tests also establish the feasibility of selecting a particular circumferential location in a rotating component and demonstrate the effects of the disc motion on measurements made with the finite velocity neutron probe.

2.0   EXPERIMENTAL

2.1   Sample

The sample was in the form of a disc of diameter 203 mm and thickness 16 mm. Two diametrically-opposed, through-thickness holes of diameter 25 mm were centered at radius 70 mm. The material of the disc was examined by metallography following the diffraction experiments. The grain size was evaluated at three radial positions along the line between the through thickness holes and the average value was 102 ± 3 μm.

Chromel-alumel thermocouples were affixed to the surface of the disc at locations indicated in Fig. 2.1, corresponding to the radial distances listed in table I. The disc was attached to a shaft to be turned at 3000 r.p.m by an electric motor. The thermocouple signals were extracted from the shaft by a slip ring, and collected by a Daytronics data acquisition system, on loan from Pratt & Whitney Canada, Inc.

A temperature gradient was introduced to the disc by placing a stationary, 1 kW electrical heating element around the perimeter of the disc. The heater temperature was controlled at a value of 772^0K. The shaft was cooled by circulating freon, so the temperature varied with radial position. A through-thickness variation of temperature

---

* Trademark of United Technology Corporation

was also expected since the spinning disc was cooled at the surface by the relatively moving air. The disc and heater were enclosed in a steel casing, with insulation made of silica-based fibers held against the casing with a thin-walled aluminum plate. A window was cut into the steel casing and through the insulation to reduce the amount of material the neutron beams would penetrate in reaching the Waspaloy disc.

The disc and motor assembly were mounted on a milling-machine bed, located on the floor close to the neutron diffractometer. Vertical positioning of the disc was achieved by a manual drive. There was an uncertainty of the order of a few millimeters in the vertical positioning of the disc with respect to the spatially fixed sampling volume. Positioning within the horizontal plane was achieved by stepping motors under computer control. There was no direct coupling of the milling machine to the diffractometer, so the orientation of the disc with respect to the direction of the incident neutron beam was fixed.

A cylindrical coordinate system defines positions in the disc most effectively, with R the radial distance from the disc axis and Θ the azimuthal angle from a reference direction. In the frame of reference of the neutron diffractometer, Θ was measured from the vertical direction, as shown in Fig. 2.2. The temperature measurements by neutron diffraction were made along the $\Theta = 90^0$ axis, at values of R=34 mm, 46 mm, 72 mm, 85 mm, 91 mm and 97 mm, at the mid thickness of the disc. Along this locus, even though the disc was spinning, the relative velocity of the diffracting plane normal in the direction of the scattering vector was zero. One measurement was made at R=81 mm and $\Theta = 8^0$, at which location there was a high relative velocity between the diffracting plane normal and the scattering vector. As a result, a Doppler shift in the angular position of the diffraction peak was expected and observed (see Section 3.3.1). With the disc spinning, a measurement at a given value of R is an average over all values of Θ. At R=72 mm, the diffracted neutrons were collected in a multichannel scalar (MCS), to characterize circumferential variations of the diffraction peak parameters. The channel numbers of the MCS were reset and incremented by an encoder fixed to the shaft, to divide the circumferential track into 60 sectors of width, $\Delta\Theta = 6^0$. The encoder was a magnetic sensor that detected the passage of slots machined into a steel disc attached to the main shaft. The output signals from the magnetic sensor were sharpened by a Schmidt trigger to increment the MCS channel number reliably. Lost incrementing pulses were maintained below a level of 1% over the duration of the experiment. Also, the percentage variation of the distance between slots on the encoder was within ±1% of the mean.

2.2 Neutron Diffraction

The neutron diffraction measurements were made with the L3 triple-axis spectrometer on the main floor of the NRU Reactor, at AECL Research, Chalk River Laboratories, Canada. Diffraction from the (331) planes of a single crystal silicon monochromator provided an incident neutron beam with a wavelength of 1.4435 Å.

have height and width dimensions of 9 mm. The diffracted beam was also shaped with a cadmium mask to have a width of 9 mm. Diffraction measurements were made only within the volume defined by the intersection of the incident and diffracted beams, denoted as the sampling volume. By adjustment of the sample position with respect to the spatially-fixed neutron beams, the sampling volume was centered at the mid thickness of the disc, and was always completely within the disc material except when a through thickness hole swept past.

A multiwire, ^{3}He-based neutron detector was configured to count only neutrons that triggered one of the central three wires. The detector was scanned in steps of 0.1^0 over the diffraction peak to obtain the raw data of neutron counts per incident beam fluence versus diffraction angle. A gaussian function on a linear background was fitted to the raw data to obtain the peak parameters: angular position, integrated intensity and full width at half-maximum (FWHM). The intrinsic width of the diffraction peaks was governed by the distance collimation in the apparatus and found to be $(0.73 \pm 0.03)^0$. The temperature at a particular location within the disc, when the heater was activated, was assessed by comparing the angular position and the integrated intensity of the (220) diffraction peak of the Waspaloy matrix to the values obtained with the heater unpowered. Changes in the peak parameters were related to temperature through the calibration curves obtained in Ref. 1. Typically, the diffraction peak position shifted about -0.4^0 from a room temperature value of about 69.4^0, and the integrated intensity was reduced by about 15%. The uncertainties in measuring peak positions and intensities, associated with fitting to the raw data, were, on average, $\pm0.004^0$ and $\pm1\%$, respectively.

3.0   DATA AND ANALYSIS

3.1   Temperature-Analysis Methods

Following the procedure explained in Ref. 1, there are two methods for determining temperature from diffraction data. The first method is based on determination of lattice strain, ε^{th}. The strain is evaluated by comparison of the lattice plane spacing (d-spacing) at the elevated temperature, $d(T)$, with that at the reference temperature, $d(T_0)$, through the relation

$$\varepsilon^{th} = [d(T) - d(T_0)] / d(T_0) \tag{1}$$

The d-spacing is obtained by accurate determination of the scattering angle, ϕ, of the diffraction peak from a specific set of lattice planes, which are defined by Miller indices (hkl). In the present measurements the (220) reflection from the matrix of Waspaloy is analyzed. The relationship between the d-spacing, the scattering angle and the wavelength of the neutron beam, λ, is Bragg's law,

$$d = \lambda / 2\sin(\phi/2) \tag{2}$$

The variation of thermal strain with temperature in Waspaloy was shown, in Ref. 1, to be represented well by a quadratic function of temperature,

$$10^4 \times \varepsilon^{th} = -29.1(1) + 0.0834(6)T + 5.04(3) \times 10^{-5}T^2 \tag{3}$$

In this equation, the reference temperature, T_0, for which the thermal strain is defined to be zero, is 296^0K, the temperature of the unheated disc spinning in air. The constant in Eq. (3) differs from the analogous equation in Ref. 1, for which the zero-strain reference temperature was taken as 293^0K. Since the thermal strains in the disc could be measured to a typical precision of approximately $\pm0.005\%$, it was expected that the temperature could be deduced from Eq. 3 to a precision of 6^0K. In a rotating disc, the lattice strain is also perturbed by stress arising from centripetal forces. However, at 3000 rpm, this strain component can be neglected (see Section 3.3.2).

The second method for determining T is to evaluate the reduction in diffraction-peak intensity as the temperature increases above T_0. Assuming that the vibrations of the atoms about their face centered cubic lattice positions are harmonic, the ratio of integrated intensities at elevated and reference temperatures, I/I_0, is related, to a good approximation, to a material dependent Debye-Waller constant, B, the room-temperature lattice constant, a, the Miller indices (hkl) of the diffraction peak, and the reduced temperature, $t = (T-T_0)/T_0$, through the expression

$$I/I_0 = \exp[-B\, t\, (h^2+k^2+l^2)/(2a^2)] \tag{4}$$

In Ref. 1 it was noted that a simple calibration function was obtained by linearizing the exponential function and plotting $(1 - I/I_0) / (h^2+k^2+l^2)$ against $(T-T_0)$. The slope of the straight line obtained, $0.0537(7) \times 10^{-3}\ ^0K^{-1}$, accurately characterized the relationship of measured diffraction peak intensity to temperature.

The typical statistical precision of determining the diffraction-peak intensity, associated with fitting a gaussian function to the raw data, would have limited the precision of the deduced temperatures to, at best, 12^0K. However, in the present measurements, the fluctuations in intensity that arise from the coarse micro structure of the Waspaloy disc are more significant than neutron counting statistics. Based on the typical grain size, the size of the sampling volume and the solid angle subtended by the detector, the net precision in determining temperature from changes in the intensity of the diffraction peaks was found to be approximately 30^0K, when circumferential averaging was performed.

3.2 Neutron Diffraction Data

3.2.1 Circumferential Distribution of Intensity and Strain

The multichannel scalar recorded scattered neutron intensity over 60 circumferential channels in the disc. A 60-channel spectrum was collected for each

angular position of the neutron detector as it scanned over the range of the (220) diffraction peak. This data-collection process was repeated five times when the sampling volume was located at R=72 mm, with the heating element both on and off. The repeated scans verified the reproducibility of data. The holes in the disc served to verify the reproducibility of circumferential positioning. The data were sorted into individual diffraction peaks (neutron intensity versus scattering angle) at each circumferential position. These peaks were fitted by a gaussian function on a linear background to extract accurate values of the mean angular position and integrated intensity, the raw data for temperature analysis.

Some examples of raw diffraction peaks are shown in Figs. 3.1 through 3.3, corresponding to circumferential channels 4, 2 and 1, respectively. Channel 4 exhibits the expected features. When the heater is turned on, the peak intensity is reduced and the mean scattering angle shifts to a lower value. The peaks are reasonably represented by a single gaussian on a linear background. In channel 2 there are marked departures from the simple single peak line shape, although the overall peak widths, and changes with temperature are still as expected. While, in channel 1, the peak obtained with the heater active is at lower scattering angle, as expected, its intensity, surprisingly, is greater than occurs with the heater off.

The intensity behavior is explained by the coarse micro structure of the disc alloy and the method of data collection. Within the total volume sampled in the measurement, only a subset of the constituent crystallites (grains) are correctly oriented to diffract neutrons into the detector. This sub volume of diffracting grains, denoted as the diffracting volume, is statistically independent of scattering angle and sample orientation only if the material does not exhibit texture (preferred orientations of crystallites) and is fine-grained. On the other hand, the diffracting volume can vary sharply with slight changes in scattering angle, or sample orientation as large grains enter and exit the correct range of orientations to contribute to the diffracted intensity. At constant temperature, the same grains can be made to contribute at each scattering angle, 2θ, only if the sample is half angled, or rotated by angle θ. This half angling would maintain a fixed diffracting volume. In other words, a single subset of the grains within the sampling volume would contribute to the measured intensity at each scattering angle. As the temperature is increased and the diffraction-peak position shifts to lower scattering angle, the sample should also be rotated in a half angling mode to follow the shifting peak. However, since there was no direct coupling between the sample mount and the diffractometer, no half-angling was possible. As a result, the diffracting volume in the coarse-grained disc varied statistically with temperature, and observed changes in intensity did not arise solely from changes in the amplitudes of vibration of atoms about their lattice positions. Irregular line shapes at a given temperature and irregular changes of intensity with temperature are thus explained by the lack of half angling of a specimen with a coarse micro structure.

Fig. 3.4 summarizes the variations of integrated intensity with circumferential location in the disc, both hot and cold. The radial location was R=72 mm. Intensity is lost near positions 25 mm and 55 mm as the sampling volume intersects the diametrically-opposed holes in the disc. The expected statistical uncertainty is

shown on the figure as a bar of length twice the standard error associated with fitting a gaussian function to the diffraction-peak data. The fluctuations of intensity from channel to channel are much larger than this statistical uncertainty. Repeated measurements at low temperature produced data that fluctuated reproducibly, within the statistical uncertainty, at each position; however, the experiment at high temperature produced data with a different pattern of fluctuations. The low temperature results rule out encoder inaccuracy as the source of channel-to-channel fluctuations while the discrepancies between cold and hot conditions were expected from the coarse micro structure. Neglecting the channels corresponding to holes in the disc, the standard deviation of the measured intensity over all other channels may be calculated and denoted σ. Correcting for the average uncertainty in determining intensity by fitting a gaussian to the peak data for each channel, σ^G, the spread in intensities due to fluctuations in the diffracting volume, σ^F, is then obtained through

$$\sigma^F = (\sigma^2 - (\sigma^G)^2)^{1/2} \tag{5}$$

For a low temperature scan in Fig. 3.4, σ^F was found to be 13% of the average intensity, so even if time would allow the collection of large numbers of neutron counts in each channel, coarse grains in the material would prevent us from obtaining the precision of 0.5% in intensity required to determine the temperature to $\pm6^0$K. Modeling the total sampling volume as a collection of equiaxed grains of equal size and random orientation, A may be related to the average number of grains contributing to the signal, and hence to the average grain size. Accounting for the solid angle subtended by the neutron detector, the sampling volume, the multiplicity of the (220) diffraction peak and σ^F, an average grain size of (102 ± 4) μm is obtained. This value agrees with 103 μm, obtained by metallography.

The observed micro structure in the disc is typical for Waspaloy in turbine applications. This means that the diffraction peak intensity method can only provide sufficiently precise temperature values if the sample is half angled. In addition, improvements in the statistical smoothness will be obtained if some means is devised to increase the number of grains sampled. One suggestion to accomplish this involves continuous oscillation of the half angle during the measurements, thereby bringing more grains into the correct orientation for diffraction during the time of data collection. A second suggestion is to replace the constant wavelength diffraction technique with a time of flight method, which would sample many (hkl) reflections simultaneously and hence average over many sub-volumes of correctly oriented grains within the total sampling volume.

Measurements of thermal strain are also influenced by the coarse micro structure, since irregularly shaped peaks, when fitted by a single gaussian function, exhibit small and random shifts in their mean angular positions. The temperatures, deduced from thermal strain, at 60 circumferential positions where R=72 mm are shown in Fig. 3.5. Diffraction data from five repeated scans were summed to provide

intensity versus angle profiles with approximately 1000 counts in the peak. The average uncertainty in temperature arising from fitting this raw data was found to be $\sigma = \pm 9.9^0 K$ and is shown on Fig. 3.5 as a bar of length 2σ. The actual standard deviation of the temperatures deduced at sixty circumferential positions was much larger, $\sigma = \pm 30.3^0 K$. Half angling of the specimen, as occurred in the static calibration measurements , or sampling of more grains would reduce the uncertainty in thermal strain measurements by improving the diffraction peak shapes.

3.2.2 Radial Distribution of Temperature in the Disc

By continuous summing of scattered neutrons, circumferential averages of intensity and strain were obtained at each radial position. The averaging ensured that many more grains contributed to the measured diffraction peaks, so the line shapes were improved. Examples of the circumferentially averaged diffraction-peak data are shown in Figs. 3.6-3.8, corresponding to the radial positions R=46 mm, 72 mm and 85 mm, respectively. All peaks are well-represented by a single gaussian function on a sloping background, indicated by a continuous line on the figure. On increasing the temperature, the mean angular position shifts to lower value, the integrated intensity of the gaussian is reduced and the background level (related to thermal-diffuse scattering) increases, all as expected.

The diffraction peaks in Figs. 3.6-3.8 each required 20 hr of data collection time, although sufficient neutron counts could have been collected to obtain the desired temperature precision in about 8 hr. Some improvements in instrument configuration can be conceived to reduce the necessary data acquisition time to a smaller number of hours, but the time will never be short enough to investigate temperature profiles during power-up transients. The neutron diffraction method is appropriate to gather information on the steady-state conditions of a gas turbine engine.

Table I presents the temperature profile on the surface of the spinning disc as a function of R, measured by thermocouples. Table II presents the results of neutron diffraction temperature analysis by the thermal strain and intensity methods. The data from both tables are presented in Fig. 3.9. The temperatures deduced from neutron diffraction measurements of thermal strain exhibit a smooth trend, with statistical fluctuations similar in magnitude to those of the thermocouples. The precision of the measurements has improved over that observed in Fig. 3.5 because averaging over many more grains has occurred. The neutron temperatures are systematically higher than the thermocouple readings. This is not surprising, because the air cooling of the disc surface could account for a $300^0 K$ difference between the mid-thickness of the disc, characterized by neutron diffraction, and the surface of the disc, characterized by the thermocouples. The average temperature, over all radial positions, obtained by measurements of thermal strain was $(662 \pm 24)^0 K$. This is equal, within the stated precision, to the average temperature obtained from the reductions in the integrated intensities of neutron diffraction peaks, $(647 \pm 76)^0 K$. Though the temperatures deduced from intensity fall within the correct range, they exhibit marked statistical fluctuations, much worse than can

be obtained by thermocouples. While circumferential averaging has introduced enough additional grain-sampling to smooth out the thermal strain analysis, there are still not a sufficient number of grains to eliminate the effects of the coarse micro structure on the intensity analysis. The ability to half-angle the specimen is definitely required before the intensity method will be feasible.

3.3 Effects of Higher Angular Frequency

In a real gas turbine engine the angular frequency of the disc will be about ten times as great as in the present model experiment. This higher angular frequency will distort the measurements of strain and the deduced temperature unless corrective action is taken.

3.3.1 Doppler Shifts in Diffraction Peaks

For many orientations of the spinning disc with respect to the direction of the incident neutron beam, there is a component of velocity of the diffracting plane normal in the scattering plane. An example is the upper beam depicted in Fig. 2.2. The neutrons themselves have a finite speed, in the neighborhood of 2000 m/s, comparable to the tangential component of velocity at the blade tips in a gas turbine. A Doppler effect is expected to distort the diffraction process and to shift the angular positions of the observed diffraction peaks.

The shift is calculated with reference to Fig. 3.10. The scattering plane is defined by the incident and diffracted neutron beams. A Cartesian coordinate system is associated with the diffractometer, with the z axis perpendicular to the scattering plane, the x axis parallel to the cylindrical axis of the disc and the y axis in the plane of the disc. Coordinates in the frame of reference of the diffractometer are denoted (x,y,z), or (R,Θ) while coordinates in the frame of reference of the rotating disc are denoted with primes, (x',y',z'). The disc rotates with angular frequency, w, in radians per second. The tangential velocity, $\vec{u}$, of a point at position (R,Θ) on the disc is the relative velocity of the disc and diffractometer frames of reference. The vector u may be divided into two components, $u_z = -wR\sin\Theta$ and $u_y = wR\cos\Theta$, where u_y is the cause of the Doppler shift in the observed diffraction-peak angular positions.

In a diffraction measurement on a stationary disc, the angle between the incident and diffracted beams would be twice φ, which is the angle between the incident beam and the x axis. Now, with the disc rotating, assume that the direction of the incident beam, in the frame of reference of the diffractometer, is unchanged, with angle φ as shown in Fig. 3.10. magnitude of the incident neutron velocity, v_0, is related to the neutron wavelength, λ, Planck's constant, h, and the mass of the neutron, m, through DeBroglie's relation, $v_0 = h/(m\lambda)$. The incident velocity has components $v_{0x} = v_0 \cos\varphi$ and $v_{0y} = -v_0 \sin\varphi$. Translating to the reference frame of the disc, the apparent y-component of velocity of the incident neutron is increased by the relative velocity, u_y . The apparent wavelength of the incident neutrons in the reference frame of the rotating disc is therefore

$$\lambda' = \frac{\lambda}{\sqrt{\cos^2\varphi + (\sin\varphi + (m\lambda/h)\omega R\cos\Theta)^2}} \tag{6}$$

The angle of the incident beam with respect to the y-axis, in the frame of the disc, α, is

$$\alpha = \arctan[v_0\cos\varphi / (v_0\sin\varphi + \omega R\cos\Theta)] \tag{7}$$

Diffraction occurs in the frame of the disc. The scattering angle, $\varnothing'$, is obtained from Bragg's law

$$\lambda' = 2\, d_{hkl}\, \sin(\varnothing'/2) \tag{8}$$

where d is the spacing between the atomic planes in the material, described by Miller indices, (hkl). The angle, β, made between the -y-axis and the diffracted beam, in the frame of the disc, is the sum of $\varnothing'$ and α. In the frame of the disc, the magnitude of the diffracted neutron velocity, v_1', is equal to that of incident beam, which is $h/(m\lambda')$. However, in translating back to the diffractometer frame of reference, the relative velocity must be added, giving net velocity components $v_{1x} = v_1' \sin\beta$ and $v_{1y} = -v_1' \cos\beta + \omega R\cos\Theta$. The magnitude of the diffracted neutron velocity, v_1, in the frame of the diffractometer, is not equal to that of the incident neutrons unless the relative velocity term, $\omega R\cos\Theta$, is zero. Instead, it has the value

$$v_1 = \sqrt{(h/(m\lambda'))^2\sin^2\beta + [(h/(m\lambda'))\cos\beta - \omega R\cos\Theta]} \tag{9}$$

The Doppler-shifted diffraction angle, $\varnothing$, observed in the frame of reference of the diffractometer is defined by

$$\varnothing = \arccos[(v_{0x}v_{1x} + v_{0y}v_{1y})/(v_0\, v_1)] \tag{10}$$

Calculations of the diffraction angle in a disc rotating at 3000 rpm are shown in Fig. 3.11. Curves indicate the variation of the diffraction angle with the location of measurement, defined by the coordinates R and Θ. At larger values of R, the magnitude of the tangential velocity is increased and so are the Doppler shifts. Most of the measurements in the present report were made along the radius with $\Theta = 90^0$, where the Doppler effect vanishes. The single measurement made at $(R,\Theta) = (81\ mm, 8^0)$ to demonstrate Doppler effects is shown on the figure, with an error bar representing twice the standard error of fitting the diffraction peak with a gaussian function on a linear background. The calculated curve that agrees with this data point has a radial coordinate, R, of 78 mm. The experimental and fitted radial coordinates agree within the uncertainty associated with vertical positioning of the enclosed disc on the neutron diffractometer.

For future applications, a second calculation of Doppler shifts for a disc spinning at 30,000 rpm is shown in Fig. 3.12. At this angular velocity, typical of a running gas turbine, the diffraction peak shifts due to the Doppler effect would be of the order of a few degrees, if Θ is near 0^0 or 180^0. These Doppler shifts are about 100 times larger than shifts to be expected from dynamic strain, and 10 times larger than shifts to be expected from high temperatures in the turbine disc. The measurement of thermal strain at values of Θ other than 90^0 requires the ability to average results from accurately set values of Θ and 180^0 - Θ. Alternatively, accurate knowledge of ω, Θ and the other geometrical coordinates would permit a correction through the calculation in this section.

3.3.2 Lattice Strain due to Centripetal Forces in a Spinning Disc

A rotating, elastically deformable disc is in a state of dynamic stress due to centripetal forces. There will be corresponding elastic strains that cannot be separated from the thermal strain in a single measurement of lattice expansion. The principal components (normal (N), radial (R) and hoop (H)) of the dynamic stress are given in Ref. 2. The component normal to the plane of the disc is zero. The radial and hoop components of stress, σ_R and σ_H respectively, are functions of disc radius, b, material density, ρ, the angular frequency, ω, Poisson's ratio, ν, and the radial position on the disc, R. Their values are obtained from

$$\sigma_R = \frac{\rho\omega^2}{8} (3 + \nu) [b^2 - R^2] \tag{11}$$

$$\sigma_H = \frac{\rho\omega^2}{8} (3 + \nu) [b^2 - \frac{(1+3\nu) R^2}{(3+\nu)}] \tag{12}$$

The dynamic stresses produce elastic strains in the material, and are manifested as (hkl)-dependent shifts in the diffraction peak positions. The strains are given by the set of equations,

$$\varepsilon_R = (\sigma_R - \nu_{hjl} \sigma_H) / E_{hjl}$$

$$\varepsilon_H = (\sigma_H - \nu_{hjl} \sigma_R) / E_{hjl}$$

$$\varepsilon_N = -\nu_{hjl} (\sigma_H + \sigma_R) / E_{hjl} \tag{13}$$

The diffraction elastic constants, Young's modulus, E_{hjl}, and Poisson's ratio, ν_{hjl}, relate the macroscopic stress field to the strains determined in particular lattice directions, < hkl >. The method by which the diffraction elastic constants are determined within the Kröner model of elasticity, assumes polycrystalline material with nearly spherical grains, and a random distribution of crystallite orientations.

Since the present set of temperature measurements were made from shifts in the

71

(220) diffraction peak, it is important to evaluate the strains, in the <220> direction, that arise from the dynamic stresses. The values for E_{220} and ν_{220} , calculated from the single crystal elastic constants of pure nickel[4] are scaled by the ratio of bulk elastic constants for Waspaloy and pure nickel to obtain the effective values, $E_{220} = 248$GPa and ν_{220} = 0.31 for Waspaloy. Other parameters typical of the present experiment are a disc radius of 100 mm, a density for Waspaloy of 8.19×10^3 kg/m^3 and a rotational rate of 3000 rpm. The three principal components of strain as a function of radial position, R, are shown in Fig. 3.13. In the present experiment, the radial component of strain was measured. For all R, the magnitude of strain due to spinning is less than 20% of the strain measurement precision and corresponds to a temperature error of less than 1^0K. Thus, in the present experiment, the dynamic strains could justifiably be ignored. However, increasing the rotational rate to 30,000 rpm, more typical of the speeds in a gas turbine engine, produces much larger strains, as depicted in Fig. 3.14. In this condition the dynamic strains attain levels of 9×10^{-4} , corresponding to temperature shifts of about 80^0K. Thus, in an operating gas turbine engine it is important that dynamic and thermal strains be separated by combining strain measurements in different sample directions and by applying the peak intensity method, which does not depend strongly on the stress state of the specimen.

4.   CONCLUSIONS.

It is feasible to collect neutron diffraction data on a spinning disc with dimensions similar to those of an actual turbine disc. The data were successfully separated into circumferential channels through a magnetic pick-up near a slotted disc; however, at higher angular velocity, an encoder with intrinsically sharper transitions may be required. Also, it was shown that the specimen location could be varied to measure the temperature at specific radial and through thickness positions.

The temperatures in 60 circumferentially-distributed channels could not be determined with adequate precision because the coarse micro structure of the material produced irregular diffraction peak shapes, and large fluctuations in the diffracting volume. To improve the precision, more grains must be sampled either by rocking the half-angle through a small range during or by circumferential averaging. To further improve the precision, the specimen should maintain, on average, a half angle relationship to the scattering angle, to ensure that the same diffracting volume contributes to the measured neutron intensity at each scattering angle.

Circumferential averaging of data provided temperature measurements, as a function of radial position, with a precision similar to that obtained with thermocouples. These measurements were based on the neutron diffraction measurement of thermal strain. On the other hand, circumferential averaging was not sufficient to obtain adequate precision in temperature measurements through the changes in neutron diffraction peak intensity, though the values were statistically scattered about the correct mean.

Typical neutron fluxes and instrument configurations will limit the neutron diffraction

method of temperature measurement to applications where a specimen can be held in a steady state for a few hours.

In an operating gas turbine engine, the angular frequency of the disc will be about 10 times greater than that of the disc in the present series of tests. The Doppler effect, verified in the current tests, will dominate the apparent strain when the scattering plane does not contain the axis of the disc. To overcome the Doppler effect, it must be possible to exactly locate the disc axis in the scattering plane of the diffractometer. Also, while the strain due to the dynamic stresses in the current spinning disc could be neglected, in an actual gas turbine, the dynamic strains will correspond to apparent temperature shifts as much as 80^0K. The neutron diffraction method based on intensity measurements is least sensitive to dynamic stresses, and is the preferred route to obtain temperature information, if the effects of micro structure and subtle changes in diffraction geometry can be removed. The thermal-strain method may be successful on its own, but it must be feasible to measure strain in a number of directions and extract the direction independent (thermal) strain. Alternatively, the stress state of the spinning disc at the locations of temperature measurement must be calculated accurately, and the corresponding strains removed from the net strain observed.

Overall, the present experiments encourage one to proceed with a demonstration that the temperature can be measured noninvasively, by neutron diffraction, in an operating gas turbine engine.

5. ACKNOWLEDGMENTS

6. REFERENCES

1. T.M. Holden, J.H. Root, D.C. Tennant, D. Kroeze "Measurement of Strain and Temperature for Waspaloy and the Titanium Alloy AMS 4928 Under Conditions of Static Loading", Report ANDI-38 made for Pratt & Whitney Canada Inc. by AECL Research, Chalk River, Ont. Canada, K0J 1J0

2. W. Johnson and P.B. Mellor, Engineering Plasticity, Van Nostrand Reinhold Co., London.

3. H. Behnken and V. Hauk, Z. Metallkde. 77, 620-625 (1986).

4.   Smithells Metals Reference Book, 6th ed., E.A. Brandes editor, Butterworths, Toronto, (1983).

Table 1

Thermocouple	Radius (mm)	Temperature (^{0}K)
1	98.2	665 (2)
2	73.7	642 (1)
3	48.3	610 (1)
4	26.4	564 (2)
5	92.0	667 (1)
6	76.2	642 (1)
7	42.9	593 (1)

Radial positions of thermocouples on the surface of the Waspaloy disc, and average temperatures obtained when the heating element was activated. The numbers in parentheses are uncertainties derived from the spread of values read over a period of 10 days. With the heating element unpowered, the average temperature over all thermocouples was (296 ± 1) ^{0}K.

Table 2

Radius (mm)	Temperature (^{0}K)	
	from Strain	from Intensity
34	616	550
46	641 638 *	606
72	660 667 *	574
85	678 682 *	718
91	677	765
97	693	706

Temperatures deduced from neutron diffraction measurements of thermal strain and integrated peak intensity. The uncertainty expected for the strain deduced temperature, based on typical errors in fitting the data with a gaussian function on a linear background, are $\pm 6^0$K. For the intensity deduced temperatures the expected uncertainty is $\pm 12^0$K; however, the actual uncertainty in the intensity measurements is much higher ($\pm 30^0$K) and is traced to the coarse micro structure of the disc. Temperatures indicated with an asterisk (*) were deduced with reference to the unheated disc after completion of measurements at high temperature. Otherwise, reference measurements were made before the disc was heated.

WASPALOY DISC

Thermocouples

Through-thickness Hole

1 2 3 4 5 7
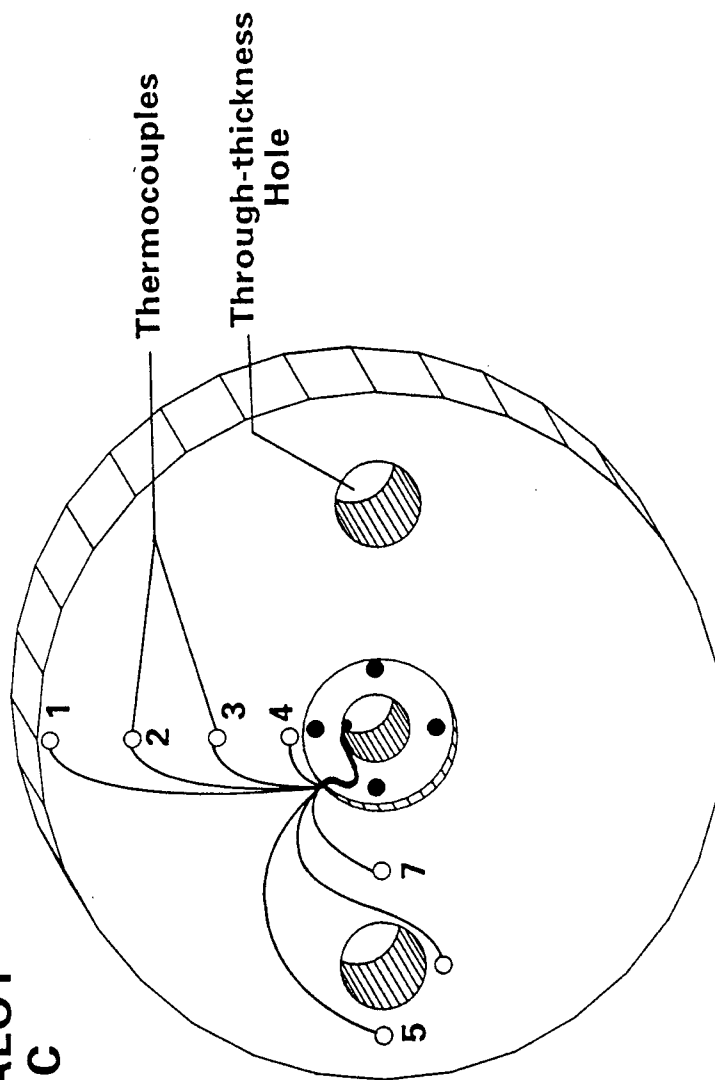
Fig. 2.1 Positions of thermocouples on the surface of the Waspaloy disc.

77
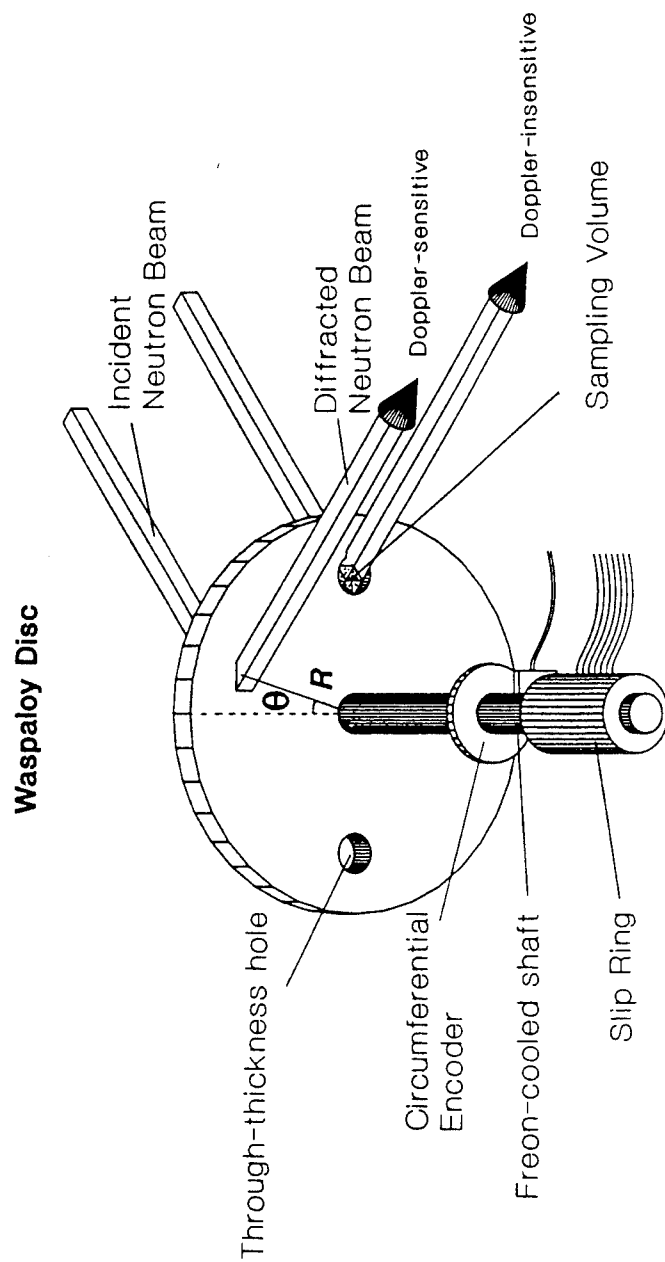
Fig. 2.2 The scattering geometry for measurement of neutron diffraction peaks at mid-thickness of the Waspaloy disc. The disc was enclosed by an insulated container and an electrical heating element was located around the perimeter of the disc.
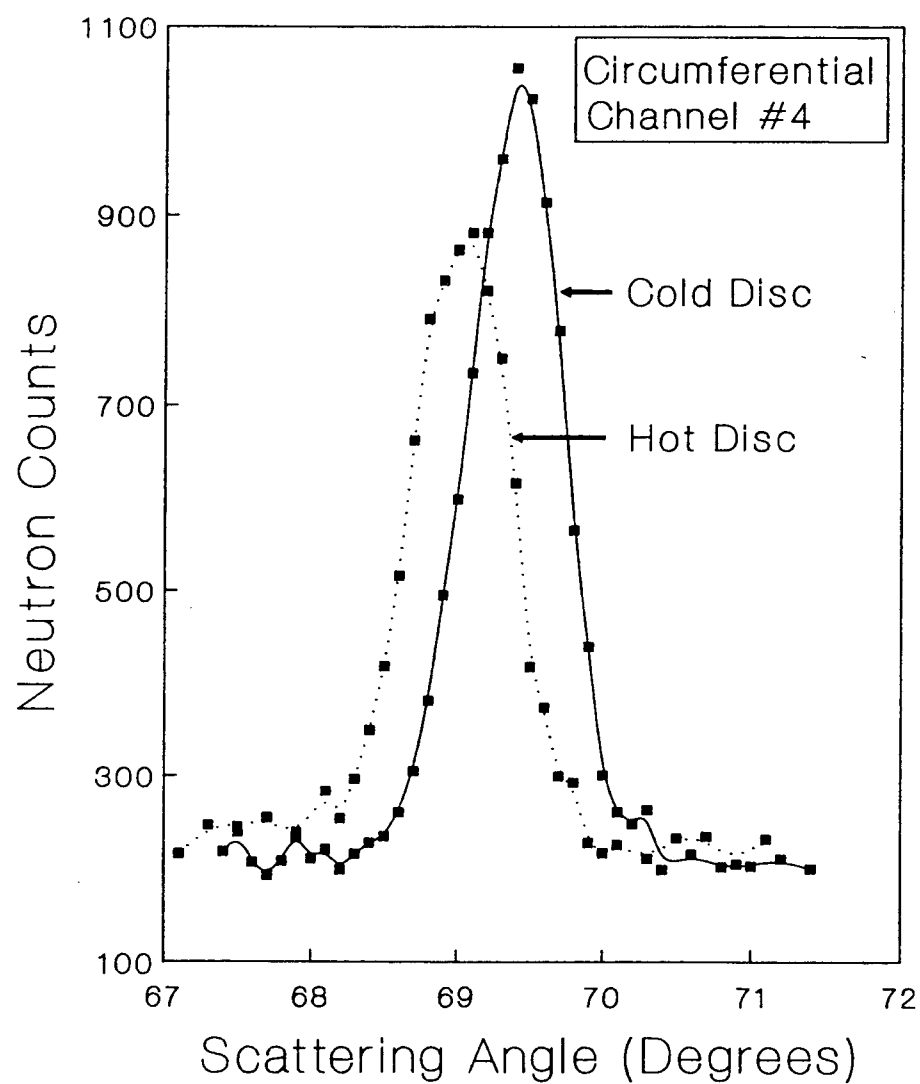
Fig. 3.1 Diffraction peaks obtained by summing 5 consecutive scans at circumferential position 4, with the disc in both hot and cold states. The lines are cubic splines and serve to guide the eye.
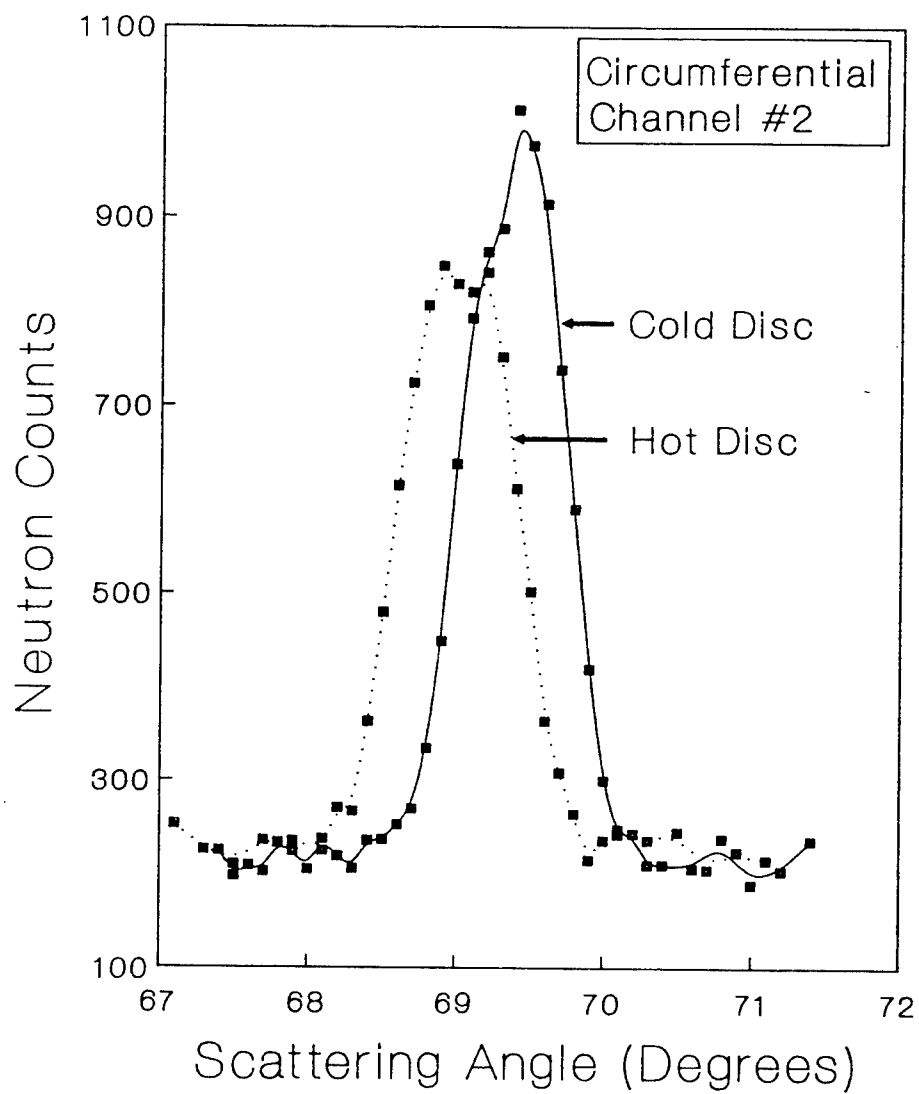
Fig. 3.2 Diffraction peaks obtained by summing 5 consecutive scans at circumferential position 2, with the disc in both hot and cold states. The lines are cubic splines and serve to guide the eye.
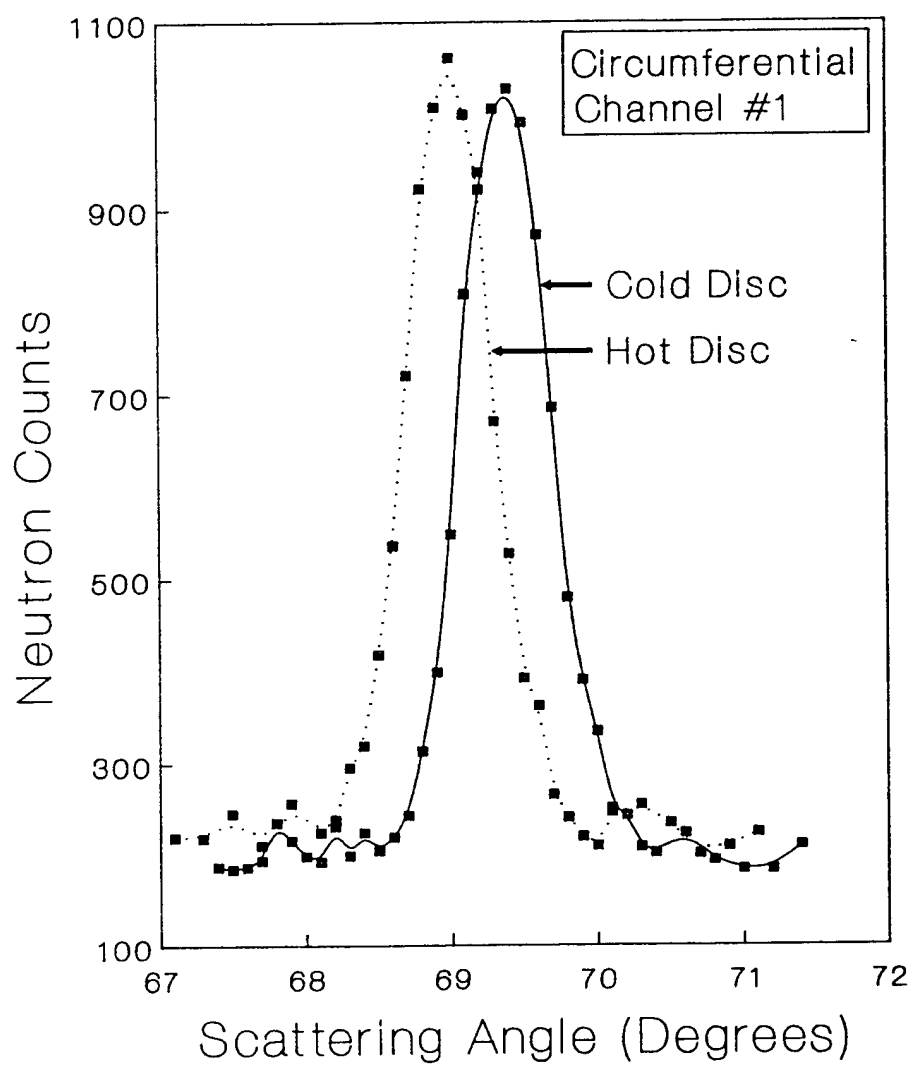
Fig. 3.3 Diffraction peaks obtained by summing 5 consecutive scans at circumferential position 1, with the disc in both hot and cold states. The lines are cubic splines and serve to guide the eye.
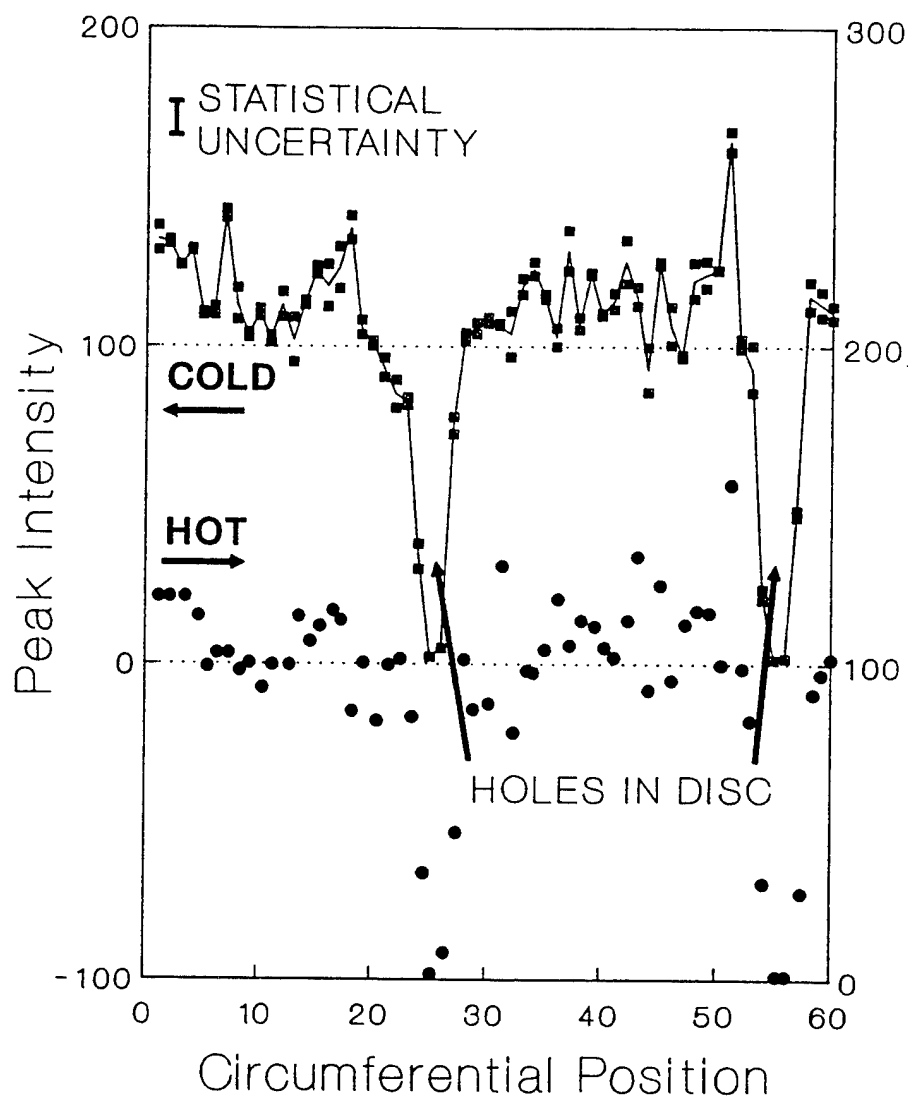
Fig. 3.4 Integrated intensity of diffraction peaks as a function of circumferential position. Small squares indicate two consecutive scans with the heater off and the continuous line joins points that average the two scans. Intensity for these data is plotted on the left-hand axis. The solid circles indicate a scan with the heater on, with intensity plotted on the right-hand axis. The error bar is twice the typical standard error in integrated intensity, arising from fitting a gaussian on a linear background to the raw diffraction peak data.
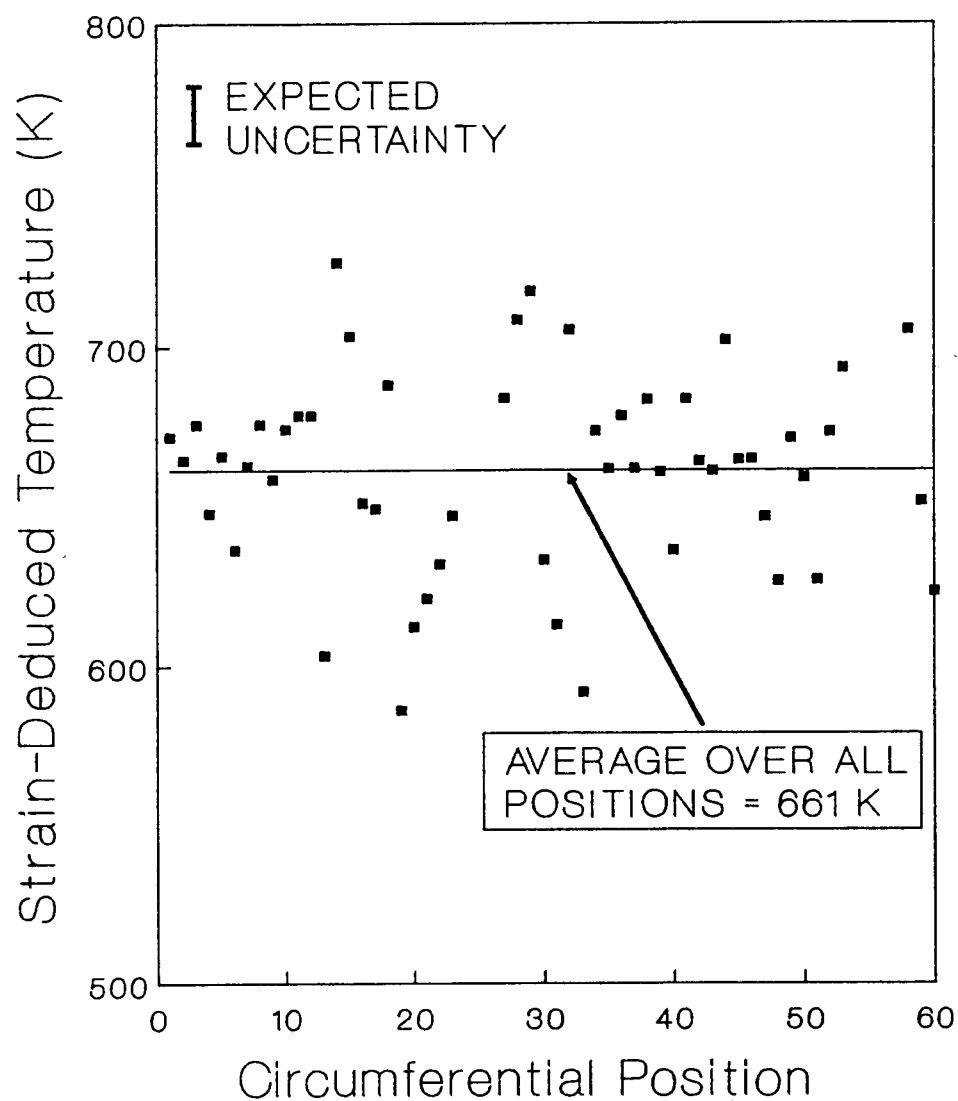
Fig. 3.5 Temperatures deduced from thermal strain as a function of circumferential position. The raw data are summed peaks from 5 consecutive measurements at R = 72 mm. The length of the error bar is twice the standard error inferred from the uncertainty in fitting a gaussian on a linear background to a typical diffraction peak.
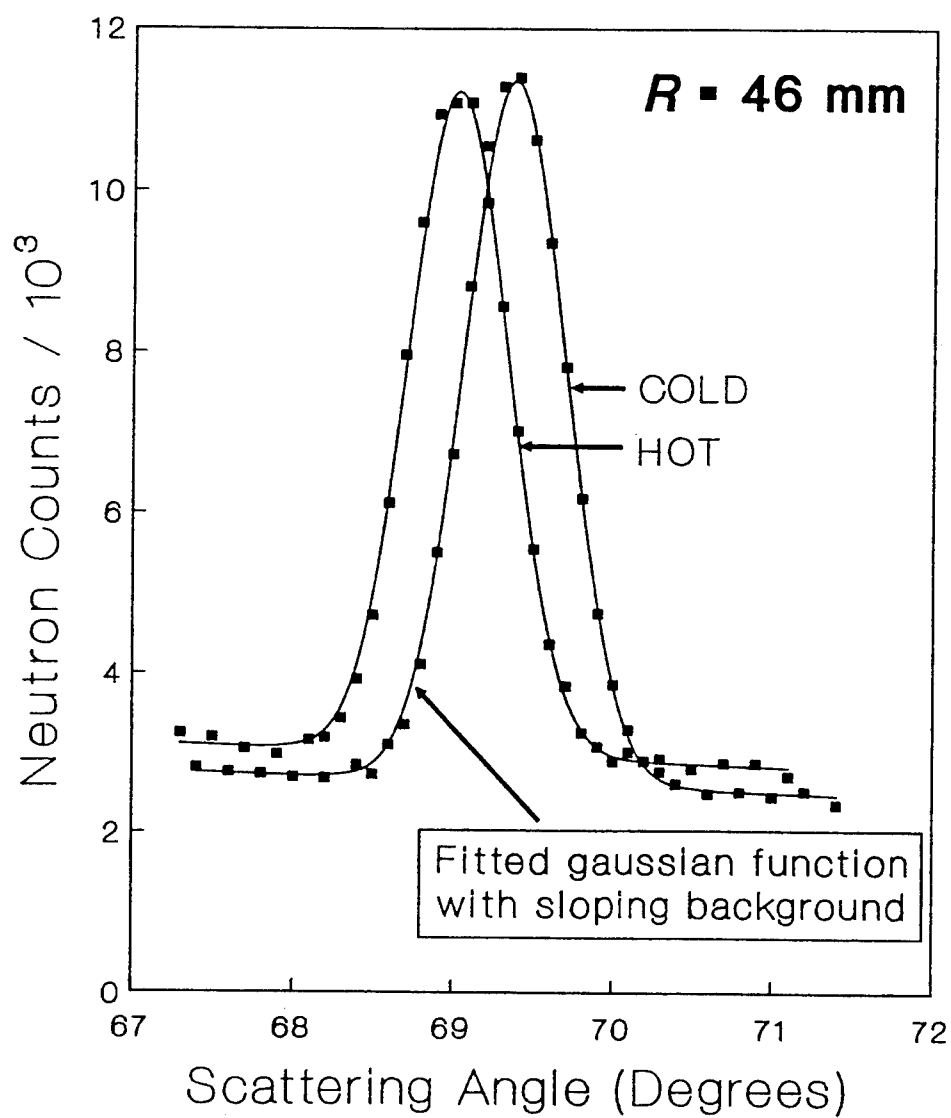
Fig. 3.6 Diffraction peaks obtained by circumferential averaging of intensity at R = 46 mm, with the disc in both hot and cold states. Each continuous line shows a fitted gaussian function on a linear background.

84
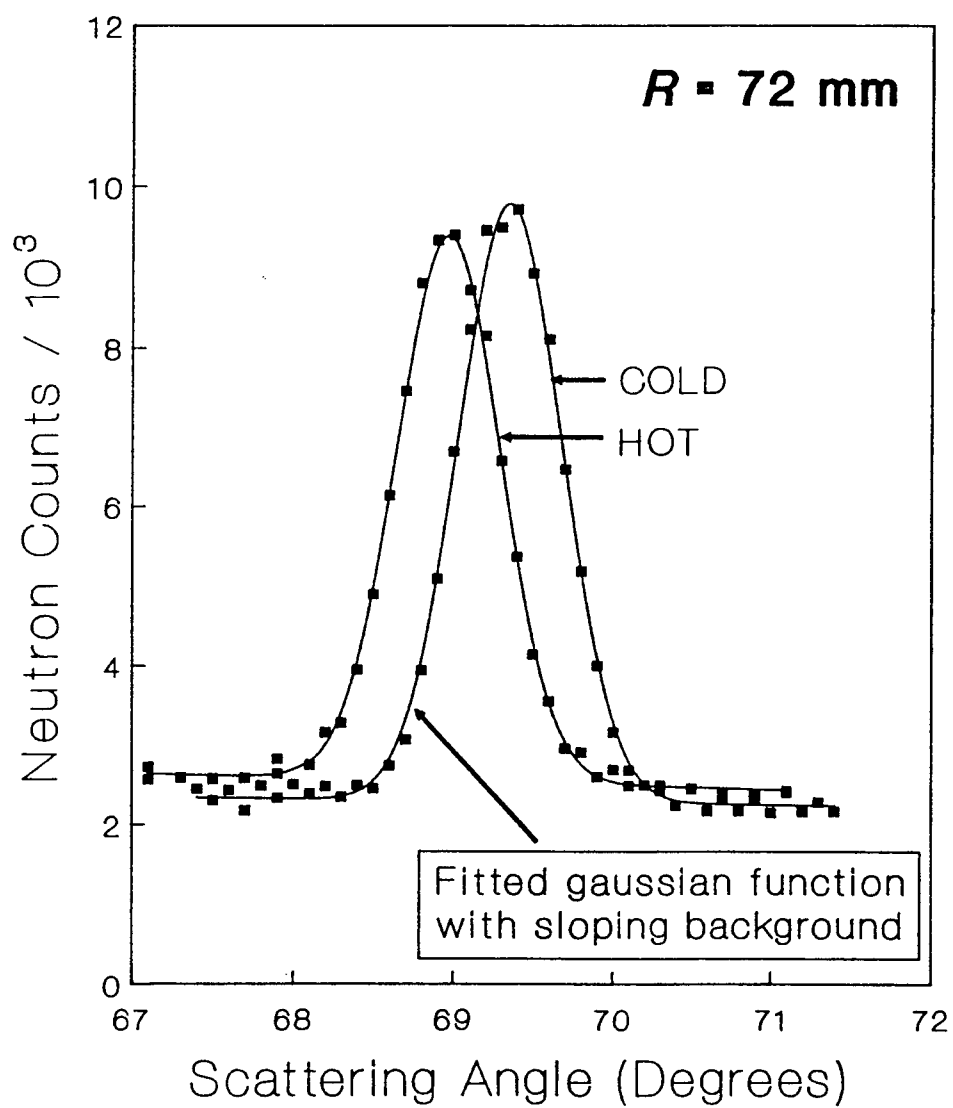
Fig. 3.7   Diffraction peaks obtained by circumferential averaging of intensity at R = 72 mm, with the disc in both hot and cold states. Each continuous line shows a fitted gaussian function on a linear background.
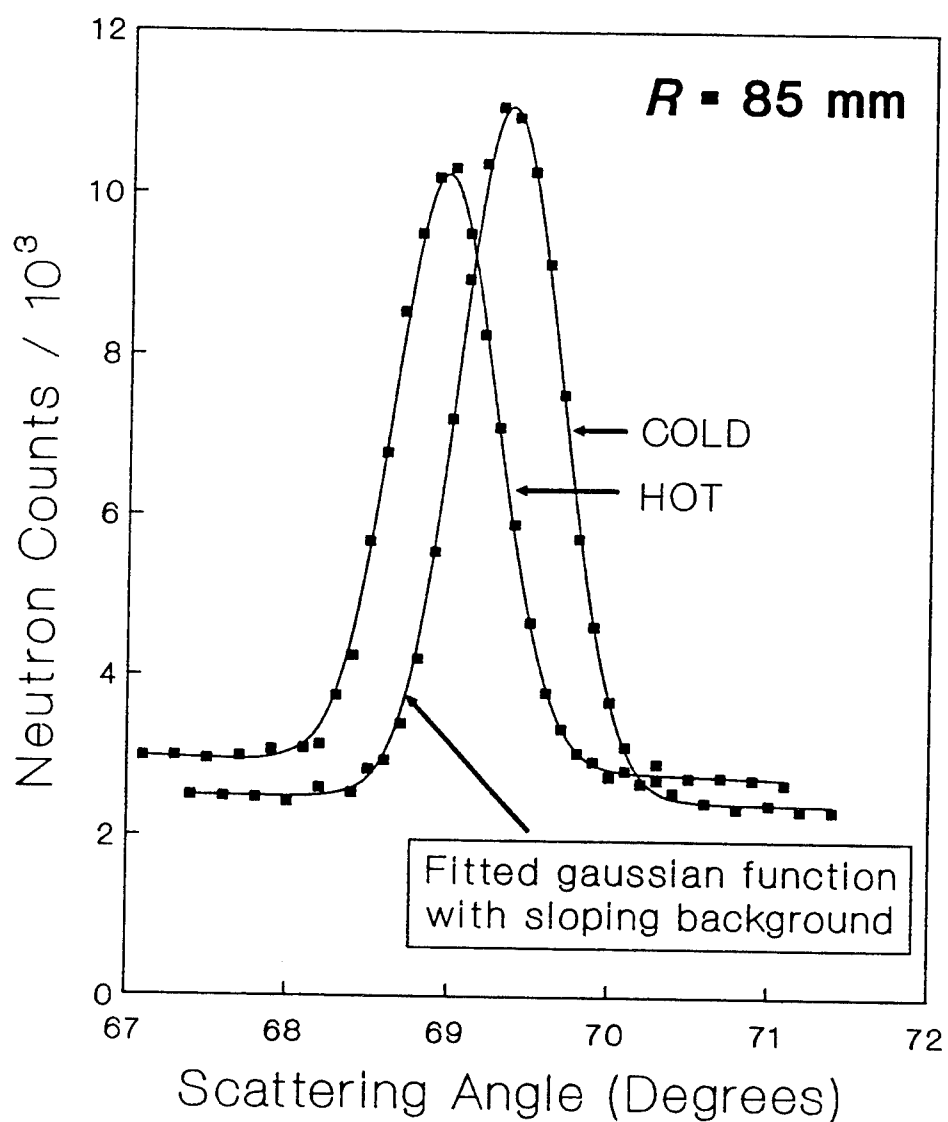
Fig. 3.8 Diffraction peaks obtained by circumferential averaging of intensity at R = 85 mm, with the disc in both hot and cold states. Each continuous line shows a fitted gaussian function on a linear background.
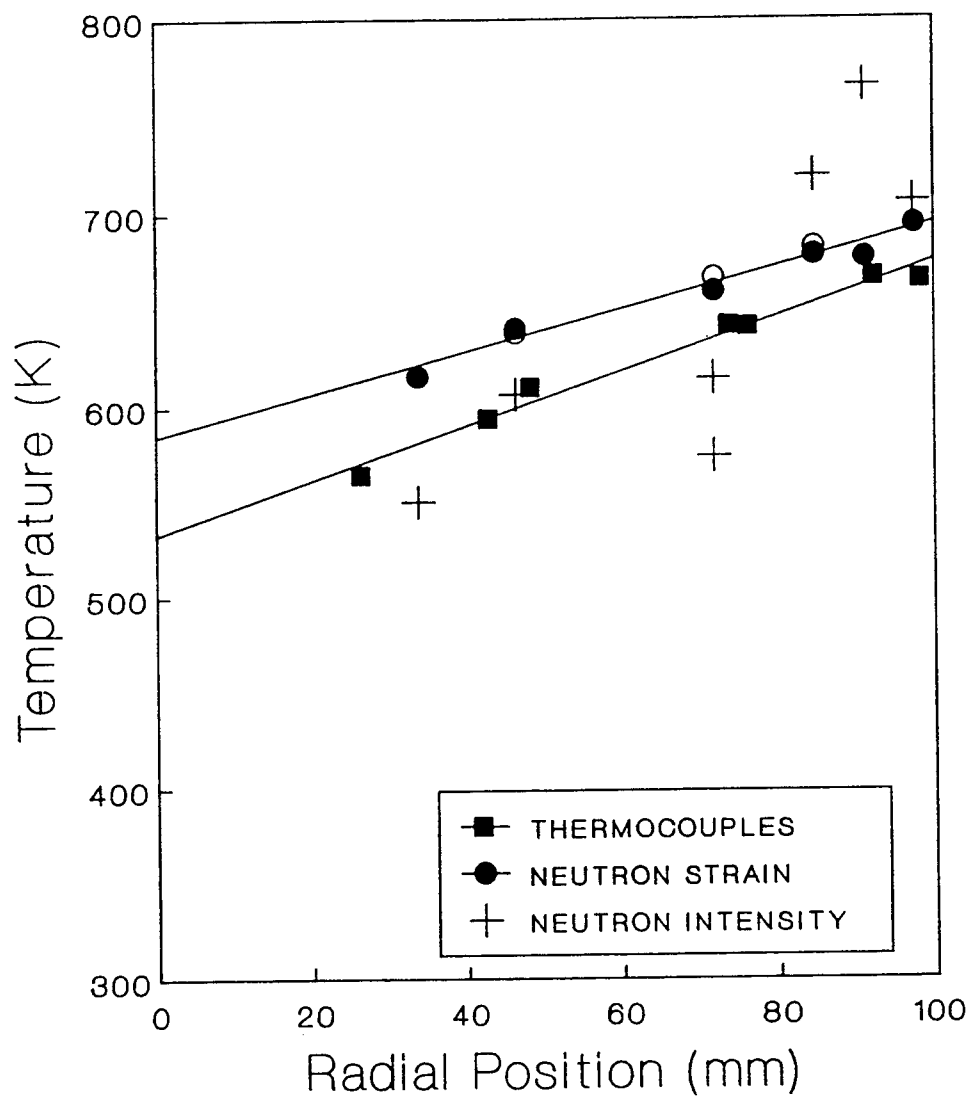
Fig. 3.9 The temperature profile in the spinning disc with the heater activated, as determined by thermocouples and the 2 neutron diffraction methods, with circumferential averaging. The lines are least-squares fits to the neutron (thermal strain) and thermocouple data, serving to guide the eye. The electrical heating element is located at R = 106 mm.
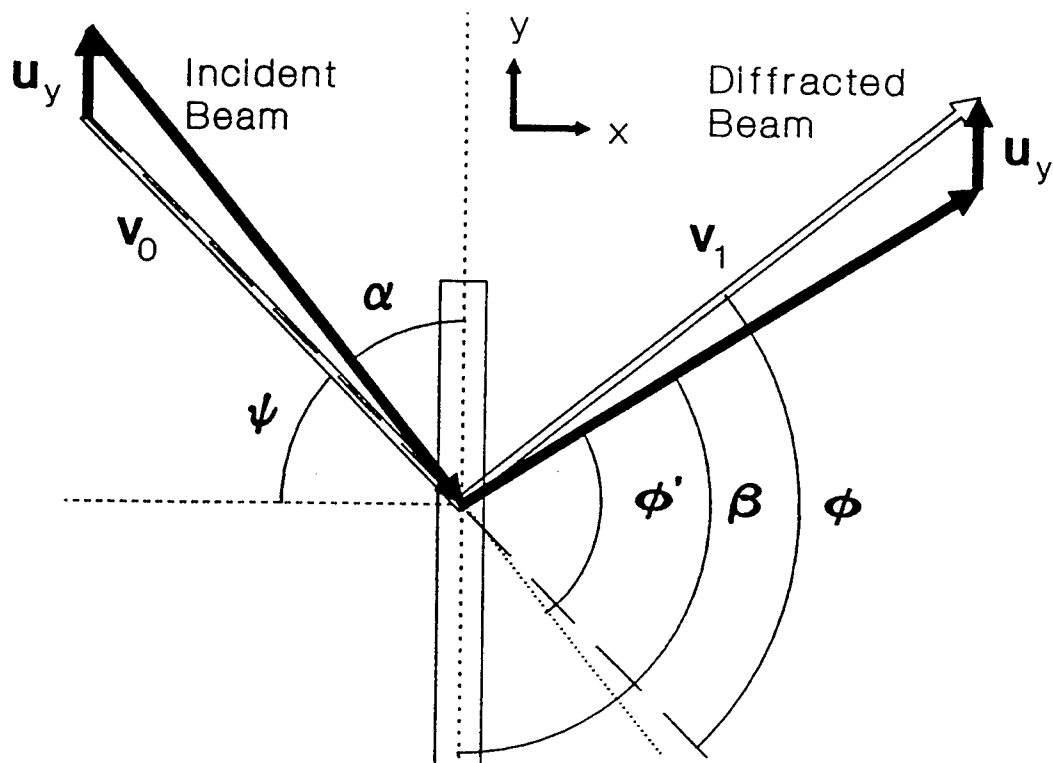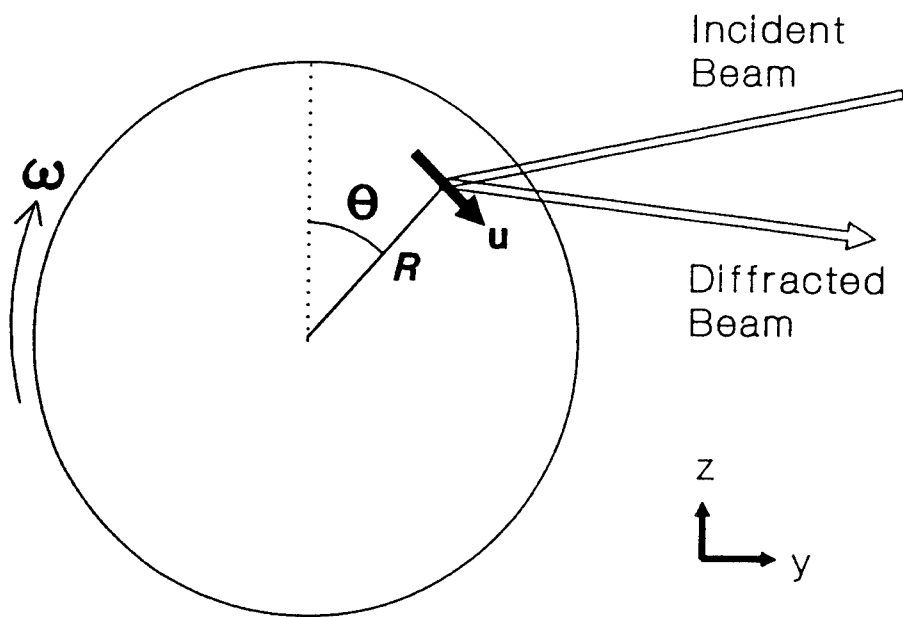
Fig. 3.10 Definition of coordinates and angles for a calculation of the Doppler effect in a spinning disc.
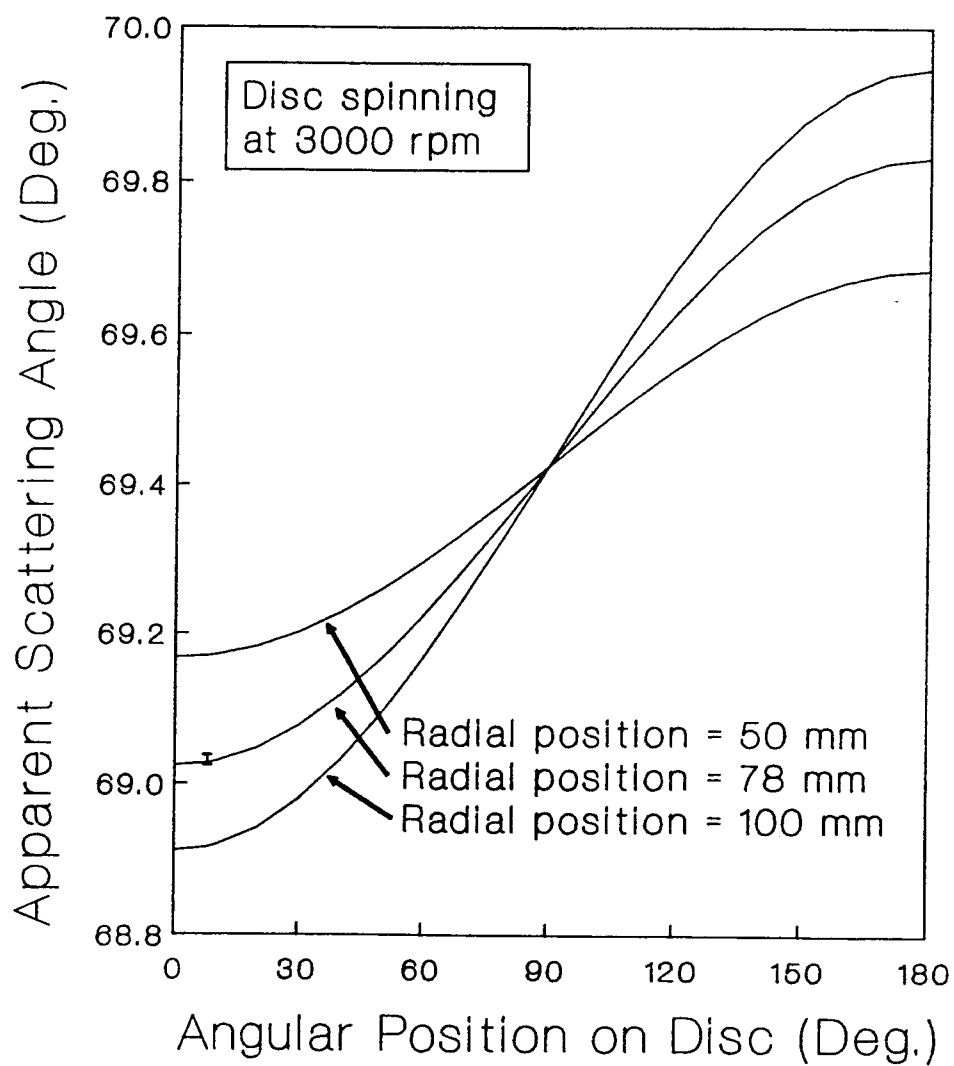
Fig. 3.12 The apparent mean scattering angle of the (220) diffraction peak as a function of angular position, Θ, on a disc spinning at 3000 rpm The error bar indicates the observed position of the diffraction peak when measurements were made with the disc axis below the scattering plane.
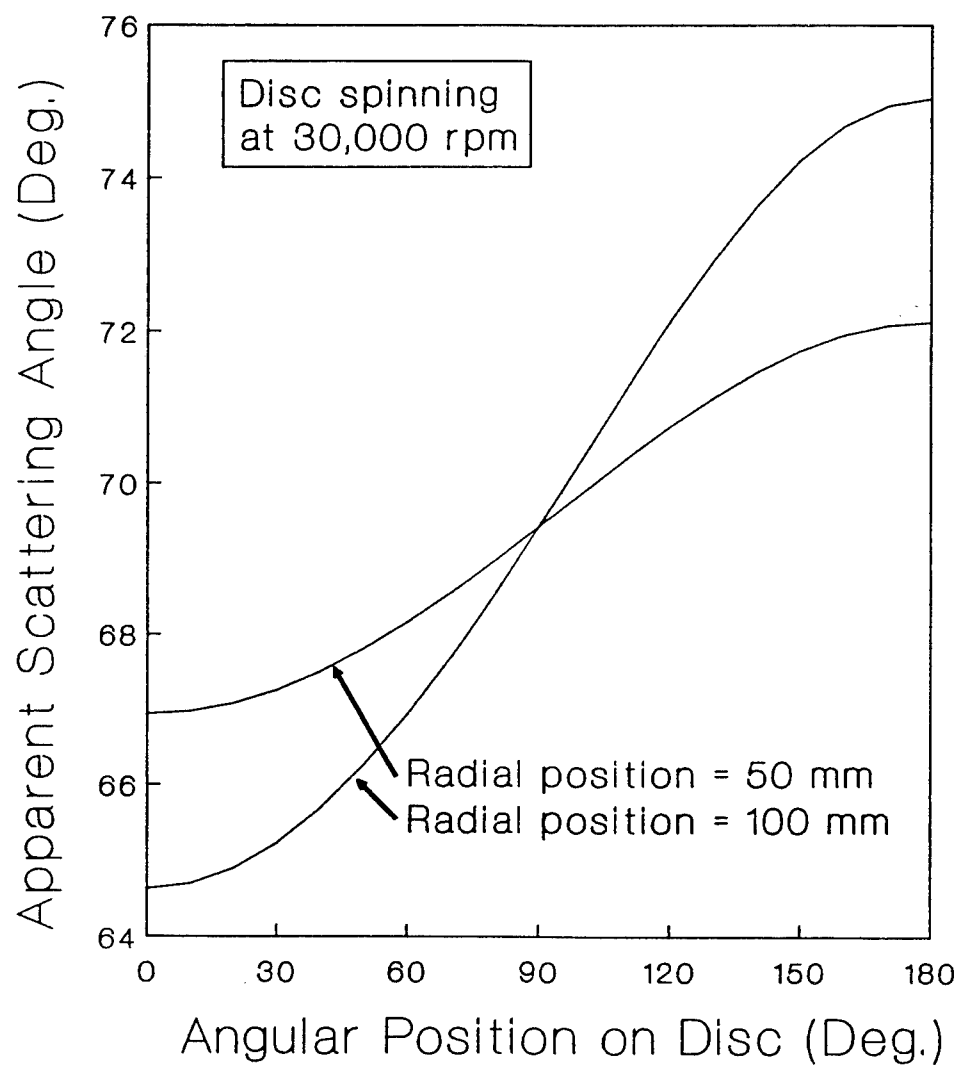
Fig. 3.13   Typical Doppler effects in a disc spinning at 30,000 rpm
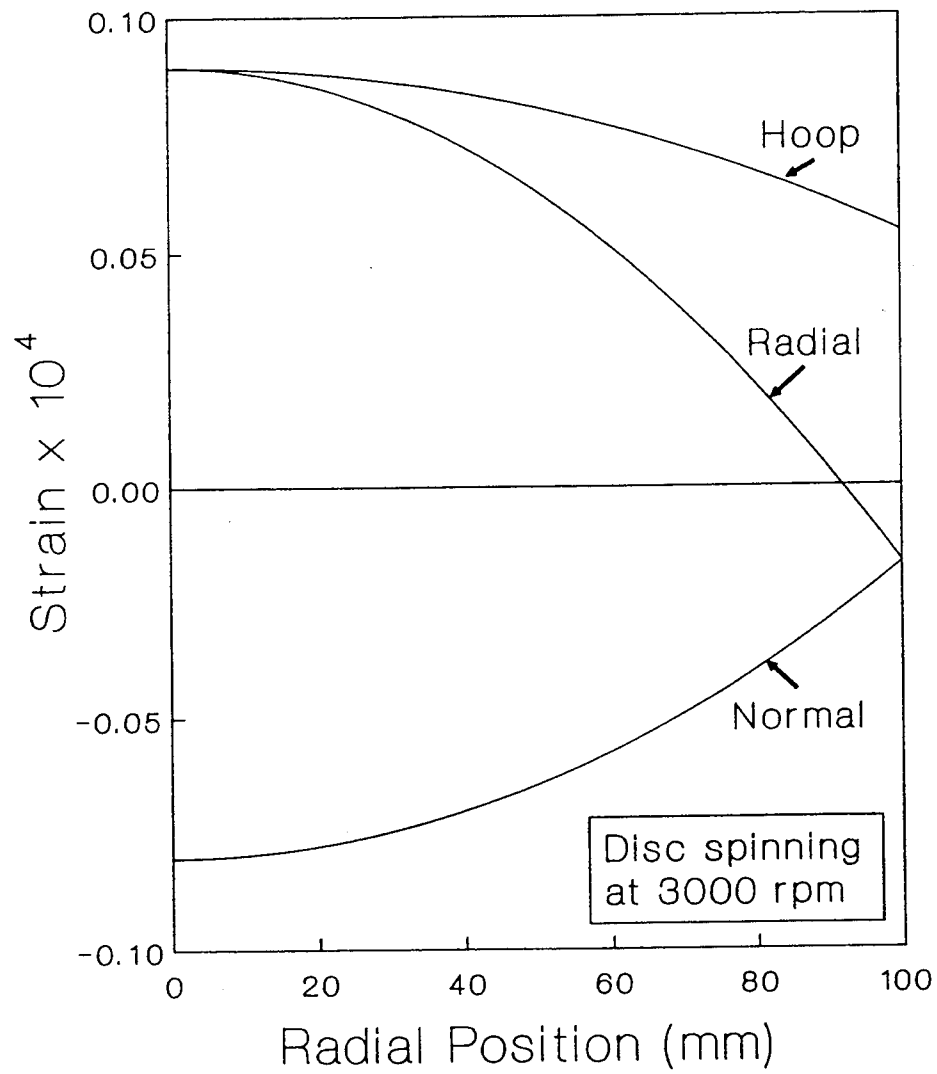
Fig. 3.14 The three principal components of strain due to dynamic stresses in a disc spinning at 3000 rpm, as a function of radial position, R.
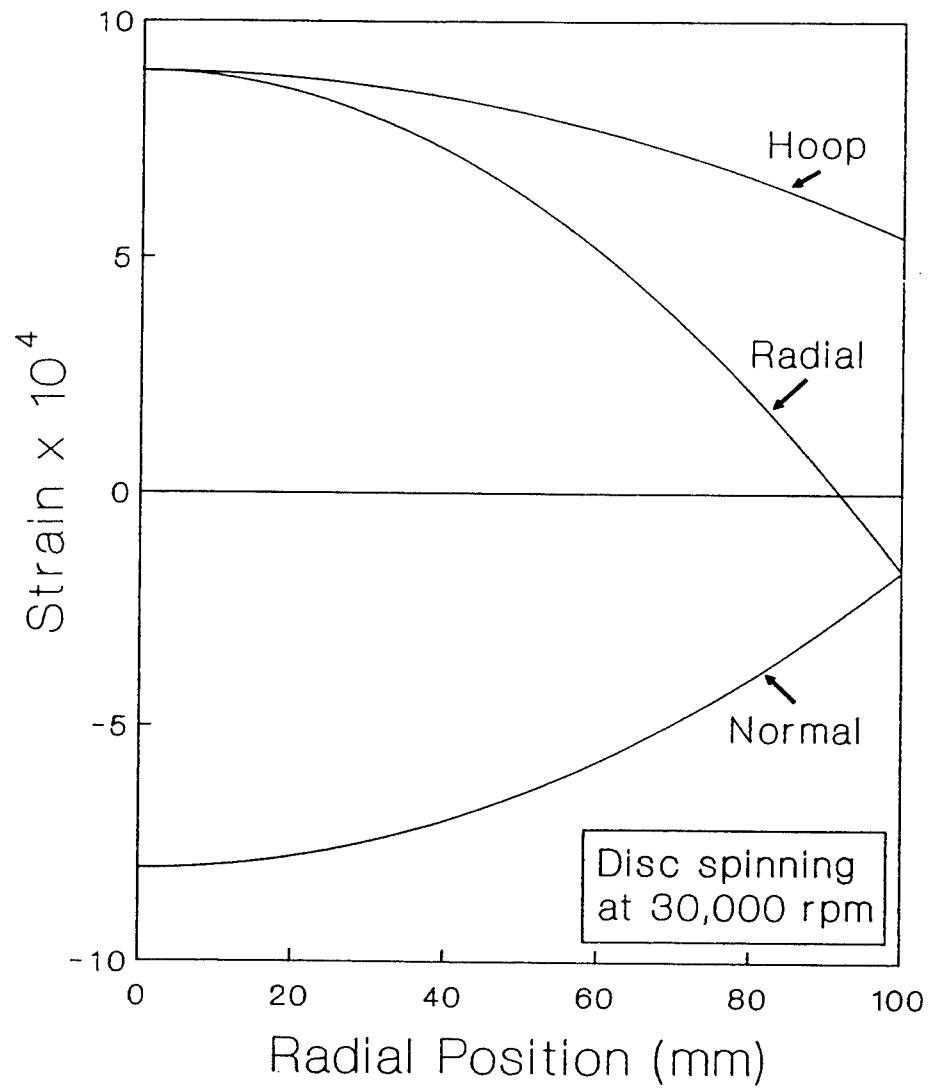
Fig. 3.15   The three principal components of strain due to dynamic stresses in a disc spinning at 30,000 rpm, as a function of radial position, R.

APPENDIX D

ANDI - 73 COLD   ENGINE   TEST

COLD ENGINE TEST

T.M. Holden and J.H. Root

ABSTRACT

Measurements of neutron diffraction from the turbine disc in a PT6 engine have been carried out. The transmission through other structures in the engine causes a loss of intensity by a factor of 25, corresponding to a total neutron path length of 3.5 cm through nickel-based alloy.

Neutron and Condensed Matter Science Branch
AECL Research, Chalk River Laboratories
Chalk River, Ontario, Canada K0J 1J0

1994 January

1.0   INTRODUCTION

Previous reports [1,2] (Appendices B and C) have established the proof of principle for measuring temperature noninvasively by neutron diffraction. Measurements were made in static samples of Waspaloy and Titanium alloy and in a Waspaloy turbine disc rotating at 3000 rpm. Several papers in the scientific literature [3,4,5] have described the results. The experimental method and the accuracy of measurement were established and some of the experimental difficulties in applying the method to real components were uncovered. This report addresses the question of the practicalities of mounting a PT6 engine on the neutron spectrometer at the reactor, of locating the turbine disc in the gage volume, and determining the attenuation of the incident and diffracted neutron beams on passing through the engine components. The report is arranged as follows: details of the experimental arrangement are described in Section 2 and the results, including a mapping of some engine components in the horizontal plane are given in Section 3.

2.0   EXPERIMENTAL

The experiment was carried out on the L3 spectrometer at the NRU reactor, employing the (113) planes of a silicon monochromator to provide neutrons of wavelength 1.719Å. With this arrangement the (220) and (113) peaks of the Waspaloy turbine disk are at scattering angles near 85.0^0 and 105.3^0 respectively. The possibility of measuring either of these peaks was important since the loci of the incident and scattered neutron paths could be varied a little to avoid particularly thick sections within the engine. The experiment was eventually carried out with collimation and a single detector scanning over a range of scattering angles to measure the peak position. Considerable effort, however, was made at the start of the experiment to design a modification of the multidetector system to enhance the efficiency of data collection. As a result of these initial efforts the multidetector can be utilized to increase the data collection rate by a factor of about four.

The PT6 engine was mounted on a robust XY translator on the spectrometer table by counter weighing it from a support frame passing over the center of the table. The arrangement is shown in Figure 1. The axis of the engine was arranged to lie parallel to the bisector of the incident and scattered beams and therefore the neutrons were reflected off the face of the turbine disc. In this configuration there is no Doppler effect.

The principal problem encountered is that all the structures within the engine are manufactured from Ni-based alloys which have nearly the same lattice parameters. Therefore, the position of the diffraction peak, which is a means of identifying the material and thus useful for identifying a particular component, is not unambiguous. It was therefore necessary to fix the scattering angle of the spectrometer at the maximum count position for the Waspaloy disc used in Reference 2, and to move the engine parallel and perpendicular to the scattering vector on an X-Y grid to locate elements of the engine structure which we could recognize and eventually to identify the disc.

95

Figure 2 shows an engineering drawing of the engine showing the turbine disc, the attached turbine blades and the stator vanes at the end of a curved passage through which the hot gas mixture passes prior to falling on the turbine blades.

3.0   EXPERIMENTAL RESULTS

The map of the engine structure determined by neutron diffraction is shown in Figure 3. Each cross corresponds to a maximum in neutron signal as the engine was moved through the gauge volume in either the axial or radial direction. The outer cover of the engine is identified. The outermost skin of the hot gas passage and the inner skin are readily recognized by the curved shape of the component. The static vane appears as a series of peaks created within the hot gas passage. The location of the turbine disc is therefore to the rear of the static vane in the region of axial position 13.5 cm and at a radial position in the range 18-20 cm. The (113) diffraction peak recorded at $(X, Y) = (13.6, 20$ cm$)$ is shown in Figure 4 and required 46 minutes of counting time. The loss of intensity due to passage of the beam through other parts of the engine structure, as obtained by comparison with the Waspaloy disc used in Reference 2, is about a factor of 25. The corresponding thickness of nickel based alloy to deplete the beam by this factor is 3.5 cm. The integrated intensity in the diffraction peak is plotted as a function of radial position at a fixed axial position of 13.3 cm in Figure 5. The intensity is strongly attenuated beyond $Y = 19.5$ cm because of the long path length through the disc. An axial scan at a fixed radial position of $Y = 20.0$ cm is shown in Figure 6. The width of the region of recorded intensity is correct, bearing in mind the width of the neutron beam (1.3 cm) and the width of the turbine disc (1.3 cm).

4.0   CONCLUSIONS

It appears to be a practical proposition to mount the engine on the diffractometer, locate the turbine disc and obtain a signal of 1000 counts in the peak above the background in about 6 1/2 hours with a single detector set-up. This would be reduced by a factor of 4 by the use of a multidetector. Further, towards the shaft of the disc this time would be three times longer because of the attenuation of the beam by the disc whose thickness is a function of radial distance from the shaft. The technique of choice would be measurement of the lattice spacing, since as shown in Reference 2, the grain size of the Waspaloy dominates the statistics in the peak. The costly features of a future hot engine test include the engineering design to bring in air to the engine from outside the reactor building and to extract the exhaust, to bring in the fuel, and to build a fire-proof noise-and-disintegration barrier around the engine adjacent to the spectrometer. At a new reactor it might be possible to have a thermal neutron guide transporting neutrons to an engine test-bed facility outside the reactor building. These engineering considerations would then be far less of a constraint.

5.0   ACKNOWLEDGMENTS

of D. Leggett and the engineering assistance of Yvon Michaud and Erich Stephen from Pratt and Whitney, Canada Inc.

6.0 REFERENCES

1. T.M. Holden, J.H. Root, D.C. Tennant and D. Kroeze, ANDI-38, 1991.

2. J.H. Root, T.M. Holden and DC. Tennant, ANDI-49, 1992.

3. T.M. Holden, J.H. Root, D.C. Tennant, D.E. Kroeze and D. Leggett, Proc. Gas Turbine and Aero Engine Congress, Brussels, Belgium, ASME 90-GT-324, 1990.

4. D. Leggett, T.M. Holden, J.H. Root and D.C. Tennant, Proc. 37th Annual Symposium of the Instrument Society of America, San Diego, I ASA, 1991 -#91-090, 1991.

5. J.H. Root, T.M. Holden, D.C. Tennant and D. Leggett, Proc. 7th Symposium on Temperature, Toronto, Canada, 1992 (in press).

ATOMIC ENERGY OF CANADA LTD. - RESEARCH CO.
CHALK RIVER, ONTARIO

20558 - 2
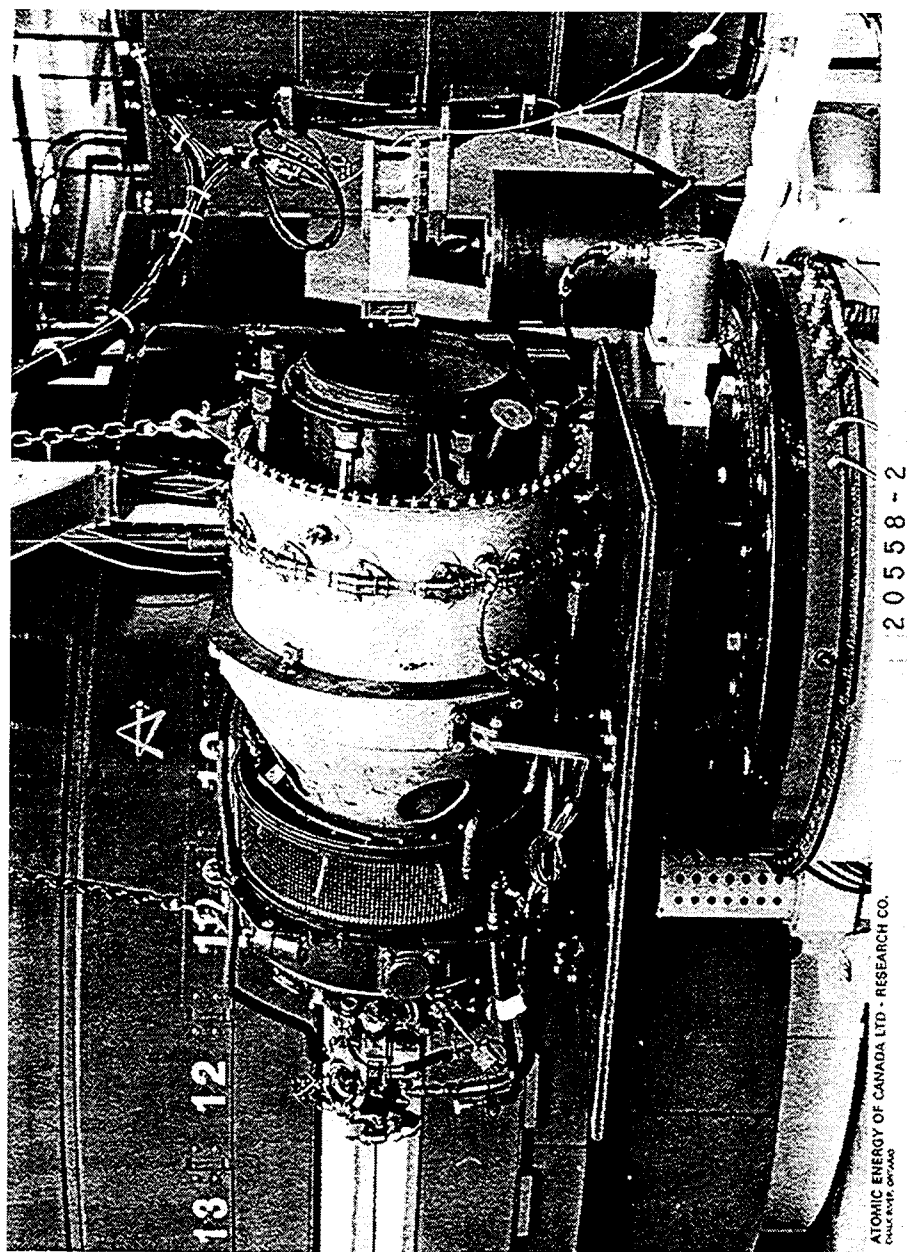
Fig. 1   Photograph of the PT-6 engine mounted on the L3 spectrometer at the NRU reactor for the cold engine test.
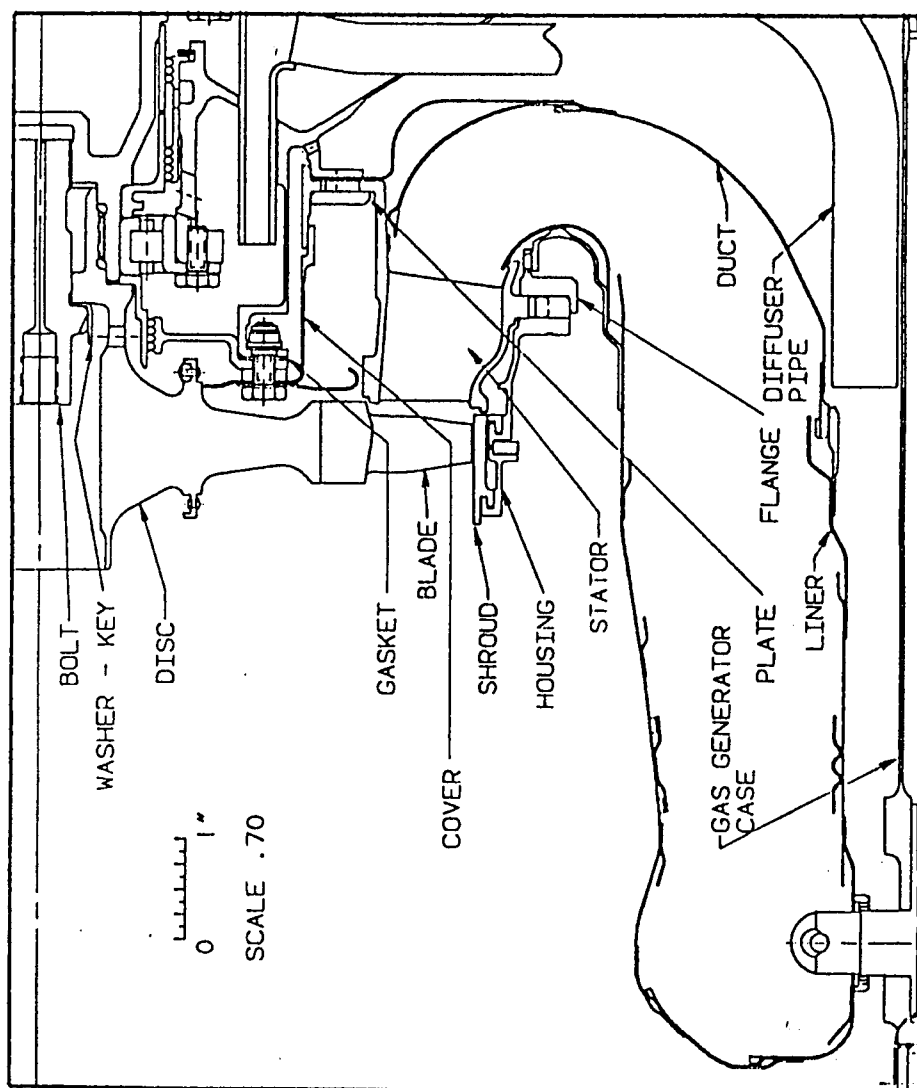
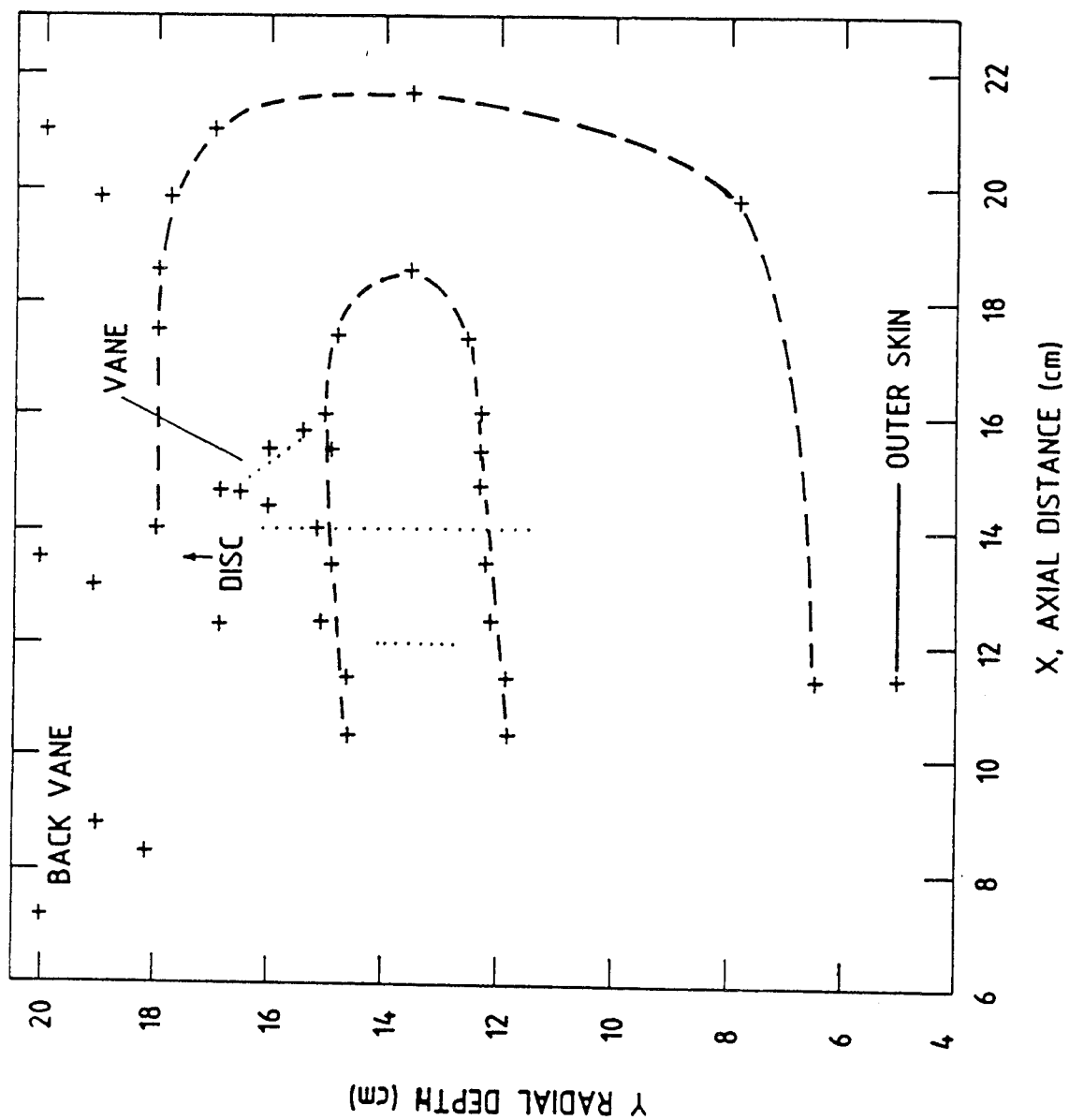**Fig. 2** Engineering drawing of PT-6 engine showing section in the horizontal plane.

Fig. 3 Map of engine structures determined from the positions of peaks in diffracted intensity in axial (X) and radial (Y) scans in the horizontal lane.
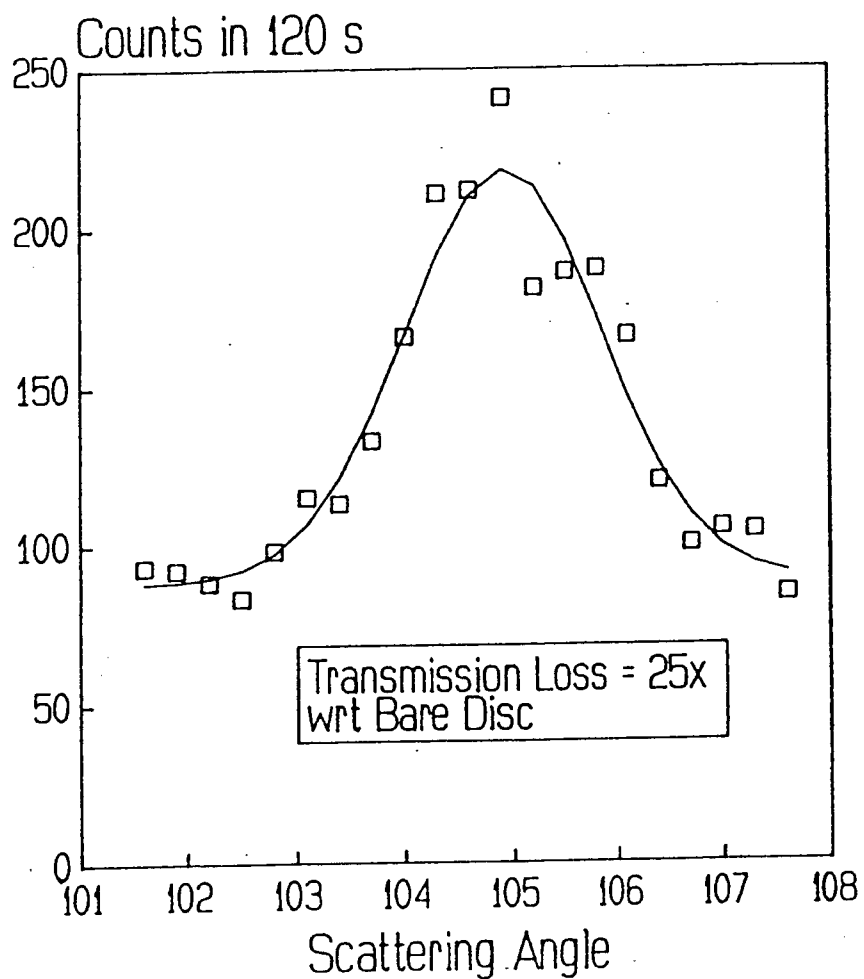
Fig. 4   (113) Diffraction peak recorded in the turbine disc at X=13.6, Y=20 cm.
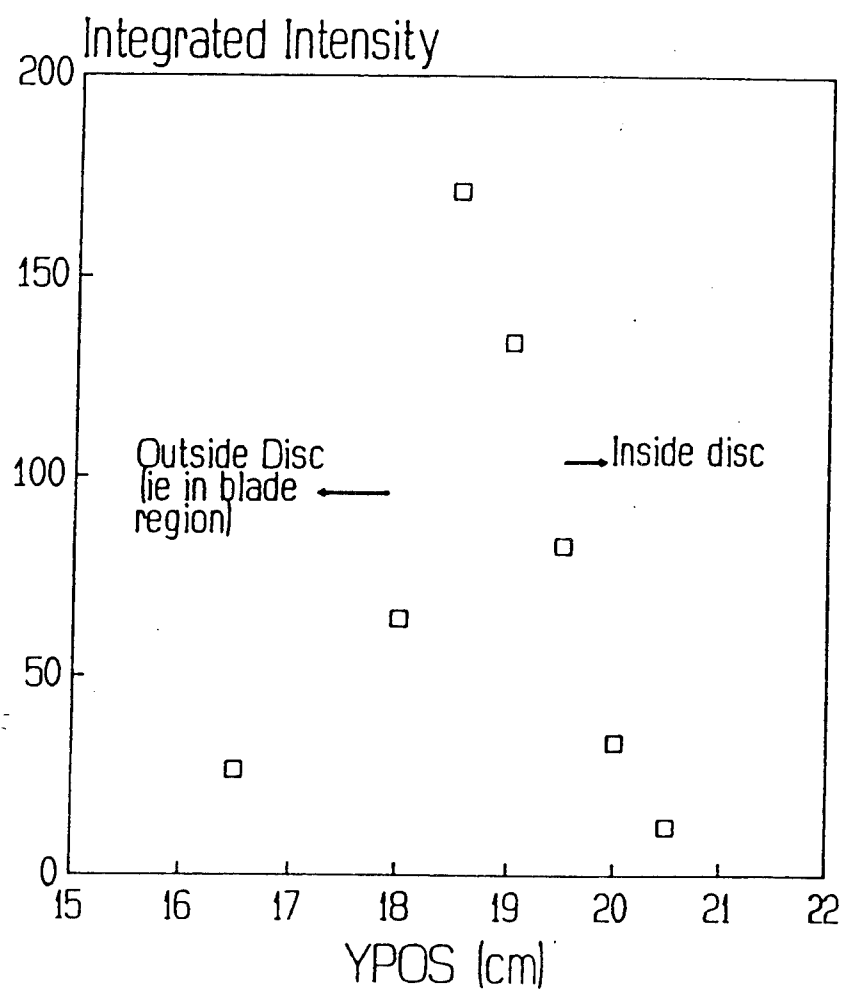
Cold Engine
Scanning Radially into Disc

Fig. 5   Integrated intensity from the turbine disc as a function of radial position at a fixed axial position of X=13.3 cm.
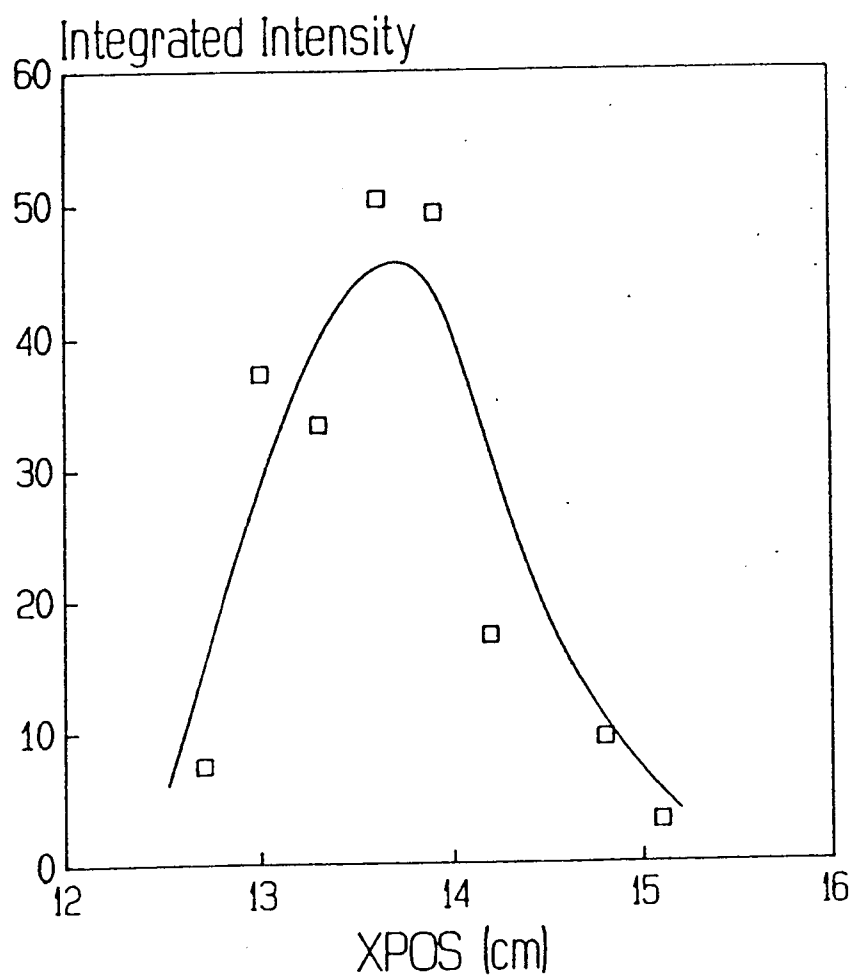
Fig. 6 Integrated intensity from the turbine disc as a function of axial position at a fixed radial position of 20.0 cm.